CRANFIELD UNIVERSITY

D. E. GALLARDO

DYNAMIC EFFECTS IN CdTe QUANTUM-DOT LEDs

NANOTECHNOLOGY CENTRE
DEPARTMENT OF MATERIALS
SCHOOL OF APPLIED SCIENCES

PhD THESIS

CRANFIELD UNIVERSITY

SCHOOL OF APPLIED SCIENCES

PhD THESIS

Academic Year 2005-2006

D.E. GALLARDO

Dynamic effects in CdTe quantum-dot LEDs

Supervisor: Dr S.C. Dunn

August 2006

This thesis is submitted in partial fulfilment of the requirements
for the degree of Doctor of Philosophy

ACKNOWLEDGEMENTS

ABSTRACT

In this work the electrical and electroluminescence properties CdTe nanocrystal films were analysed. The structure consisted of a multilayer of CdTe nanocrystals deposited by the layer-by-layer technique, sandwiched between an ITO anode and an aluminium cathode.

The first part of this work was dedicated to structural and process improvement. Earlier devices, produced through a layer-by-layer (LbL) manual procedure, had an average thickness of 30nm per nanocrystal monolayer, with a roughness near 30% of the overall thickness. Electrical tests showed current densities over $100 \, \text{mA/cm}^2$, with a frequent occurrence of pinholes and short-circuits that caused erratic sample behaviour and device rupture. SEM and AFM microscopic analysis showed that the nanoparticles were aggregated in 15-20nm thick clusters bound by polymer. A high porosity and non-uniformity of the multilayer was observed, explaining the formation of short-circuits. Luminescence was obtained from a very small number of samples, and with a very short duration that did not make spectral analyses possible.

A robotic arm was programmed to carry out the LbL deposition, in an attempt to reduce the inhomogeneities of the multilayer. A key factor was the introduction of a special routine to remove the samples from the solutions. The sample withdrawal was designed to be in the vertical at a rate of 1.18 mm/s. The idea was to use gravity and the surface tension of the aqueous solutions to remove all the excess liquid from the surface. Additionally, poly(ethylenimine) (PEI) was eliminated from the process to improve homogeneity. These modifications produced multilayers with a thickness of 3nm per layer, average roughness below 5nm and CdTe packing density of 27%. Electrical measurements showed a stabilisation of the current-voltage (I-V) characteristics. A significant improvement in luminescence occurrence frequency and intensity was also achieved, enabling first spectral analyses.

Once a reliable manufacturing procedure was developed, the electrical characterisation commenced with the analyses of samples with a different number of layers, operated in air. A field dependency of the I-V curves was found. Optimal performance was obtained from 30-layer samples, and this number of layers was adopted for subsequent analyses.

Best samples showed external quantum efficiencies of 0.51%, with a photometric response of 0.8 lm/W and peak brightness of 1.42 cd/m^2. However, current and electroluminescence (EL) degradation with voltage and operation time were found in the device.

Single carrier devices revealed a barrier for electron injection higher than predicted by the band diagram of the structure. The presence of an aluminium oxide layer at the multilayer/cathode interface was postulated, and confirmed through experiments in nitrogen. It was proposed that the growth of this oxide layer is the cause of device degradation during operation in air. However, it was demonstrated that the presence of the oxide favoured radiative recombination prior to degradation, with device efficiencies nearly 10 times higher than in devices without the oxide film. This was justified through three effects: charge accumulation at both sides of the oxide, field concentration across the oxide barrier and a reduction in leakage current.

Unequal behaviour of samples with different electrode materials revealed that charge injection was the limiting mechanism for current flow, with a current onset field in the range of 2-3×10^7 V/m. Fowler-Nordheim plots showed that field emission was responsible for hole and electron injection into the device. Also, Fowler-Nordheim plots provided evidence of the dynamic nature of the cathode oxidation process. Dielectric breakdown of the aluminium oxide barrier at a rupture field of 3×10^7 V/m was found as a possible triggering mechanism of oxide layer growth. It was found that a critical field around 4.5×10^7 V/m caused irreversible loss of photoluminescence (PL) of the nanocrystals. This loss was attributed to an avalanche effect within the multilayer. The operational range for the devices is then found to be between 2×10^7 V/m and 4.5×10^7 V/m.

TABLE OF CONTENTS

LIST OF FIGURES

LIST OF EQUATIONS

LIST OF TABLES

ACRONYMS

Alq3: 8-hydroxyquinoline aluminium

ED: Electron-only device (Al/CdTe/Al)

EL: Electroluminescence

FN: Fowler-Nordheim

HD: Hole-only device (Au/CdTe/ITO)

LbL: Layer-by-Layer

LED: Light emitting device, including light emitting diodes

MIM: Metal-insulator-metal device

NLED: Nanocrystal LED (all-inorganic)

OLED: Organic LED

PDDA: Poly(dimethyl-diallylammonium chloride)

PEI: Poly(ethylenimine)

PL: Photoluminescence

PLED: Polymer LED, here included among OLEDs

PPV: poly-p-phenylene-vinylene

SD: Standard device (Al/CdTe/ITO)

SDN: Standard device tested in nitrogen

1 Introduction

Around 20% of all energy produced worldwide is consumed in lighting applications. This consumption has been estimated at 2.016 TWh/year, or 21.103 PJ/year, equivalent to an electricity bill of $230.000 million/year. In terms of CO_2 emissions, it amounts to 1.775 million tonnes/year.* Most current lighting systems are based on low-efficiency mechanisms such as thermal emission: incandescence bulbs and kerosene lamps. There is a strong need to produce large-area, low-cost, long lifetime lighting sources with a high-efficiency profile to replace conventional lighting systems. Solid-state (p-n junction) LEDs and compact fluorescence lamps are recent incorporations to the domestic lighting market, offering improved efficiencies over traditional bulbs and fluorescent lamps, but their adoption in large surface applications is hampered by their higher manufacturing costs.

Figure 1. Europe city lights. Source: NASA, http://visibleearth.nasa.gov/

---

* Evan Mills, Ph.D., International Association for Energy-Efficient Lighting and Lawrence Berkeley National Laboratory, June 2002.

Furthermore, information technologies demand new luminescent displays capable of high-efficiency, low power consumption that also have low fabrication cost, are lightweight and have a wide range of colour capabilities. The telecommunications sector adds to this demand, with the tendencies in the mobile phone market to include high performance mini-displays with videoconferencing and multimedia capabilities. Cold-cathode fluorescence lamps are widely used for LCD (Liquid Crystal Display) displays, but they present luminance problems for daylight applications. The TFT (Thin-Film Transistor) technology offers better luminance, but production yields (the ratio between the displays which pass and fail the quality tests) are low, due to the huge number of transistors per display (around 2.4 million transistors for a 1024×768 display). FEDs (Field Effect Displays) have excellent contrast, luminance and production yield, but their high weight and volume, and their high power consumption prevents their use in portable appliances up to date.
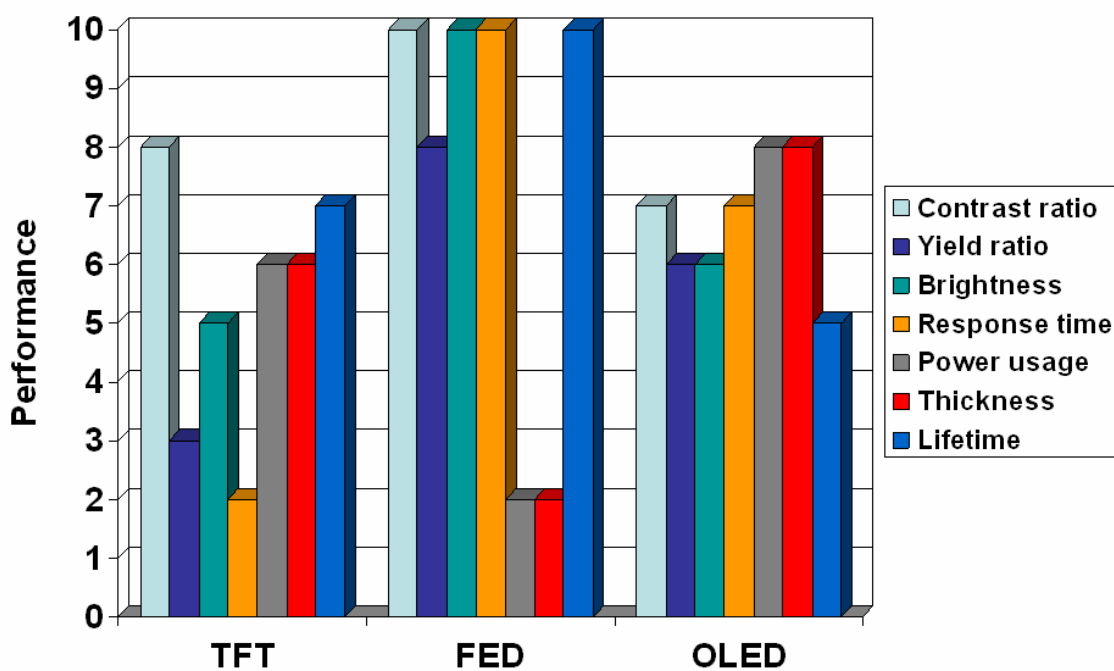
Figure 2. Comparison of the performance of the most relevant technologies for displays.

OLED is a very promising technology that is already hitting the displays market. It has got also possibilities in the lighting sector, as large area devices are viable in principle. Organic film deposition techniques are extremely flexible, with recent developments in ink-jet and screen-printing. However, its main problem is related with their sensitivity

to moisture and the formation of dark spots, that limit the lifetime. OLEDs also present problems of differential aging, in which different colours age at different rates, an important problem in colour appliances.

Hybridisation with inorganic semiconductor nanoparticles seems to be a possible way to improve the OLED technology. Semiconductor nanoparticles (*aka* nanocrystals or quantum dots) are inorganic semiconductor particles whose physical dimensions are reduced down to a few nanometres. At these sizes, the particles present properties intermediate between molecules and solid-state materials, due to the so-called *quantum confinement effects*. An important consequence of these confinement effects is an enhancement in the luminescence properties of semiconductor nanoparticles, with high spectral purity and excellent fluorescence efficiencies. Another advantage comes from the size-tunability of their emission: the colour of emission can be tuned just by changing the size of the nanocrystals, without any changes in composition or stoichiometry. These properties make nanoparticles a very attractive material for light emitting applications. In hybrid LEDs, the excellent luminescence properties of semiconductor nanocrystals are combined with the conducting properties and flexibility of manufacture of organic semiconductors. However, some limitations are still introduced by the relatively lower stability of organic materials.

A fully inorganic LED based on semiconductor nanoparticles is an option for the future: the NLED (Nanocrystal-LED). In these devices, all the active materials are inorganic, therefore eliminating the instability issues of organic materials. The main problem of NLEDs is related to the incorporation of nanoparticles to functional structures. Nanocrystal films need to keep the individuality of the nanoparticles, in order to preserve the confinement effects. This discontinuity of nanocrystal films affects their conductivity properties. Several electrical characteristics of semiconductor nanocrystal films are still in the early stage of research, especially charge injection and transport. The discontinuity of nanocrystal films introduces difficulties for the application of the theory of continuous media, traditionally used in the analysis of thin-film and OLED technologies. Concepts like band-bending and charge depletion areas are not clearly applicable to nanocrystal films. Most of the electrical studies on nanocrystal films have been done in conjunction with organic semiconductors, but they have introduced confusion about which properties are attributable to the nanoparticles and which ones to the organics. The literature related to fully inorganic nanocrystal devices is still very

scarce, this may be motivated by the efforts in the hybrid approach. Intensive research on electric properties of nanocrystals films will no doubt benefit the already developing hybrid technology, but also the future NLED. It is in this context that the present work is framed.

In this work, CdTe nanoparticles emitting red light will be used. As will be presented in the results, the peak of emission from these particles is centred on 630nm. The energy bandgap corresponding to this wavelength is ca. 2.0eV. The electron affinity of bulk CdTe is 4.5eV[1,2]. It is expected that confinement effects would make the up-shift of the conduction band significantly higher than the downshift of the valence band. Thus, the bottom edge of the conduction band of CdTe nanoparticles is thought to be close to 4.0eV from the vacuum level. For a bandgap of 2.0eV, the top edge of the valence band is then around 6.0eV from the vacuum level. Because of the position of the valence band in the nanocrystals, an anode with a high work function is required for hole injection. Regarding the cathode, it was preferred to avoid highly reactive materials like magnesium or calcium, and aluminium was selected as the electron injection material. The structure of our device consists of a glass substrate coated with indium-doped tin oxide (ITO), that acts as transparent anode. A film of CdTe nanocrystals is deposited on top of the ITO, and it is finally coated with an aluminium cathode. Figure 3 shows a picture of the device and its static band diagram.
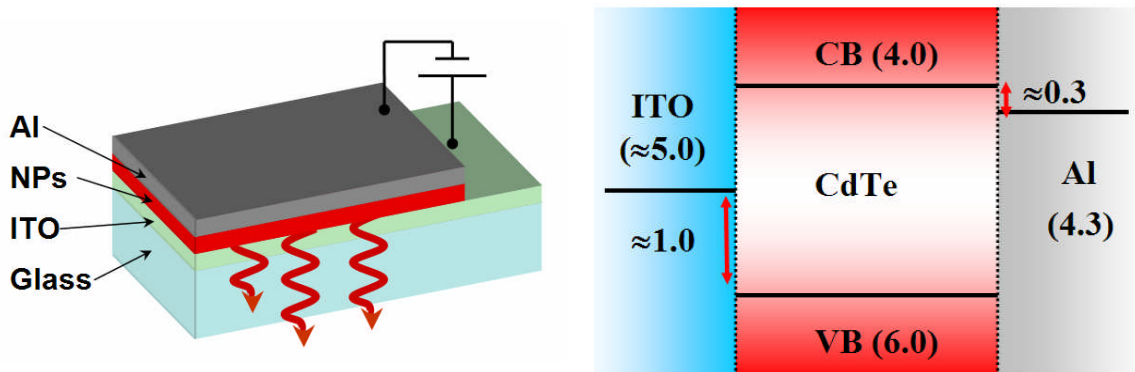
Figure 3. The device consists of a multilayer of nanocrystals sandwiched between two electrodes. The cathode is made of aluminium and the anode of ITO. The multilayer is deposited by a LbL procedure. The substrate is glass. Photons escape through the ITO and the substrate. The static band diagram on the right shows the barriers for electrons and holes as predicted from the positions of the different energy levels (quantities are in eV).

According to the band diagram of Figure 3, the barrier for hole injection is about 1.0eV high, while for electrons it is around 0.3eV. Therefore, electrons will be injected at lower voltages and in higher quantities than holes. This asymmetry in injection should influence profoundly the dynamics of the device. Electrons will carry most of the current.

The layer-by-layer (LbL) method was selected as nanoparticle deposition method. The LbL technique allows structural control at monolayer level. This makes possible a high structural and electrical homogeneity, necessary to prevent pinholes and short-circuit device rupture, without resorting to organic buffer films. In an NLED, the LbL method introduces a dielectric material between nanoparticles that is not present in spin-cast or drop-cast layers. Due to the insulating polymer, the expected transport mechanism is either tunnelling or hopping[3,4], or a combination of both. Dense packing of nanoparticles will be a requirement to have a significant current[5,6]. The dielectric material may reduce the conductivity of the nanoparticle films. However, this characteristic could help reduce the leakage current from un-recombined carriers. Device engineering might help overcoming the limitations in conductivity of nanoparticle films, while keeping their advantages.

In summary, the NLED proposed for this work is not expected to be optimal in terms of efficiency and lighting power. However, its structural simplicity will allow the direct investigation of carrier dynamics in semiconductor nanoparticles without the obscuring influence of other materials. The knowledge gained with these studies will provide the grounds for the improvement of more elaborated structures.

The theoretical and experimental background for this work will be presented in the Literature Review. It will provide an introduction to some basic concepts needed for the understanding of the subject, and a discussion of the technologies related to the NLED. The Experimental section will give details about the manufacture of the devices and the techniques used to characterise them. The Results and Discussion section is divided in two main subsections. The first subsection will describe the process of structural improvement of the device. The result of this improvement leads to a repeatable device manufacturing technique essential for the rest of the work. The second subsection is dedicated to the study of the electrical and emissive properties of the device.

2 Literature review

2.1 *Electroluminescence from semiconductors*

The characteristics that make semiconductor nanoparticles such interesting materials for light emitting devices (and many other applications) are better understood with a comparison with the properties of bulk semiconductors. In this section, some concepts of solid-state physics of semiconductors will be reviewed. For a more detailed explanation of the concepts, the reader is directed to the references. The focus will be made in features of special interest for the later study of semiconductor nanoparticles, and particularly in optical properties.

2.1.1 The band model.*

The chemical and electronic properties of materials are given by the arrangement of electrons within the material. In an atom, the location of an electron in space and time is given by its wave function, ψ. The wave function depends on the three space coordinates and time, $\psi(\mathbf{r}, t)$. If the potential energy of the electron in an atom is described by $V(\mathbf{r})$, the time evolution of an electron in that atom is given by the Schrödinger equation[†]

$$i\hbar\frac{\partial \psi}{\partial t} = -\frac{\hbar^2}{2m}\nabla^2\psi + V\psi$$

Eq. 1

Although accurate solutions for this equation can only be given for the hydrogen and helium atoms, these solutions can be adapted to explain the properties of atoms with higher atomic numbers. It is then found that electrons are only allowed to be in discrete states characterized by their energy. Electrons in an atom will tend to arrange themselves in the less energetic configurations, filling first the levels of lower energies. Only two electrons with opposite spin orientations can share the same quantum state

---

[*] Recommended bibliography: Feynman[154] offers an easy to follow introduction to quantum physics; more details can be found in French[155]. Ashcroft[156] and Omar[157] are excellent monographs on solid-state physics. Paul[158] is a more specialised treaty on band theory applied to semiconductors.
[†] This equation does not include relativistic nor magnetic effects.

(Pauli's Exclusion Principle). If two atoms are put close to each other, their electrons tend to arrange according to the new potential distribution, but they cannot share the same energy levels because of the Exclusion Principle. The resulting effect is that energy levels are split and redistributed in groups. As we increase the number of atoms, this rearrangement progresses. In macroscopic solids, which are aggregations of the order of 10^{23} atoms[*], the groups of levels are so compact that their separation in energy is very small. Because of this, they can be considered continuous bands instead of groups of levels (Figure 4 and Figure 5)[7].

Single atom   **Diatomic molecule**   **Mole**
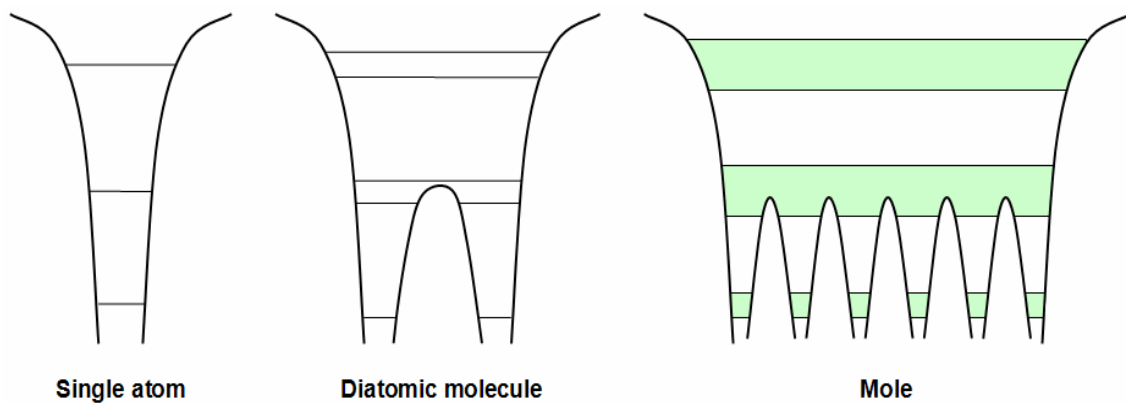
Figure 4. Illustration of the band model. An isolated atom presents a series of electron levels at permitted energies. When two atoms join to form a molecule, the electrons re-arrange to minimize the internal energy. But Pauli's Exclusion Principle allows only two electrons of opposite spin in each state. The consequence is a splitting of the electron levels at close energies. In a bulk solid, where the number of atoms is around 10^{23}, the level splitting is so fine that the different groups of levels can be considered as continuous bands.

In an equivalent way, the electronic configuration of a solid is determined by the solution to the Schrödinger equation, but now the function $V(\mathbf{r})$ must represent the potential of the whole solid. Then, $V(\mathbf{r})$ depends on the particular arrangement of the atoms within the solid. The arrangement of atoms in a crystalline solid is given by its *Bravais lattice*. Each lattice has its associated symmetries. Due to these symmetries, the solid can be thought as formed by the periodic repetition of a crystalline cell called the *unit cell*. The unit cell is the smallest crystalline cell with the symmetries of the whole lattice. Consequently, the potential $V(\mathbf{r})$ has the same translational symmetries as the lattice, i.e. the potential is periodic. Bloch's theorem establishes that, for a periodic

---

[*] Avogadro's number, here denoting a mole of substance as indicative of a macroscopic solid.

potential, the solutions to the wave equation Eq. 1 for electrons in the lattice have the same translational symmetry as the lattice.
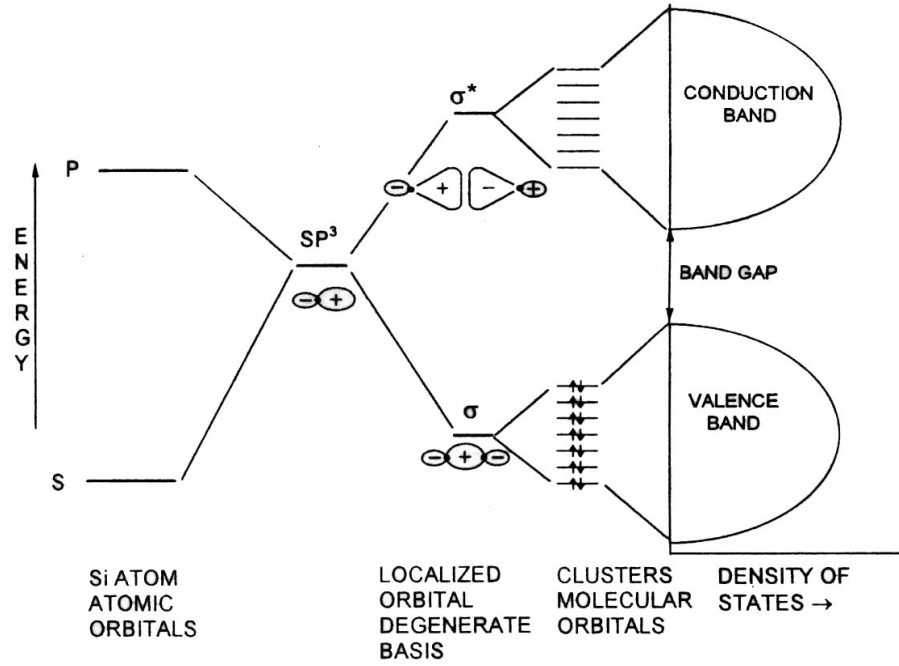
Figure 5. Evolution of silicon atomic orbitals into crystal energy bands [after Bawendi et al. (1990)[8]]

Every Bravais lattice has an associated reciprocal lattice, characterized by its set of wave vectors **K**, which is also a Bravais lattice. From quantum mechanics, the momentum **p** of a particle is related to its wave vector **k** through the relation $\mathbf{p}=\hbar\mathbf{k}$. Because of this, the reciprocal space is also called the *space of momenta* or *k*-space. The Brillouin cell is the reciprocal of the unit cell. One of the consequences of Bloch's theorem for electrons in a periodic potential is that their velocity **v** is an odd function of their wave vector, i.e.:

$$\mathbf{v}(-\mathbf{k})=-\mathbf{v}(\mathbf{k})$$

Eq. 2

When an electric field is applied to a solid, the current density in a band is:

$$\mathbf{J}=-\frac{e}{V}\sum_{\mathbf{k}}\mathbf{v}_{\mathbf{k}}$$

Eq. 3

where $\mathbf{v}_{\mathbf{k}}$ is the Bloch velocity of the state **k**, V is the volume of the reciprocal cell and e the charge of the electron. Since velocities are odd functions of the wave vector **k**, it

follows that the sum for all **k** equals zero if all the levels in a band are occupied. Thus, a band completely full of electrons cannot carry an electric current. Only those bands that are partially full are able to carry an electric current when an electric field is applied.

Conventionally, the uppermost completely full band is called the valence band. The conduction band is that immediately over the valence band. The conduction band can therefore be partially filled or completely empty. An empty conduction band has no carriers to support an electric current. Partially filled conduction bands are required for electric conduction (Figure 7). As described earlier, the energy levels between the conduction and valence bands are forbidden and constitute the so-called energy *band-gap*. An electron from the valence band can be transferred to the conduction band by absorption of an amount of energy at least equal to the value of the band-gap, E_g. This energy can be supplied by photons or phonons. High-energy particles, like cosmic rays, can also induce these transitions. Alternatively, an electron can release an energy equal or greater to the band-gap E_g by dropping from the conduction to the valence band. These two different transitions between the conduction and valence bands are called *band-to-band transitions* (Figure 6).
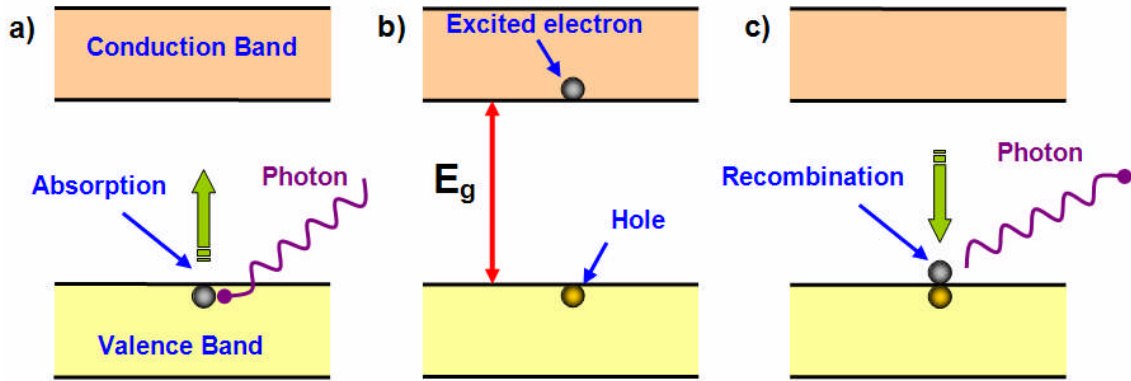
Figure 6. Band-to-band transitions. A photon of energy $E_a \geq E_g$ impinges onto the semiconductor, and it is absorbed by an electron in the valence band (a). The energy E_a is invested in promoting the electron across the forbidden gap into the conduction band, leaving a hole in the valence band (b). In the process of radiative recombination, the electron decays from the conduction band and recombines with the hole in the valence band, releasing the energy lost in the form of a photon of energy $E_r \geq E_g$ (c).

If the band-gap is large (several eV), an electron needs a high-energy photon to jump from the valence band to the conduction band. This transition will only occur under illumination of short wavelength light, typically in the UV region. Thus, (in normal

ambient conditions) the material is an insulator. Examples of insulators are diamond and alumina, with gaps of 7eV and 8eV respectively. Alternatively, if the energy gap is narrow, some electrons can be excited to the conduction band by the absorption of photons in the visible or infrared parts of the spectrum, and phonons. These electrons partially fill the conduction band, making possible the conduction of electricity. The voids they leave in the valence band are known as holes, *quasi-particles* that can be treated as positively charged carriers. A material with these properties is a semiconductor. Semiconductors at a given temperature *T* have a certain number of electron-hole pairs, due to the thermal energy. This number is called *intrinsic carrier concentration*, *n*, and is given by

$$n = 2\left(\frac{k_B T}{2\pi\hbar^2}\right)^{3/2} (m_e m_h)^{3/4} \exp\left(-\frac{E_g}{k_B T}\right)$$

Eq. 4

where m_e and m_h are the effective masses of electron and hole respectively. Typical examples are Si and Ge, with gaps of 1.22eV and 0.66eV and intrinsic carrier concentrations of 10^{10} cm^{-3} and 2×10^{13} cm^{-3} respectively (see Figure 7).
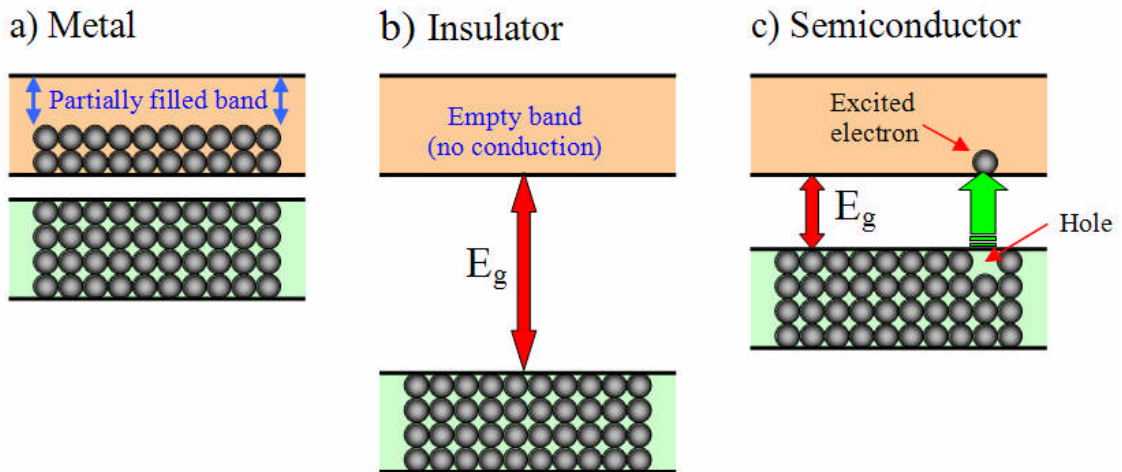
Figure 7. Different types of materials as a function of the bandgap width and electron population in the conduction band. a) The conduction band is partially filled and electric conduction is possible. The material is a conductor. b) The conduction band is empty and the band gap is too large to allow photon-assisted electronic transitions. The material is an insulator. Examples of insulators are diamond (7eV) and alumina (8eV). c) The conduction band is empty and electric conduction is not possible. However, the bandgap is narrow and photon assisted transitions can populate the conduction band with electrons. The vacancies in the valence band can be considered as particles with a positive elemental charge, known as *holes.*

The material is a semiconductor. Examples of semiconductors are silicon (1.22eV) and germanium (0.66eV).

2.1.2 Light emission in semiconductors

2.1.2.1 Band-to-band transitions

The process of light emission in semiconductors is known as radiative recombination[9-11]. In an excited semiconductor there will be holes near the top of the valence band and electrons near the bottom of the conduction band. Due to the presence of holes in the valence band, the electrons in the conduction band are in an unstable high-energy state. The holes in the top of the valence band constitute empty lower energy states that the electrons can fill; consequently electrons in the conduction band can release their extra energy and fill the vacancies in the valence band, recombining with the holes. The transition from a higher to a lower energy level results in an energy loss equal to the difference in energy of these levels, i.e. E_g (*fundamental transition*). When this energy is released as heat or as lattice vibrations, the process is called *non-radiative recombination*. Alternatively, if the energy is released in the form of a photon, the process is known as *radiative recombination*.

Quantum mechanics imposes some restrictions to electronic transitions, the most important here related to the preservation of the total spin. Allowed radiative transitions are given by the *selection rules*[12,13]. Of every four recombinations, only one comes from a singlet state and drives radiative recombination, the other three come from triplet states and result in non-radiative recombinations[12,13]. Thus, for a (bulk) semiconductor, radiative recombination is only 25% likely.

In radiative recombination, the emitted photon has an energy equal or greater to E_g (fundamental transition). The value of the energy band-gap is a characteristic of every semiconductor (although its precise value depends on temperature); therefore each semiconductor has its characteristic light emitting frequency.

The energy released in an electron-hole recombination process can be transferred to a third electron, constituting a non-radiative recombination mechanism known as *Auger*

recombination[5,11,14]. Metal electrodes act as a source of quasi-free electrons, and can cause the quenching of luminescence[6,15,16].

2.1.2.2 Excitons

An electron-hole pair can get linked via Coulomb interaction, forming an *exciton*[17,18]. The exciton can be considered an individual entity, a pseudo-particle or quasi-particle; this allows a simplified study of the electron-hole interaction, because it is possible to assign to the exciton particle-like properties: mass, momentum, energy, Bohr radius, etc[17]. The exciton can recombine radiatively by emitting a photon. The exciton energy spectrum consists of a discrete set of energies given by:

$$E_n = E_g - \frac{Ry^*}{n^2}$$

Eq. 5

where *n* is the order of the exciton (*n*=1,2,…) and *Ry** is the *exciton Rydberg energy* of the material. Thus, the energy associated to excitons is slightly lower than in band-to-band transitions. The proportion of excitons is given by Saha's equation

$$\frac{n_{exc}}{n} \propto n \left(\frac{2\pi\hbar^2}{kT} \right)^{3/2} \exp\left(\frac{Ry^*}{kT} \right)$$

Eq. 6

where *n* is the number of free carriers (electrons and holes). This means that exciton contribution is important only for *Ry**≥*kT*. For binary semiconductors, Ry* is typically in the order of several meV, e.g. 5meV in GaAs, 16meV in CdSe, 18meV in ZnSe, 29meV in CdS[17] and ≈10meV in CdTe. For these semiconductors, the exciton contribution is only noticeable at low temperatures[17], and most of the excited states will correspond to uncorrelated electrons and holes (Figure 8).
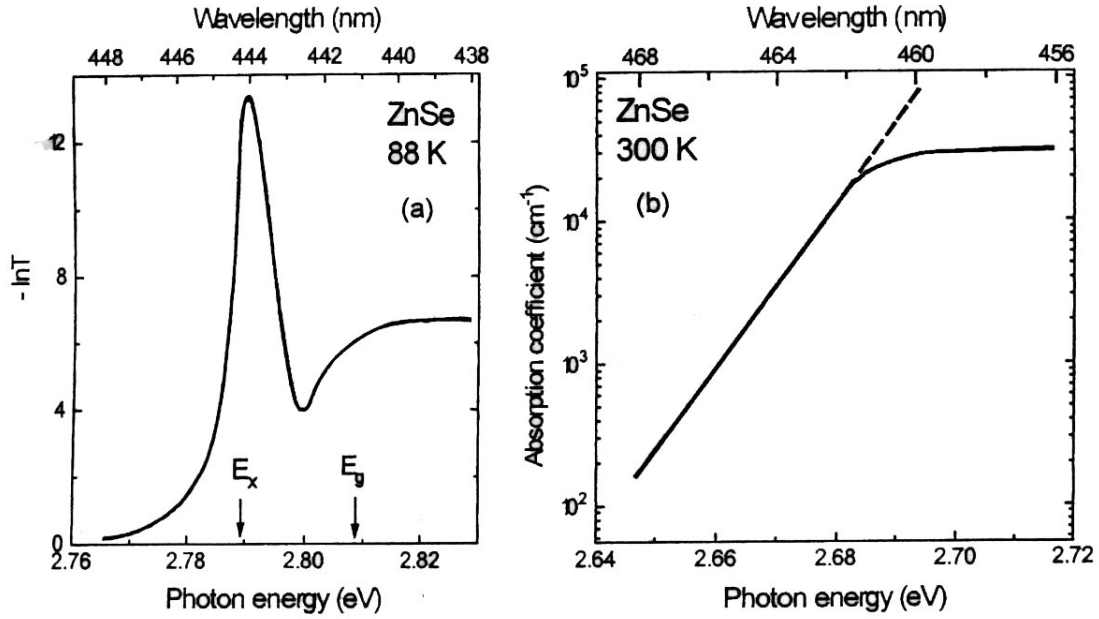
Figure 8. Absorption spectrum of ZnSe near the fundamental transition, at 88K and 300K. The Rydberg energy for ZnSe is Ry^*=18meV, whereas the band-gap energy is E_g=2.81eV at 80K, and E_g=2.67eV at 300K. (a) At 80K, the thermal energy is kT=6.9meV, and the exciton absorption causes a sharp peak in the spectrum. (b) At 300k, the thermal energy is kT=26 meV, and the exciton peak has vanished against the electron-hole absorption. [After Gribkovskii et al. (1990)[19]]

2.1.2.3 Direct and indirect semiconductors

In the simplest model, the energies of the conduction band (CB) and valence band (VB) are given respectively by[20]

$$E_c(\mathbf{k}) = E_g + \frac{\hbar^2 k^2}{2m_e^*} \quad \text{and} \quad E_v(\mathbf{k}) = -\frac{\hbar^2 k^2}{2m_h^*} \qquad \text{Eq. 7}$$

where $\mathbf{k}$ is the momentum vector, m_e^* and m_h^* are respectively the effective masses of electron and hole, and the origin of energy has been chosen at the top of the valence band (Figure 9). In an energy-momentum (k-space) band diagram, the maximum of the valence band (VB) and the minimum of the conduction band (CB) lie at k=0 (designated Γ in the diagram, Figure 10). Any band-to-band transition (permitted by the selection rules) must conserve the energy and momentum of the system. Thus, allowed transitions happen vertically in the band diagram, by the emission or absortion of a

13

photon of energy equal of greater than E_g. These are called *direct transitions*, and the semiconductors in which they happen are designated *direct semiconductors*[9,21].
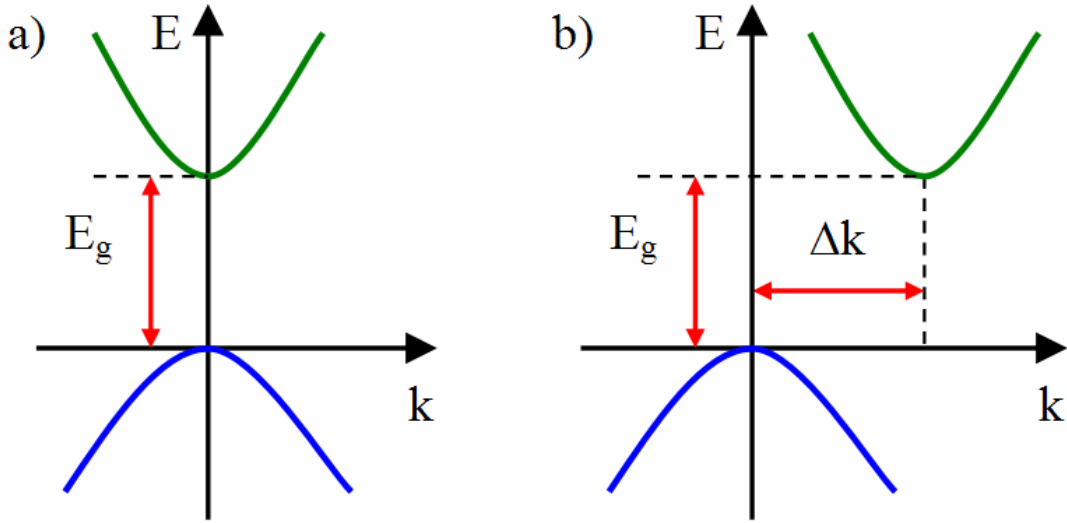
Figure 9. Direct and indirect transitions in semiconductors. a) In direct transitions, the top of the valence band and the bottom of the conduction band coincide at the same value of momentum, ***k***=0. The electron jumps vertically between the conduction and valence band by releasing or absorbing the energy difference E_g. b) In indirect semiconductors, the top of the valence band and the bottom of the conduction band occur at different values of ***k***. Thus, an electron transition involves not only a change in energy E_g, but also a change in momentum Δ***k*** to conserve the total momentum. This latter condition requires the intervention of a phonon, and makes indirect transitions less probable than direct transitions.

However, there are semiconductors for which the minimum of the CB does not happen at ***k***=0. In these materials, vertical transitions cannot happen because they would violate the conservation of momentum (the photon carries a negligible momentum at optical frequencies). Thus, band-to-band transitions in these semiconductors require, in addition to the photon, the participation of a phonon, to account for the difference in momentum Δ***k***. Such transitions are called *indirect transitions*, and the semiconductors in which they happen are designated *indirect semiconductors*.
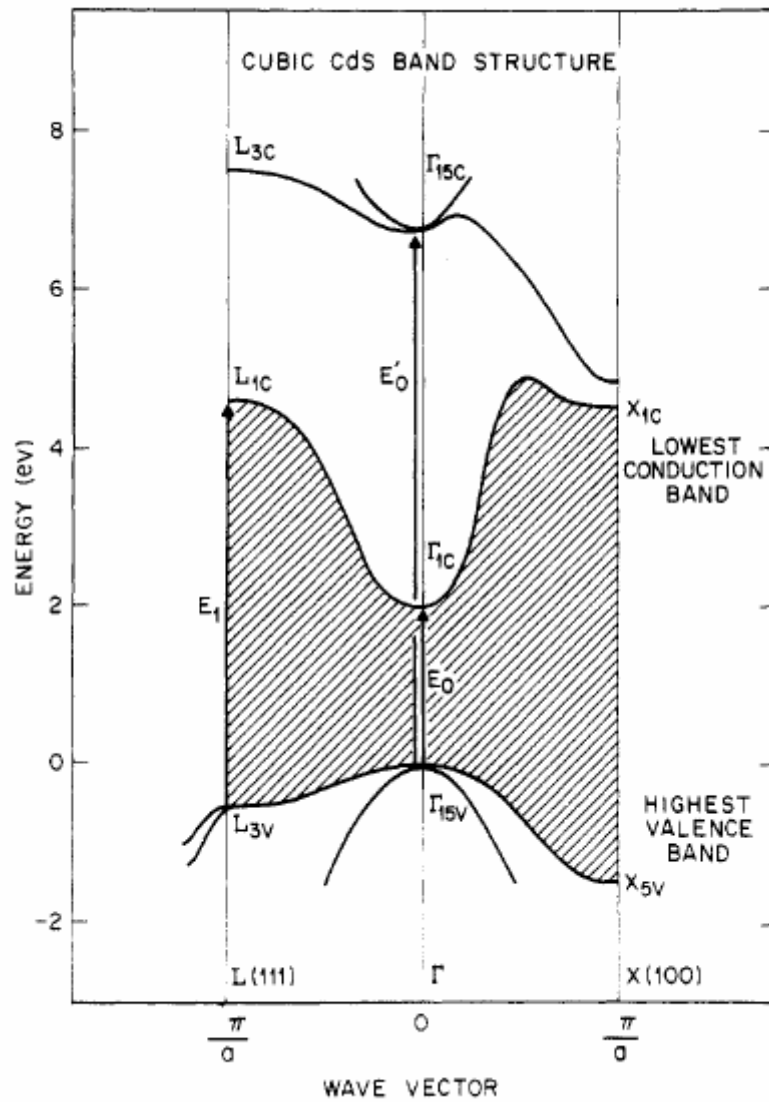
Figure 10. Band diagram of Crystalline CdS [after Brus (1986)[22]]. The maximum value of the valence band and the minimum of the conduction band lie at **k**=0 (point Γ). Thus, CdS is a direct semiconductor.

Indirect transitions require the simultaneous intervention of two different particles, a phonon and a photon, whereas direct transitions need only the photon. Thus, indirect transitions are less probable than direct ones. This makes indirect semiconductors less efficient for radiative recombination, and therefore less convenient for light emitting devices. Table 1 gives the values of several of these properties for a few selected semiconductors.

Table 1. Properties of selected semiconductors[23]. The energy band-gap E_g is measured at 300K, and the corresponding wavelength of emission is given as λ. The refraction index is n_r.

Material	Type	E_g (eV)	λ (nm)	n_r
Si	Indirect	1.12	1107.6	3.49
Ge	Indirect	0.66	1879.5	3.99
GaP	Indirect	2.26	548.9	3.20
GaAs	Direct	1.44	864.5	3.30
GaSb	Direct	0.72	1722.9	3.80
CdTe	Direct	1.56	795.2	2.50
CdSe	Direct	1.74	714.0	2.45
CdS	Direct	2.42	513.4	2.32

2.1.2.4 The p-n junction

The basic device structure for exciting electroluminescence from semiconductors is the p-n junction[21,24,25] (Figure 11). It consists of the intimate union of an n-type semiconductor and a p-type semiconductor. Holes are majority carriers in p-type semiconductors, whereas electrons are majority carriers in n-type semiconductors. When the junction is forward biased, the applied electric field drives holes and electrons into the n-type and p-type semiconductors respectively, where they are minority carriers. Minority carriers have a high probability of recombination, due to the abundance of their conjugate majority carriers. In practice, it is convenient to favour the injection of minority carriers of one type over the other. To do this, one of the regions is doped heavily. For example, to favour minority electrons into the p-type material, the n-type material is doped in excess (n^+ semiconductor). Thus, due to their overabundance, the number of electrons injected into the p-type region will be much greater than the number of holes injected into the n-type region. In that way, light is emitted from the p-type semiconductor. Then, placing the p-type region near the external device surface (as shown in Figure 11), re-absorption of photons is minimized, and the amount of light extracted from the device is maximized.
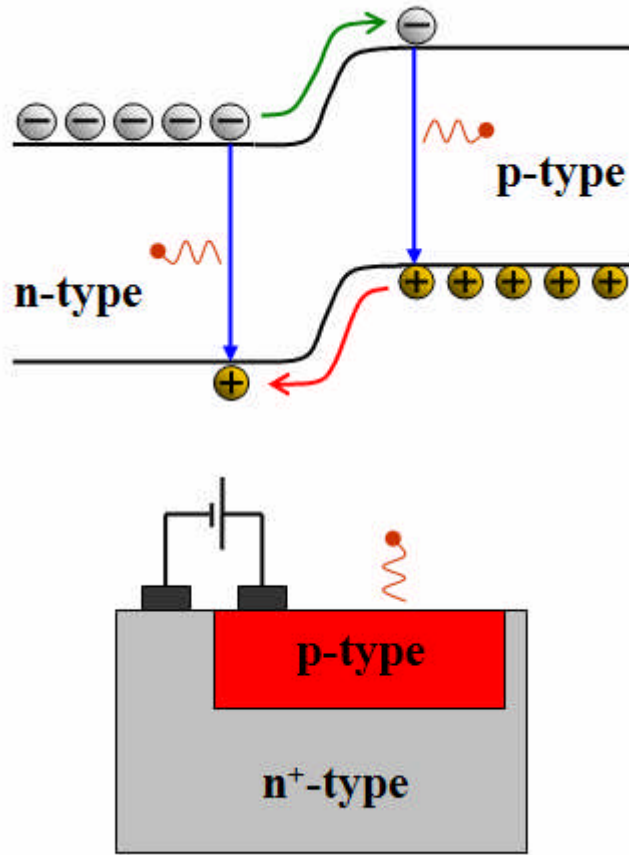
Figure 11. Electroluminescence from p-n junctions. The band diagram on the top shows how electrons and holes are minority carriers in the p-type and n-type areas respectively. Minority carriers have a high probability of recombination. In direct semiconductors, up to a 25% of recombinations would be radiative. A physical realization is shown at the bottom. A p-type well is grown into an n⁺-type substrate; the heavily doped substrate provides minority electrons to the p-type area, where recombination takes place. As the p-type area is close to the external device surface, most of the photons will escape the device.

2.1.3 Absorption and photoluminescence spectra

As introduced in Section 2.1.2, the energy band-gap is a fundamental property of semiconductors. The band-gap width, E_g, determines the wavelength of the light emitted or absorbed by the material. The bottom edge of the conduction band and the top edge of the valence band limit the band-gap. The positions of these two edges are very important for charge injection into the nanoparticles. Thus, a precise knowledge of E_g is essential for the understanding of opto-electronic devices. Two characterization

techniques are generally employed to measure E_g: absorption and photoluminescence spectrometries (Figure 12).

In absorption spectrometry[26], the sample is illuminated with (quasi) monochromatic light of known intensity. This light interacts with the sample and the resulting intensity is collected and measured. The difference between the intensities before and after the interaction measures how much light was absorbed at the given wavelength. This measurement is then repeated for all wavelengths within the surveyed range. There are several types of absorption measurement, depending on the type of interaction with the samples. When the light from the source traverses the sample the technique is called transmittance absorption. This technique is generally used with thin solid samples or colloidal suspensions. If the light is collected after reflection at the surface of the sample, the technique is called reflectance absorption. It is normally used with opaque bulk samples. In semiconductor samples, there is a pronounced increase in absorption when the excitation energy approaches the value of the bandgap, as the incoming photons interact strongly with the semiconductor creating electron-hole pairs. In direct semiconductors, for exciting photons with an energy close to the ground excitation, the energy bandgap (E_G) can be related to the measured absorption, a, through the equation[9,21]:

$$a = k \frac{\sqrt{E_I - E_g}}{E_I}$$

Eq. 8

in which E_I is the energy of the incident photons and k is a constant depending on the material. If both terms are squared, the equation becomes:

$$\left(aE_I\right)^2 = k^2\left(E_I - E_g\right)$$

Eq. 9

Thus, a plot of $(a \cdot E_I)^2$ against the excitation energy E_I renders a straight line for the energies near the band edge. The intersection of this line with the excitation energy axis gives the value of the bandgap[27,28].

In photoluminescence spectrometry[29], the sample is excited with monochromatic light with a wavelength shorter than that associated with the first exciton. The material absorbs photons by creating electron-hole pairs. When the excitation is removed, the

excitons relax, and a number of them release energy radiatively. The energy distribution of this emission constitutes the photoluminescence spectrum. A strong peak is detected at the first exciton energy, giving a direct measurement of the bandgap. When the semiconductor is direct, the time of de-excitation of the sample is short and the technique is called fluorescence spectrometry. Alternatively, is the semiconductor is indirect, radiative recombination would require longer times, and the technique is called phosphorescence spectrometry. Electroluminescence spectra are similar to photoluminescence spectra, but samples are excited electrically instead of optically.
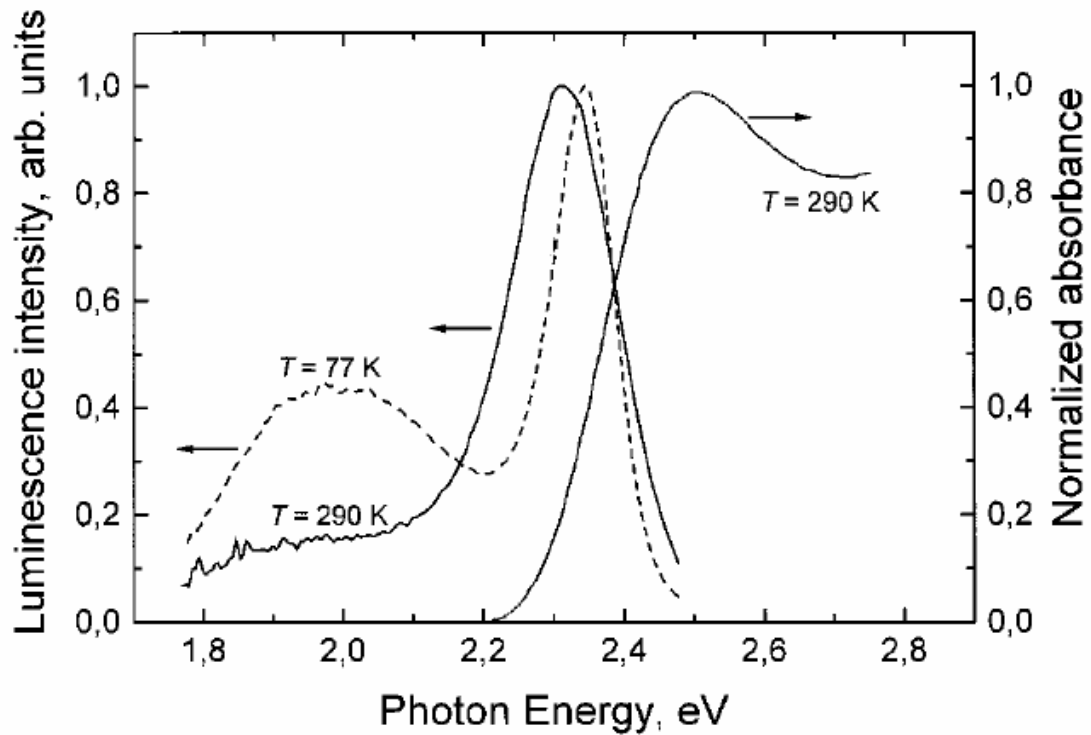
Figure 12. Absorption and photoluminescence spectra from a sample of CdTe nanocrystals. The temperatures at which each spectrum was taken is also indicated. [After Kapitonov et al. (1999)[30]].

2.1.4 Electroluminescence efficiency

There are many different ways of measuring the light output of a light-emitting device[31,32]. The choice of radiometric or photometric units, the extension of the source and the directionality of the emission, among other factors, determine the units of measure[33,34]. There are also several different criteria to evaluate the emission efficiency

of a device, depending on the applications it might be used for. The variety of figures of merit for display applications is especially wide, as they introduce parameters concerning the homogeneity of emission from sources of relatively large emissive areas. This variety can generate confusion when specifying the performance of a research or prototype device[35].

In basic research, the external quantum efficiency, η_{ext}, is a very well established magnitude and is used widely with organic and inorganic devices. It is defined as the ratio of photons emitted *out of the device* to the number of charges injected into the device[36]. To measure the number of photons emitted, a calibrated detector with a known spectral response is used. For highly monochromatic sources, it can be considered that all the emitted photons have the same wavelength. Otherwise, a convolution product of the emission spectrum with the spectral response of the detector is required[31]. The number of injected charges is measured directly by the current applied to the device. However, in p-n junction devices, a distinction can be made between the injected charges and the charges that cross the junction, due to the well-defined series resistance of the device[36]. Such a distinction is not always possible in other types of device where the series resistance is not defined, e.g. NLEDs.

Photons are generated within the structure and a fraction of them might be reabsorbed in their way out of the device. Also, usual solid-state semiconductors have refraction indexes greater than unity (Table 1). When light traverses the interface towards a medium with lower index (e.g. the air), total reflection causes a loss of photons. The external quantum efficiency takes into account implicitly all these losses. However, a measure of the amount of photons generated internally can be desirable in order to evaluate internal mechanisms, e.g. recombination statistics. The internal quantum efficiency, η_{int}, is defined as the number of photons generated internally per injected carrier. It can be related to the external quantum efficiency through the equation[33,37]:

$$\eta_{int} = 2n^2 \eta_{ext}$$

Eq. 10

where *n* is the refractive index of the semiconductor. The internal efficiency corrects only the losses due to internal reflection.

Another measure of efficiency is the power efficiency, defined as the ratio between the total radiant power and the electric power supplied to the device. The light output can also be specified in photometric units. Photometric units are weighted according to the human eye sensitivity. Typical photometric figures of merit are lumens per watt (lm/W), candela per square meter (cd/m^2), and candela per ampere (cd/A)[31].

2.2 Nano-structured semiconductors

In this section, the most important quantum size effects for semiconductor nanoparticles will be reviewed. Confinement effects will be analyzed by comparison to the band model for bulk semiconductors. After this, the manufacture of semiconductor nanoparticles will be reviewed, with emphasis on the synthesis of nanoparticle colloids by chemical routes.

There will be a subsection dedicated to the layer-by-layer (LbL) deposition method. Nanoparticles are incorporated into devices in many different ways: dip coating, spin casting, electrochemical methods, etc. Spin coating is perhaps the most extensively used technique. However, dip and spin coating methods present problems when multiple layers have to be deposited. The layer-by-layer method combines the control at nano-scales with the possibility of stacking multiple layers. For these reasons, LbL was chosen for this work.

2.2.1 Quantum confinement effects. Nano-structured semiconductors.

When the size of a semiconductor is reduced to the range of 10-100nm, important modifications to its optical and electronic properties emerge. These modifications come from the *quantum confinement effects* (QCE)[38-40]. In semiconductors, the electron and hole wavelengths, λ_e and λ_h, and the Bohr radius of the exciton, a_B, are in the order of several nanometres long[17]. For bulk materials, these lengths are much smaller than the physical size of the crystal, and thus electronic properties can be considered as independent of the crystal size. This fact is implicit in solid-state physics for bulk solids.

However, it is possible to create structures with physical dimensions comparable to (weak confinement) or smaller (strong confinement) than λ_e, λ_h and a_B[41].

When spatially confined, the dynamics of electrons, holes and excitons are altered significantly[41,42]. If this size confinement is in one dimension, the structure is called a *quantum well*. If the confinement is in two dimensions, the structure is called a *quantum wire* or nano-wire. When the confinement affects the three spatial dimensions, the structure is referred to as a *quantum dot*, nanocrystal or nanoparticle. In this section, we will focus in quantum dots, and the modifications that confinement introduces in their electronic and optical properties.

In Section 2.1.2.2, it was explained that the number of excitons depends exponentially on the ratio *Ry*/kT*. We showed that the exciton contribution at room temperature was negligible in several semiconductors, due to their small Rydberg energy. However, an electron-hole pair in a quantum dot is confined in a space of dimensions comparable to the exciton length. In this situation, the Coulomb interaction between electron and hole becomes stronger than the Rydberg energy and their motion becomes strongly correlated[43]. Consequently, the elementary excitation in quantum dots will be considered as an exciton. This strong Coulomb interaction between electron and hole introduces additional terms to the crystal potential $V(\mathbf{r})$. The solution of the Schrödinger equation with this modified potential is not analytical. Variational techniques provide a first exciton energy given by[22,41,44]:

$$E_{exc} = E_g + \frac{\pi^2 \hbar^2}{2\mu a^2} - 1.786\frac{e^2}{\varepsilon a}$$

Eq. 11

where μ is the reduced mass of the electron-hole pair and a is the quantum dot radius. The consequences of the confinement effects will be presented here through modifications to the typical band diagram of a bulk semiconductor[22,45,46] (Figure 13).

Perhaps the most important confinement effect for opto-electronic applications is the widening of the bandgap. The lower edge of the conduction bands shifts towards higher energies, while the top of the valence band shifts in the opposite direction. This widening in the energy gap translates in a shift towards the shorter wavelengths in the light emitted. The consequence is that the wavelength of emission can be tuned by varying the size of the nanoparticles; devices emitting at different wavelengths can be

fabricated simply by changing the size of the particles, without changes in the manufacturing process. Also, wavelength tunability makes available at the visible spectrum a number of direct semiconductors that in bulk form emit in the infrared[47,48].
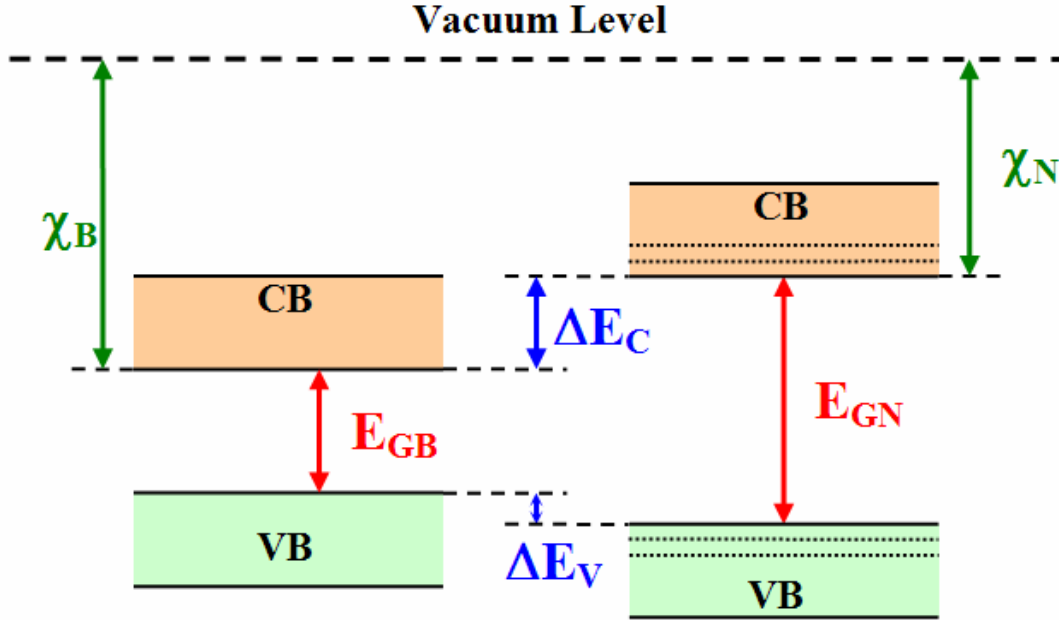
Figure 13. Quantum confinement effects in semiconductors. The most important effect is the bandgap (E_G) widening with decreasing nanoparticle size; this effect allows the tuning of the exciton emission. Another effect is the reduction of the electron affinity (χ), which can affect electron injection into the nanoparticles. The reduction of the electron affinity (ΔE_C) is generally larger than the increase in ionization energy (ΔE_V). The splitting of the lower exciton states, symbolized by the discontinuous line at the band edges, enables efficiencies over the 25% limit imposed by selection rules.

Efros and Rosen[49] calculated theoretically that the conduction band upward shift is usually greater than the downward shift in the valence band (Figure 14), and Gao et al.[4] found experimental evidence of this asymmetric shift in CdTe nanoparticles. Thus, the lowering of the electron affinity, χ, is more pronounced than the increase in ionization energy. The lowering in electron affinity can affect to electron injection into the nanoparticles, because it forces the use of an electrode with a lower work function for a good injection. But lower work functions are associated with higher chemical activity, and this can be an issue in terms of chemical stability of the device.
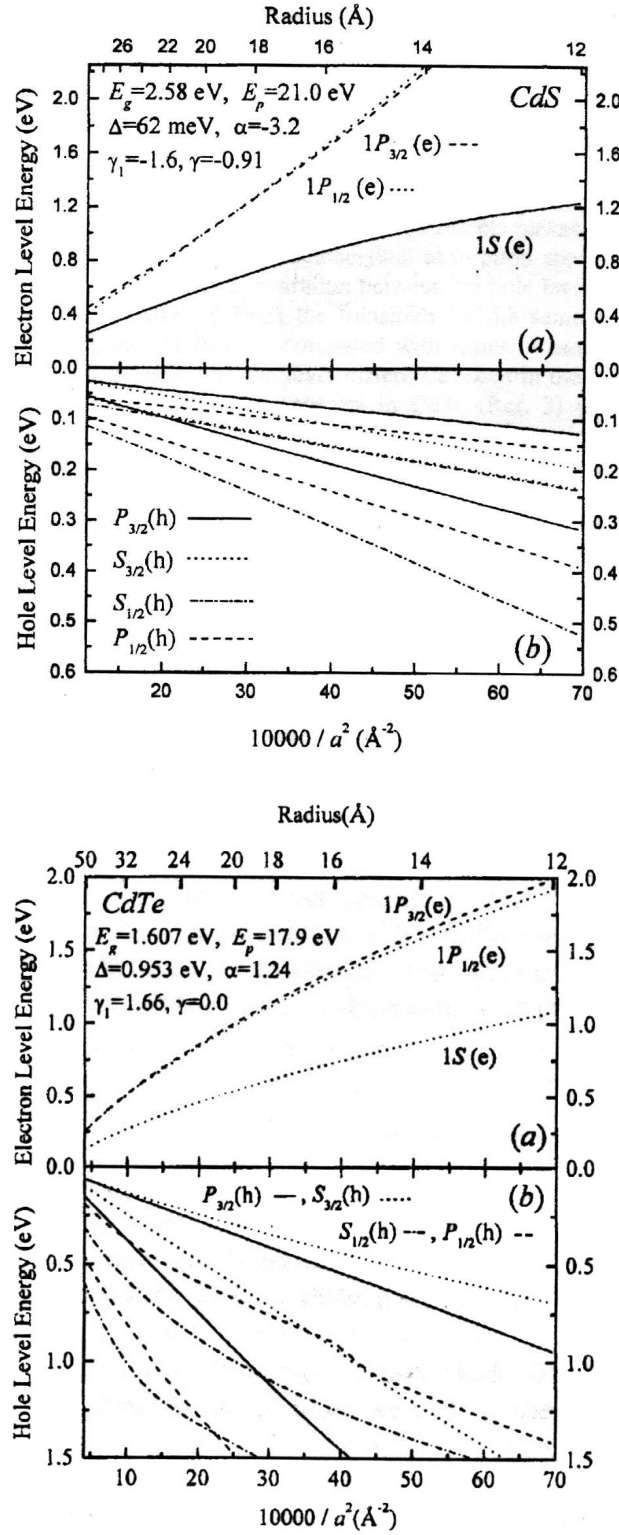
Figure 14. Size dependence of electron and hole energy levels in CdS and CdTe as calculated by Efros and Rosen. The upward shift for electron levels is more pronounced than for hole levels. [After Efros and Rosen (1998)[49]]

Another effect is that the lower exciton states (edge excitons) corresponding to different spin orientations are split by energy differences of a few meV. That means that thermally induced transitions between these levels can enable additional excitons for radiative recombination[50,51]. This effect practically eliminates the restrictions introduced by the selection rules, and opens the door to efficiencies higher than 25%.

2.2.2 Synthesis of II-VI semiconductor nanoparticles

In a review article on the subject, Eychmüller [52] defines a *good* nanocrystal preparation method as one that provides *"the largest possible range of particles sizes, narrow size distributions, good crystallinity, desired surface properties and, should the occasion arise, high luminescence quantum yields, as well as adjustable electronic properties"*. Certainly, several techniques have achieved high quality nanocrystal production in those terms, including both physical and chemical approaches.

Self-assembled epitaxy techniques have been employed to produce nanocrystals of the III-V group (see Wasserman[53] and references therein), especially those grown on GaAs substrates: GaSb, AlSb, InP and others. The procedure is based in the mismatch in crystalline structure between the substrate and the nanocrystal material. A good example is the production of InAs on a GaAs substrate, with a lattice mismatch of 7%. As the InAs is deposited onto the substrate, structural strain forces the InAs into nano-scaled agglomerates.

Electrochemical methods have been also employed for the production of nanocrystals. Penner[54] describes the formation of ZnO, CdS and CuI nanocrystals by depositing metal nanocrystals and subsequent chemical oxidation. Then, oxygen is substituted by liquid or phase reactions to form the desired semiconductor. Hodes and Rubinstein[55] describe the electrodeposition of single nanocrystals and aggregated films of CdSe, CdS and CdTe directly from the elemental constituents or their salts.

Here we will focus on the chemical routes for the synthesis of colloidal suspensions of II-VI semiconductor nanoparticles. Their flexibility in terms of surface properties and solvents make them suitable for a wide range of applications[56]. Also, concerning nano-structured inorganic semiconductors for photonic applications, nanoparticle colloids

completely dominate the literature. Colloidal nanocrystals are much smaller than epitaxially grown ones, therefore presenting stronger confinement effects[57].

The fabrication of nanocrystal colloids follows a general technique that was first proposed by Henglein[58]. The desired material is synthesized through a precipitation reaction in the presence of stabilizing molecules. The stabilizers are molecules that stick to the products, slowing down the reaction and preventing the formation and precipitation of large clusters or agglomerations. Small product nuclei capped with stabilizers are formed after the initial reaction, constituting the so-called *precursors*. These precursors are then grown in size through a process of refluxing at high temperature. Samples of solution can be taken during the process to monitor the growth of the nanoparticles. This is normally done by analyzing their photoluminescence and absorbance spectra. When the desired size is obtained, the process is interrupted. Post-production procedures are normally applied to improve the luminescent characteristics of the colloids.

There are two main chemical routes for the synthesis of high quality semiconductor colloids, defined in terms of the kind of reactants: the organometallic route and the aqueous route. The organometallic route employs phosphines as stabilizers, typically trioctylphosphine (TOP) and trioctylphosphine oxide (TOPO)[47,59]. This technique has been successfully used to produce high quality CdSe nanocrystals and CdSe core/shell structures[60]. Many semiconductors have been synthesized through this route: CdTe[47,61], InAs and InAs/shell[62], PbS[63], and particularly high quality CdSe[47,59] nanocrystals, and CdSe and CdTe core/shell structures[60,64]. However, it presents a series of issues and dangers that might favour the use of alternative techniques. The source of cadmium is commonly dimethylcadmium (DMCd, $Cd(CH_3)_2$), a pyrophoric, explosive, corrosive and extremely toxic compound. Also, the precipitation reaction takes place at high temperature, typically around 300ºC. These factors make this route expensive, dangerous and difficult to scale up. Also, problems of reproducibility with the organometallic route have been reported for CdS and CdTe[65,66].

The aqueous route employs water-soluble stabilizers like polyphosphates[67] or, more commonly, thiols[30,48,68-71] (Figure 15). The source of cadmium is cadmium perchlorate ($Cd(ClO_4)_2$), far less dangerous than DMCd, and the reactions take place at 100ºC. Gaponik et al.[71] estimated that the aqueous route for the production of CdTe

nanocrystals was eight times cheaper than the organometallic route for CdSe, and *orders of magnitude* cheaper than organometallic core-shell structures. The aqueous route also allows the fabrication of smaller nanocrystal sizes than the organometallic, although the degree of crystallinity is not as high because of the lower reaction temperatures. Sulphur atoms from the stabilizer molecules attach to cadmium atoms on the nanocrystal surface, forming a kind of CdS shell that provides additional luminescence stability[71,72]. Another advantage of the aqueous route is the possibility of selecting the nanoparticle surface charge by a correct choice of the capping material. This is an essential feature for nanocrystal deposition methods based in Coulomb interactions, like electrophoresis and the layer-by-layer technique[73].
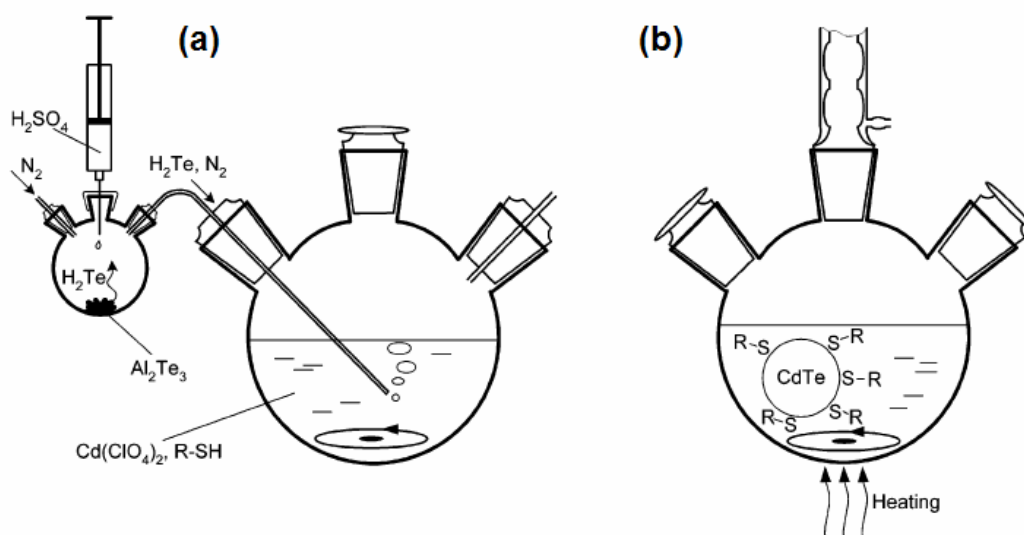
Figure 15. The aqueous route for the fabrication of CdTe nanocrystals. (a) The precursors are formed by bubbling H2Te into a solution of cadmium perchlorate and stabilizers. (b) After this, the solution is refluxed and the nanocrystals start growing.

2.2.3 Cadmium chalcogenide nanocrystals. CdTe.

The chemical control in the production of colloidal II-VI nanocrystals has been already well established[40]. Among them, perhaps the most extensively studied are the cadmium chalcogenides CdS, CdSe and CdTe (Figure 16)[47,48,68]. Highly efficient nanocrystals of these semiconductors have been produced covering the whole visible spectrum[47,64,66,74,75]. Some of their properties are presented in Table 2, together with their range of size-tunability.

CdTe is extensively used for the fabrication of nanoparticles for photonic applications. The main reason for this is its relatively large exciton Bohr radius, 15nm[27] (Table 2). Bulk CdTe is a direct semiconductor with a band-gap of 1.56eV. Its absorption peak in the near infrared has justified its use in solar cells, frequently doped with mercury. Alternatively, its transparency at wavelengths in the range 18-27μm makes it useful for infrared optics[76]. Due to the high atomic number of tellurium and zinc, CdTe and ZnCdTe are used in X-ray and gamma ray detectors[77]. Colloidal CdTe nanocrystals can be fabricated through both the organometallic[47,61] and aqueous route[48,71,72]. Quantum size effects allow the fabrication of CdTe nanocrystals emitting in almost the whole visible spectrum (Figure 17).
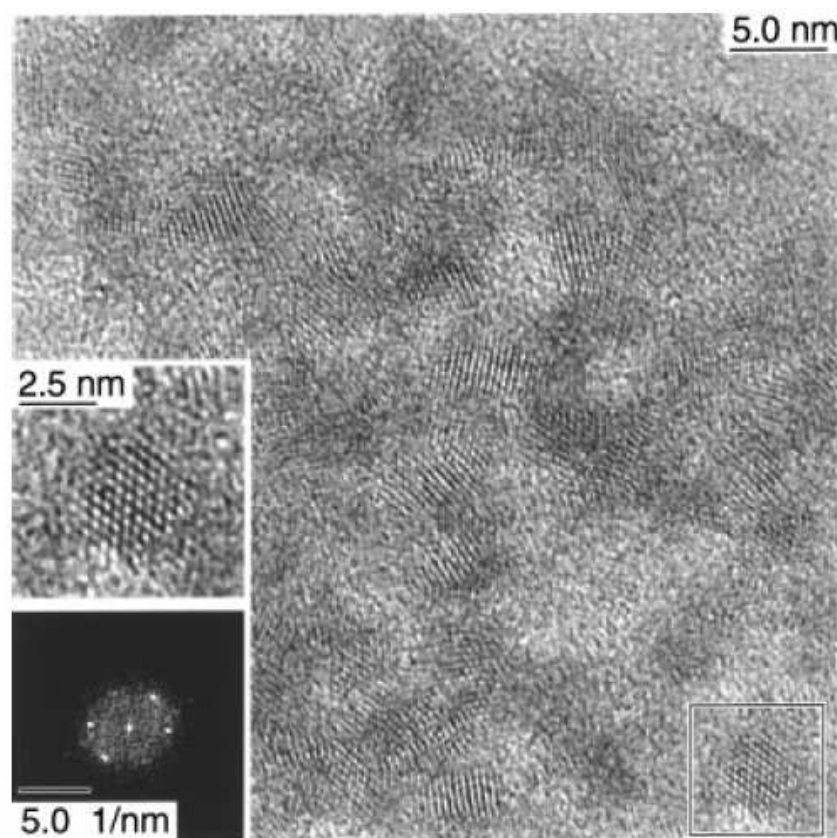
Figure 16. HRTEM picture of CdSe nanoparticles. The insets show a close look at a single particle and its fast Fourier transform (FFT). [After Rogach et al. (1999)[69]]

Table 2. Some properties of CdS, CdSe and CdTe. Sources are: (*) Berger et al. (2000)[23], (†) Gaponenko (1998), (‡) Ingert et al. (1999)[27], (§) Alivisatos (1996)[40] and (**) Gaponik et al. (2002)[71].

	Bulk band-gap (eV)	Bohr radius (nm)	Tunability range (eV)
CdS	2.42*	2.8†	4.5-2.5§ (UV-Blue)
CdSe	1.74*	4.9†	2.4-1.7§ (Blue-NIR)
CdTe	1.56*	15.0‡	2.4-1.7** (Blue-NIR)

Figure 17. Size-dependent photoluminescence of CdTe NCs synthesized in water. The smallest particles emit green, the largest red. (Image courtesy of Dr Nikolai Gaponik, Technical University of Dresden, Germany).

2.2.4 The layer-by-layer (LbL) technique

I. Langmuir and K.B. Blodgett[78,79] reported the first experiments on the deposition of molecularly controlled monolayers of fatty acids on solid substrates in the 1930s. Since then, a wide variety of self-assembly techniques have been employed for the incorporation of molecular layers to substrates with variable degrees of success. Here, the focus will be on the layer-by-layer technique with polyelectrolytes, developed by Decher and collaborators in the 1990s[80-82](Figure 18).

The LbL technique is based in the consecutive deposition of polymers with opposite electric charge. The process consists of dipping a substrate in alternated solutions of polycations and polyanions, that adhere to each other by the Coulomb forces between

their opposite charges. The substrate itself is normally charged either positively or negatively, and the charge of the first polyelectrolyte is chosen accordingly.

Polyelectrolytes are molecules that contain functional groups along their molecule that become ionized when dissolved. In this ionization, part of the functional group breaks up from the molecule, forming the so-called counterion, leaving the molecule charged with the opposite charge. Polymers can posses several charge centres per molecule; this provides an advantage for better adhesion to the surfaces when compared to small molecule species.
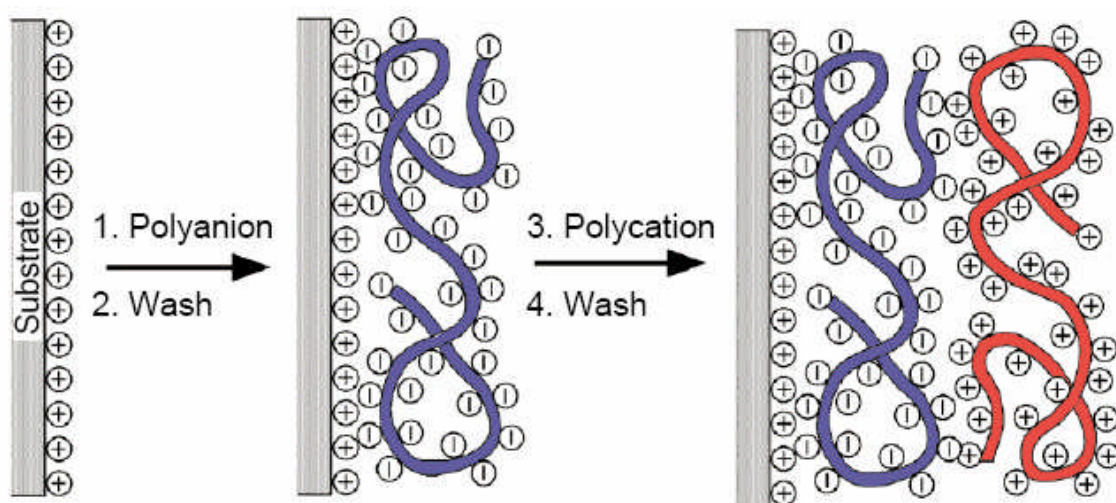
Figure 18. The layer-by-layer technique consists in the alternate dipping of the substrate in oppositely charge polyelectrolytes. Coulomb forces cause the adhesion of the layers. After Decher (1997)[82].

Polyelectrolyte molecules in solution can be stretched in linear chains or agglomerated in blobs. The stiffening or agglomeration is regulated by the minimization of the potential energy of the molecular chain[83]. Re-absorption of counterions reduces the Coulomb repulsion between charged centres and promotes molecule shrinkage and the formation of globules. Charged centres in shrunk molecules are less accessible than in stretched molecules. Thus, it is desirable to keep the molecular chains stretched in the solution for better adsorption onto the substrates. The addition of salt to the polymer solutions induces a beneficial chain stiffening[83,84]. Between each polyelectrolyte deposition, a washing step helps removing weakly absorbed polymer molecules and the cross-contamination of the different solutions.

The success of the technique is based on several key features[82]. The process is practically independent of the substrate and its surface morphology. This is due to the flexibility of the polymers, bridging underlying defects. Also, the repulsion between molecules of identical charge prevents the formation of aggregates and favours the smoothness of absorbed layers. Although originally conceived for polymer multilayers, the technique can be effectively employed with other charged materials. The surface charge of the nanoparticles can be chosen in some manufacturing processes, like the aqueous route for semiconductor nanoparticles. Thus, it is possible to fabricate multilayered structures made of semiconductor nanoparticle monolayers alternated with polymers of opposite charge[85-87] (Figure 19 and Figure 20).
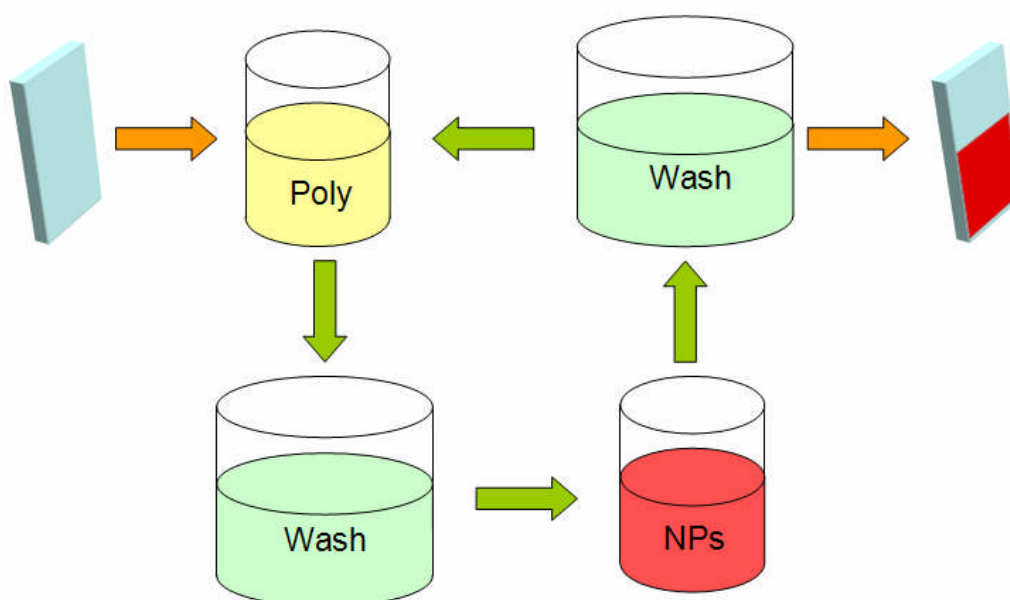
Figure 19. The layer-by-layer technique adapted to the deposition of semiconductor nanoparticles (NP). The substrate is dipped into the polymer solution to deposit a first layer of polyelectrolyte. Then, the substrate is washed to eliminate weakly bounded molecules and to prevent contamination of the nanoparticles suspension. Then follows a dipping into the nanoparticles suspension, for time enough to achieve surface saturation of nanoparticles. After another wash, the cycle can be repeated until the desired number of layers is obtained.

Poly(ethylenimine) (PEI) has been extensively used as first-layer polycation[81,85,89-92]. Its branched molecular structure favours its adsorption into negatively charged substrates, like ITO coated glass slides. Poly(dimethyl-diallylammonium chloride) (PDDA) is used for subsequent layers due to the linearity of its molecule[4,87,91]. This linearity reduces the

number of dangling molecules and protuberances at the surface, favouring smoothness and homogeneity of the multilayer.
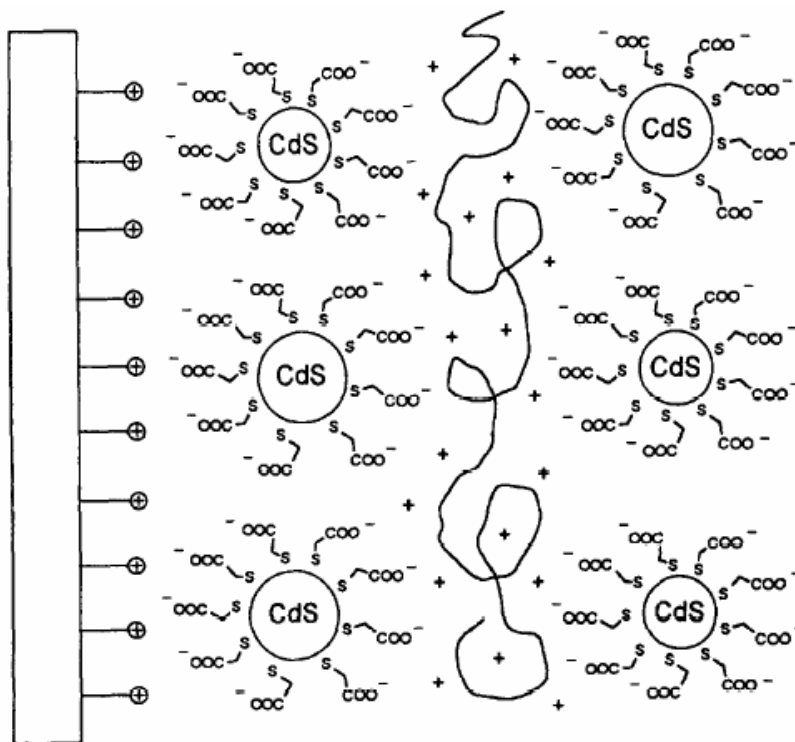
Figure 20. Illustration of the LbL technique applied to CdS nanocrystals. The nanocrystals have a negatively charged surface due to the carboxylic groups of the capping agent (mercaptoacetic acid). The polycation is ionene (I-6-Me-BF4). The quartz substrate was covered with aminopropylsilane, in order to charge it positively. After Gao et al. (1996)[88].

2.3 Related technologies for light emission

This section covers organic and hybrid LEDs. Currently, many groups researching LEDs use semiconductor nanoparticles in conjunction with organic films. The idea consists of exploiting the advantages of each type of material: the spectral purity of nanocrystal emission, the flexibility of OLED deposition techniques, the variety of conducting organic semiconductors, etc. Thus, a brief introduction to the optoelectronic properties of organic materials is necessary.

2.3.1 OLEDs

Although electroluminescent organic materials have been known since the 1960s, it was during the last decade of the twentieth century that significant progress was achieved in terms of luminance and efficiency. Since the 1990s, a plethora of new electroluminescent organic materials have been employed either in single layer or multilayer devices. Commercial OLED based products are already present in the market, signalling the maturity of the technology[93].

Earliest devices were based in highly insulating organic crystals like anthracene[94]. These devices required operating voltages in the order of 600V and luminescence was very low. Some efforts managed to reduce the operating voltages down to 30V, but with no improvement in efficiency[95]. In 1987, Tang and VanSlyke[96] produced a p-n device based in evaporated diamine and 8-hydroxyquinoline aluminium (Alq3), sandwiched between ITO and Mg:Ag electrodes (Figure 21). The device, with an external quantum efficiency of 1% and brightness greater than 1000 cd/m^2 at 10V, marked an inflexion point in the development of OLEDs. The success was due to the introduction of Alq3, a new fluorescent organic molecule of the family of the metal chelates, with good electron conducting properties[97].
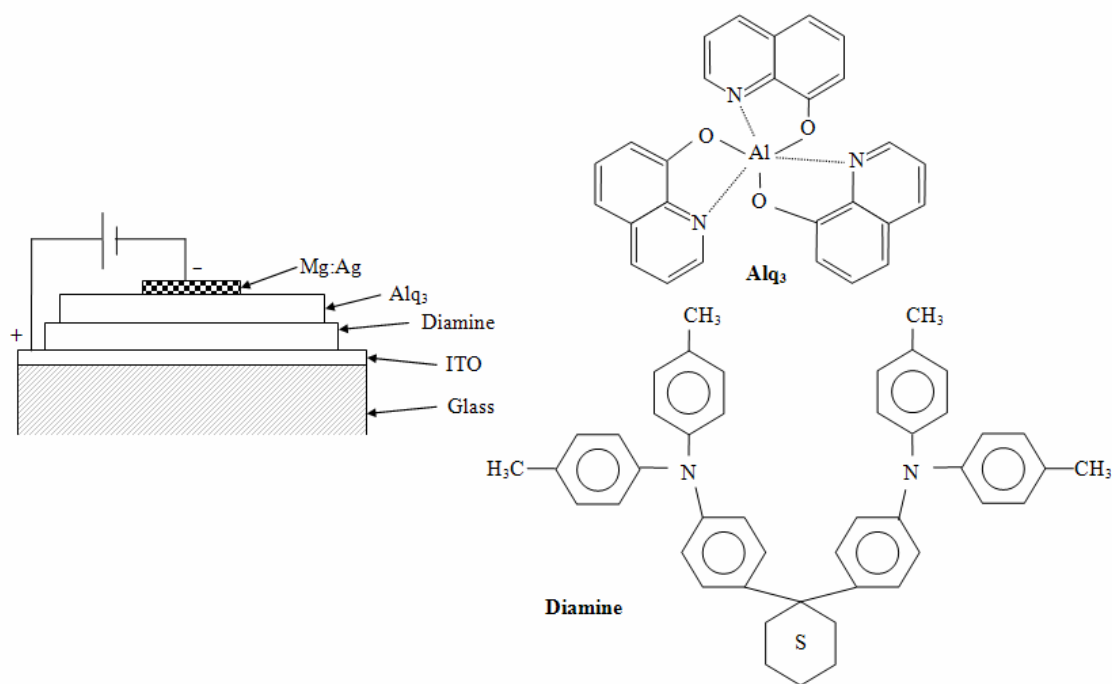
Figure 21. Tang and VanSlyke's device[96]. The luminescent material (Alq3) has good electron conductivity. The diamine layer was introduced to assist with hole injection (hole transport

layer). Both organic materials were evaporated in vacuum. This device, with a 1% external quantum efficiency and a brightness over 1000 cd/m^2, was the first highly luminescence OLED.

Burroughes et al.[98] reported the first OLED based in conjugated polymers (poly-p-phenylene-vinylene, PPV) (also known as PLEDs). The conducting behaviour is associated to carrier delocalization at π orbitals, induced by chemical doping[99]. Also, PPV can be manufactured into high-purity films with strong photoluminescence. The manufacturing procedure starts with the polymerization in water/methanol of a precursor polymer. Then the solvent is removed and redissolved in methanol. At this point, the precursor can be deposited onto a substrate and then converted into PPV at 250ºC in vacuum. Spin coating was a suitable deposition technique, providing good uniformity and control of thickness. This was one of the major advantages introduced by Burroughs et al., as sublimed organic films had presented re-crystallization and other structural problems.

Parker et al.[100,101] (Figure 22) found field injection responsible for carrier injection in MEH-PPV (poly-2-methoxy-5-2'-ethyl-hexoxy-PPV) and in PANI (polyaniline). They argued that the low carrier concentration in the polymer justified a rigid-band model, i.e. no band-bending due to carrier depletion or accumulation. Tomozawa et al.{Tomozawa, Braun, et al. 1989 #2330} and Braun et al.{Braun & Heeger 1991 #2160} supported the tunnelling model in MEH-PPV and in poly(3-hexylthiophene) devices. However, Karg, Meier and Reiss[104,105] proposed a Schottky barrier in PPV devices, arguing that band bending was introduced by interface reactions with the metal electrodes.
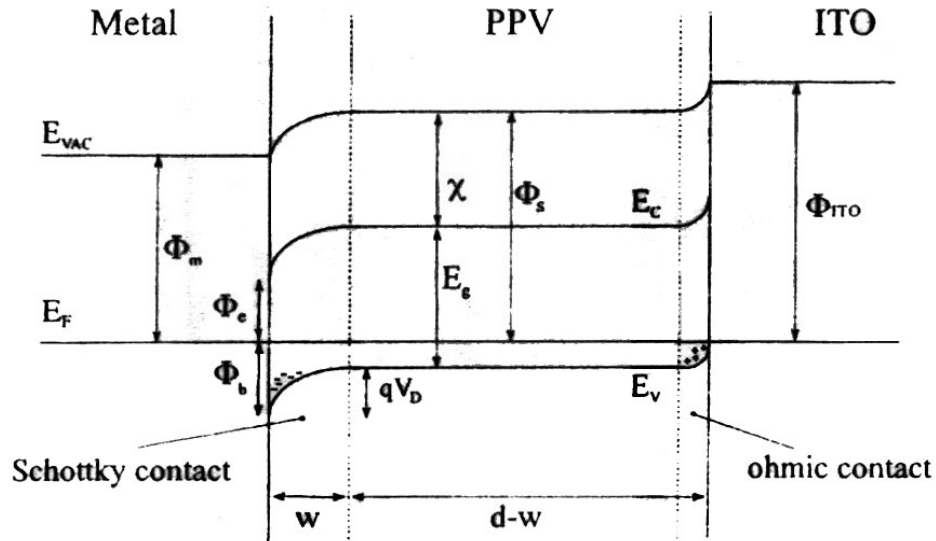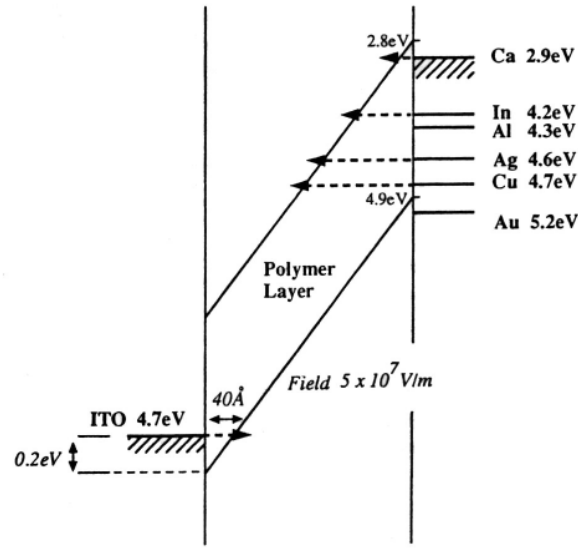
Figure 22. Charge injection into OLEDs. Parker et al. proposed a rigid-band model for the polymer, based on its low carrier density (left). Karg et al. proposed a model based on band bending, as they found evidence of interfacial charges due to chemical reaction between the polymer and the metal electrodes.

Charge injection takes place in the form of single carrier (electron or hole) polarons at the interface with the electrodes[98,103]. These polarons migrate through the structure and a fraction of them combine to form a polaron exciton. Light emission is generally obtained through direct recombination of these excitons[98,103].

In devices made of a single organic layer, one carrier is preferentially injected over the other (unless the barriers for hole and electron are perfectly symmetrical or zero).

Exciton formation will take place near the electrode with higher injection barrier; the proximity of the electrode may reduce luminescence due to quenching effects. Also, the conductivity is likely to be higher for one of the carriers; in this case, the probability of these dominant carriers crossing the structure without recombining (*leakage current*) will be high[106,107].

Tang and VanSlyke[96] had shown the benefits of a hole transport layer (diamine) in providing holes to an electron-conducting luminescent layer (Alq3). Adachi et al.[106] did the opposite with an electron transport layer (PBD, an oxadiazole derivative) and a hole-conducting luminescent material (NSD, a triphenylamine derivative), achieving an efficiency improvement of 10^4. As Adachi and collaborators explain (Figure 23), the electron transport layer (in their case) increases the number of electrons arriving at the interface, at the same time that it blocks the hole leakage current. Also, the recombination takes place at the organic-organic interface, reducing the quenching effects of the electrodes. Brown et al.[107] extended this concept to spin-cast PPV, adding a PBD/poly(methyl-methacrylate) electron transport layer. An improvement in efficiency of almost 10 was achieved.

The spectrum of emission of OLEDs is generally selected by varying the composition of the polymer[108,109], although it can be modified by changing the number and thicknesses of the polymer layer(s)[15], by doping the organic layer with other substances[110-112], and by their inclusion in optical cavities[113].
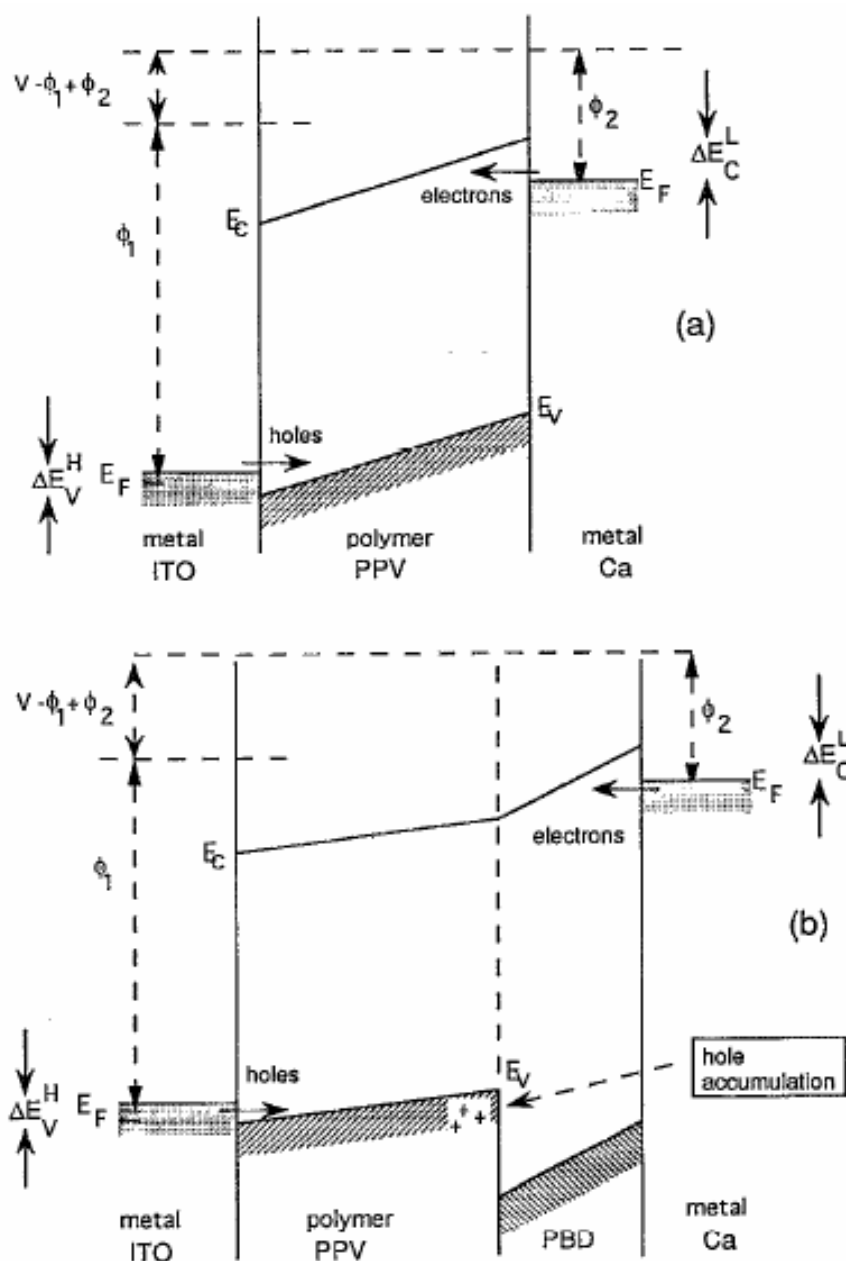
Figure 23. The effects of an electron transport layer (PBD) in an OLED with a hole-conducting luminescent layer (PPV). The electron transport layer increases the affluence of electrons to the organic-organic interface. Also, it blocks holes at the interface, creating a hole accumulation at the PPV side of the interface. Finally, the electron-hole recombination area is taken away from the electrodes and their quenching effects. That way, the efficiency of the bilayer device can be substantially higher than in single-layer devices. After Brown et al. (1992)[107].

Several modifications to the basic structure have been reported. Self-assembled polymer multilayers have been used to reduce the incidence of film defects and improve the efficiency of the devices[89,114,115]. Fou et al.[89] noticed an improvement in efficiency in PPV devices when a dielectric layer (polymethacrylic acid, PMA) was introduced in the

structure before the deposition of the metal cathode (aluminium). First they attributed this improvement to a reduction in the quenching effects by the metal cathode. Later[114], they proposed also a reduction in the band-bending at the interface with the cathode, reducing the barrier to electron injection. Hung et al.[116,117] also found an efficiency improvement in Alq3 devices when depositing a thin film of LiF or MgO between the organic layer and the aluminium cathode. They offered an explanation based in a band-bending reduction in Alq3. However, Jabbour et al.[118] explained the efficiency improvement as a consequence of electric field concentration across the LiF layer (Figure 24). This field concentration led to an enhanced tunnelling of electrons into the organic layer, improving electron injection and, hence, recombination. Similar efficiency improvements have been reported using a poly(methyl methacrylate) Langmuir-Blodgett film onto PPV[119], and an aluminium oxide film onto Alq3[120].
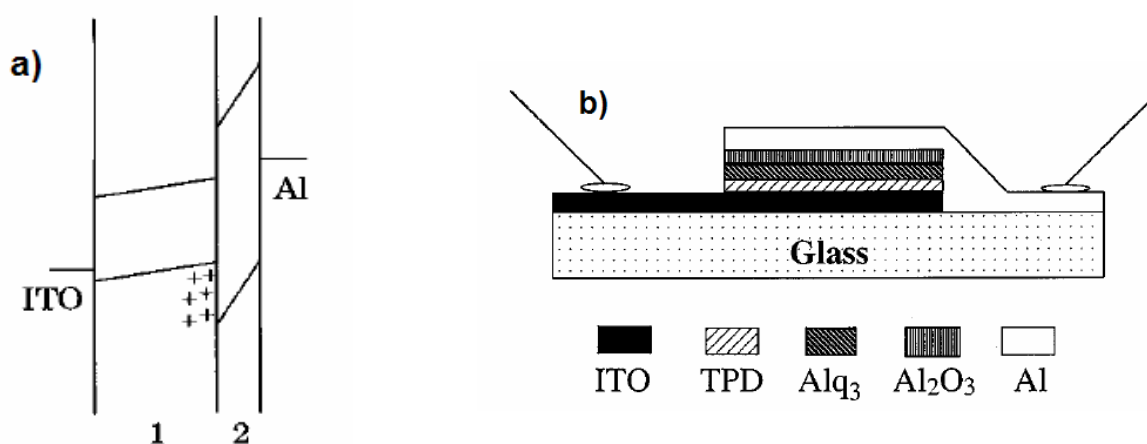
Figure 24. A dielectric film between the polymer and the cathode improves the efficiency in OLEDs. a) The improvement can be explained by the accumulation of charges in the polymer (1, PPV) at the interface with the dielectric (2, PMMA) [After Kim et al. (1996)[119]]. This accumulation enhances the field across the insulator, increasing the amount of electrons tunnelling from the cathode into the polymer. b) A picture of the device used by Li et al. A film of aluminium is evaporated on top of the Alq3, and is oxidized into Al_2O_3 by exposure to air. [After Li et al. (1997)[120]]

The main advantage of OLEDs is that polymers are amorphous. This eliminates the problems associated with the exhaustive control of growing conditions of crystalline materials. Also very convenient is the wide range of suitable solvents for polymer materials. These two characteristics allow a variety of simple deposition methods. Spin coating is a commonly used deposition technique for emitting polymers due to its

simplicity, offering at the same time good control of film thickness and homogeneity. Other techniques also frequently employed are thermal evaporation and layer-by-layer. Especially convenient for the generation of complex patterns are innovative techniques like ink-jet printing and screen-printing[113]. Features like these make of OLED a cost effective technology.

There are, however, a number of problems that OLEDs have to overcome in order to consolidate a position in the consumer goods market. Most of these problems are related to degradation phenomena that shorten the lifetime of the devices. The presence of oxygen or moisture within the device causes the photo-oxidation of the organic material and the quenching of the electroluminescence[121,122]. Oxygen and moisture also have been found responsible for device failure through cathode corrosion[123,124]. The elimination of these defects demand exhaustively controlled ambient conditions during film deposition, including an inert atmosphere.

The high electric fields applied during operation have been also considered as the origin of dark spots[125,126] (Figure 25 and Figure 26). Cumpston et al.[126] provided an explanation based on aluminium electromigration: regions of higher local field cause the electromigration of aluminium across the polymer, forming short-circuits. These short-circuiting filaments concentrate the current on them, then heat up and eventually fuse, leaving a non-emissive area.
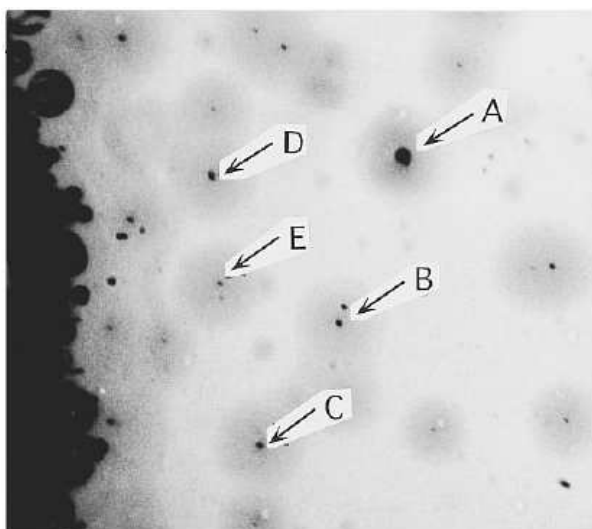
Figure 25. Dark spots in an Ag:Mg/Alq3/ITO device, as seen through the ITO electrode. The dark spots are associated with damaged areas of the top Ag:Mg electrode. [After Burrows et al. (1994)[125]]
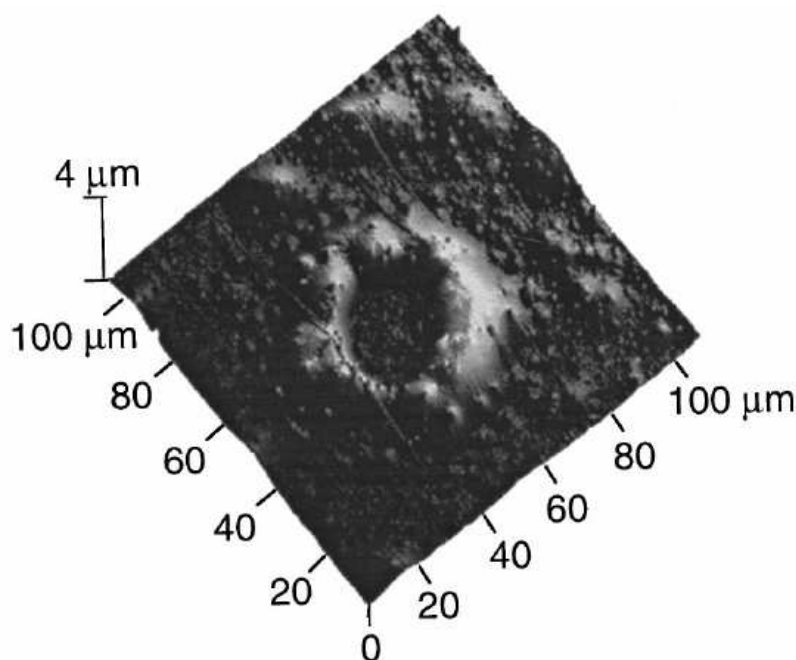
Figure 26. Close view of the metal electrode surface over a dark spot in an Al/MEH-PPV/ITO device. The crater-like structure is formed of aluminium atoms piled up due to electromigration at high fields.

Dark-spot occurrence have been also associated with the degradation of ITO electrodes at high electric fields[127-129] (Figure 27). Chao et al.[129] explained that ITO can start decomposing at field values around $1.0\text{-}1.6\times10^8$ V/m. The ITO decomposition releases oxygen bubbles that produce photo-oxidation damage, and a burst of tin ions that damage the polymer and cathode. However, Liew et al. (2000)[124] have discarded the changes in ITO morphology as a cause for dark-spot formation. For that, they washed the cathode and organic layer off a device substrate, and built a new device onto the recycled ITO. They found no correlation between dark-spot location in the new device and in the previous one.

Another degenerative effect found in OLEDs is known as intrinsic degradation[130]. It consists of a progressive loss of luminance associated to the operation of the device. The reasons for this effect are not clear yet, but currently it is the most limiting factor related to device lifetime. The rate of intrinsic degradation depends on several factors: material, device structure, colour of emission and operation conditions. The lifetime is dependent on time of operation and device particular properties. This causes *differential aging* effects that are major drawbacks for multi-pixel applications[131]. As can be found in the literature, organic luminescent materials present broader emission spectra than

solid state semiconductors; this can have a beneficial effect for white-light emission applications, but can be a problem for colour discriminating applications like computer screens[93].
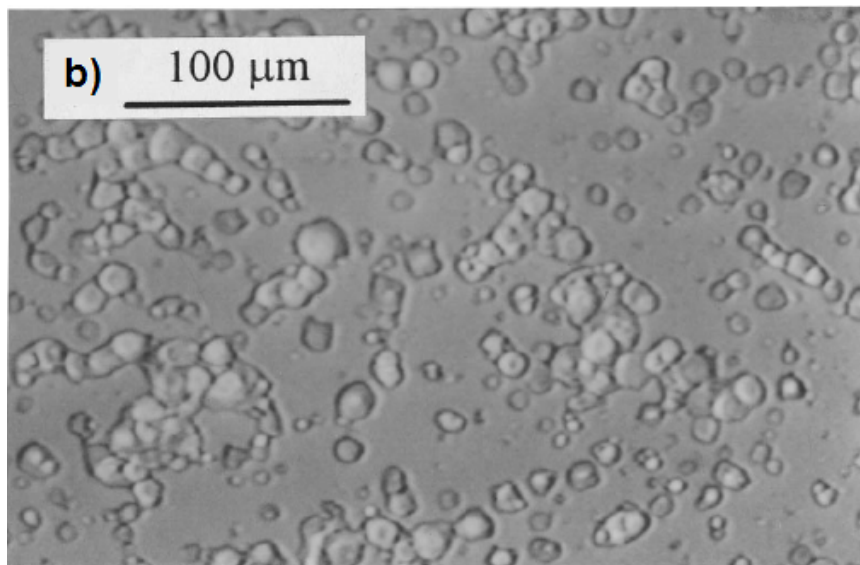
Figure 27. Damaged ITO electrode after operation at 50V. The electrode formed part of a Ag:Ca/poly(2-dodecoxy-p-phenylene)/ITO device. The damage is attributed to the decomposition of ITO under high electric field. [After Chao et al. (1996)[129]].

2.3.2 Hybrid organic-inorganic LEDs

There is not a specific definition for a hybrid LED. It generally refers to the combination of organic and inorganic materials in a light-emitting device. However, we will refer here as hybrid LEDs to those devices made with organic semiconductors and semiconductor nanoparticles. It was explained in Section 2.3.1 that luminescent organic semiconductors present good conduction and luminescence properties, but also a broad emission spectrum in general[93]. Inorganic semiconductor nanoparticles have excellent luminescence properties, with high spectral purity and luminescence efficiencies, but their conductivity is not as good in general. Hybrid devices try to combine the best properties of each material to produce, high luminosity with a high efficiency and spectral purity.

The first attempt in this direction was made by Colvin et al. (Figure 28)[16]. Their device consists of five layers of close-packed disordered CdSe nanocrystals bound by hexane

dithiol (a few hundred angstroms thick), and a 100nm thick layer of PPV (the deposition method for PPV is described as "*the standard method*", so spin coating will be assumed). The PPV layer is included with the double purpose of "*providing electrical stability and enhancing carrier injection and confinement*". They explain that, due to the low thickness of the nanocrystal film, the PPV is required to prevent dielectric breakdown of the device. The structure is sandwiched between an ITO anode facing PPV, and a magnesium cathode contacting the nanocrystal film.

In this configuration, the polymer and the nanoparticle films act as hole-transport layer and electron-transport layer respectively. Carriers accumulate at the polymer-nanoparticle film interface, concentrating the field at this plane. At low voltages emission from the nanoparticles dominates, whereas PPV emission dominates at higher voltages. The samples have to be limited in current to prevent *shorting* the devices, and luminescence starts to drop; no further comments are made regarding these effects. No environmental details are given. The turn-on voltage is around 4V, the luminance is 100cd/m^2 and the efficiency is around 0.001-0.01% (the authors were not very clear on this point). In reversed structures, with the carrier-transport roles exchanged between PPV and CdSe, the emission is substantially lower, and only PPV emits light. The turn-on voltage is 7V in this case.

Schlamp et al.[132] reported improvements on this structure by using CdSe/CdS core/shell nanocrystals. Nanocrystal films of 10, 20 and 40nm thickness are spin-cast on a PPV film 40nm thick (this later datum is not clearly specified). Samples are tested under argon flow at room temperature. The "*working field*", arbitrarily defined as the field required for a current of 10mA/cm^2, is 9×10^7 V/m and independent of the thickness of the nanocrystal film. I-V characteristics show two different regions, one ohmic and the second super-ohmic. The explanations they offer for these observations are confusing and incomplete, first referring to space charge effects or tunnelling, later dismissing them.
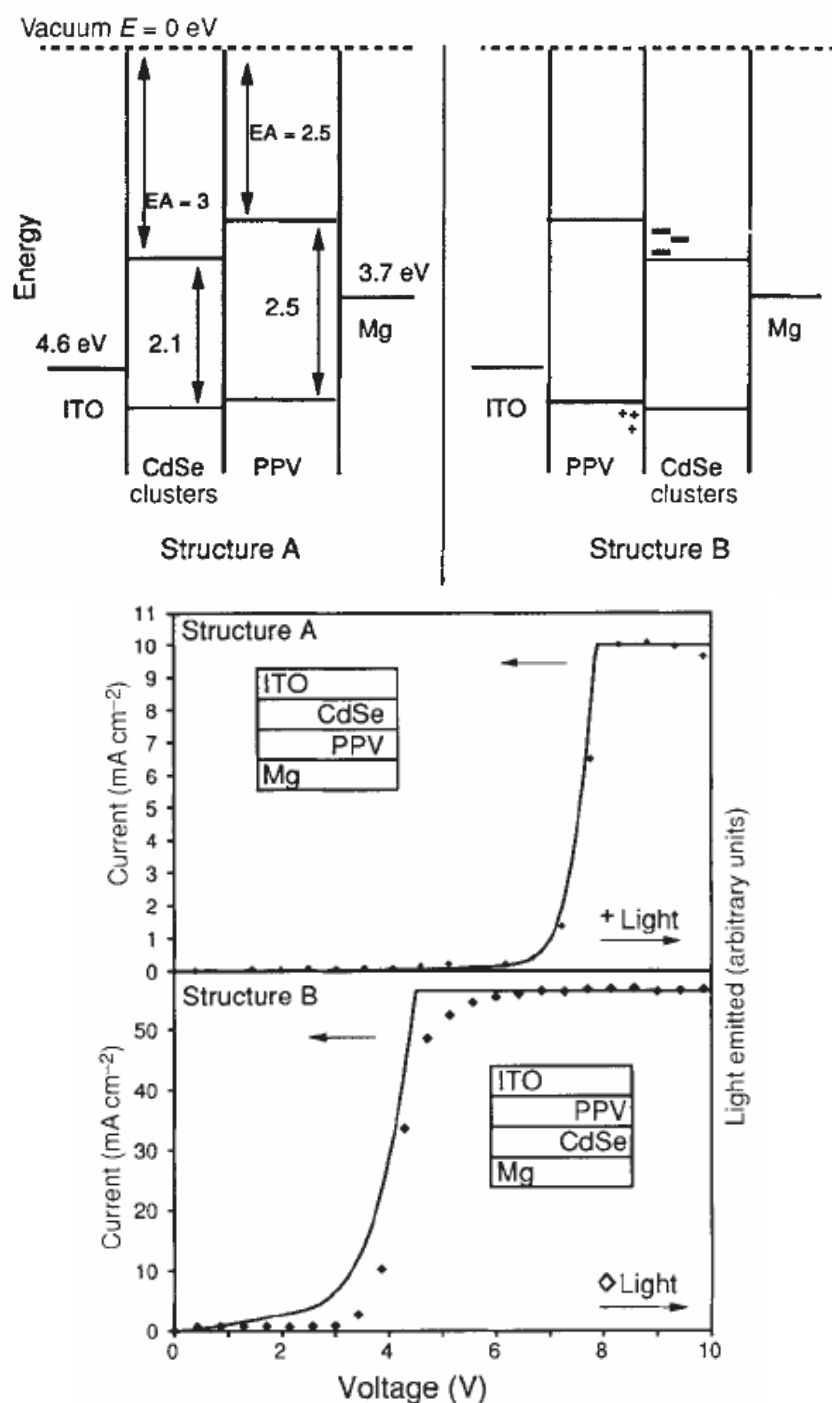
Figure 28. First hybrid device, as reported by Colvin et al.[16]. The device band diagrams on the left correspond to two different structures with inverted roles of CdSe and PPV. The corresponding I-V (solid line) and EL-V (dots) curves are plotted on the right. Structure B had better performance than structure A, due to a better level matching, and the poor electron conductivity of PPV. Turn on voltage for structure B was 4V, with emission from the CdSe for the lowest biases, switching to PPV emission as voltage went higher. Structure A had a turn-on voltage of 7V, with fainter emission, coming only from the polymer. Both types of structure had to be limited in current to prevent shorting.

A brightness of 600 cd/m^2 and peak efficiency of 0.2% are reported; both quantities saturate at 3 mA/cm^2, even below what they define as working field, but the authors do not comment on these details. The PPV contribution to emission decreases as the thickness of the nanoparticle film increases. EL from devices operated at 10 mA/cm^2 (at 0.03% efficiency) decay to 80% of the initial value after 200h. This degradation is associated with the oxidation of the polymer and the nanocrystals. Similar results were obtained by Mattoussi et al.[37], using the LbL technique for the deposition of PPV, and operated in air. They also tried using CdSe/ZnS core/shell nanocrystals, with better photoluminescence efficiency than bare CdSe nanocrystals. No improvement could be found in EL, however. This was explained by the band structure of ZnS, as it blocks hole injection into the CdSe. Gao et al.[86] reported a structure in which both PPV and CdSe were deposited by LbL, and operated in air. They report oxidation of the nanoparticles, and argue about the protective effects exerted by the PPV, although they later admit oxidation of PPV.

Another variation was introduced by Hikmet et al.[133], using poly (3,4-ethylene-dioxythiophene)-polystyrene-sulfonate (PEDOT) as a hole-transport polymer, and CdSe/ZnS core/shell nanoparticles. They report an electron-dominated current across the nanocrystal layer, with a voltage dependence that they attributed to space charge limited current.

Other structures are based in polymer/nanoparticle composites. Dabbousi et al.[3] mixed a hole-transport polymer (polyvinyl-carbazole, PVK) with an electron-transport polymer (PBD) in a 3:2 proportion, and then added CdSe dots at 5-10% in weight. A film of 200nm was spin-cast onto ITO (anode) and covered with aluminium (cathode). Devices operated in air show spectrally clean emission from the nanocrystals, with no emission from the polymers. However, the efficiency was very low, in the order of 0.0005%. Charged injection was attributed to tunnelling effects, according to the model introduced by Parker[100] (Section 2.3.1). Carrier transport was attributed to field assisted hopping. The authors could not distinguish whether the EL comes from electron-hole injection and recombination into the nanoparticles, or by Förster energy transfer. The reversibility of the structure is attributed to the close work function values of aluminium and ITO (they quote 4.28eV and 4.5-4.7eV respectively), indicating that the nanocrystals are not involved in charge transport. Other composites structures have been

fabricated with other materials (see for example Gaponik et al.[134,135]), but with no remarkable emission and stability characteristics in general.

In a different approach, Coe et al.[136] reported a hybrid structure in which the nanoparticles played no role in charge transport, but only in luminescence. The structure consists in a CdSe nanocrystal monolayer sandwiched between an electron-transport film (Alq3, 40nm) and a hole-transport film (TPD, 30nm) (Figure 29). The device shows a peak external quantum efficiency of 0.52% at 10 mA/cm^2, and a peak brightness of 2000 cd/m^2 at 125 mA/cm^2 (measurements in air) (Figure 30). The EL spectrum shows a small contribution of the Alq3. This contribution can be removed with the introduction of a hole blocking layer (3-(4-biphenyl)-4-phenyl-5-t-buthylphenyl-1,2,4-triazole, TAZ, 10nm) between the nanocrystals and the Alq3, but with an associated reduction in efficiency around 50%. No stability data is provided.
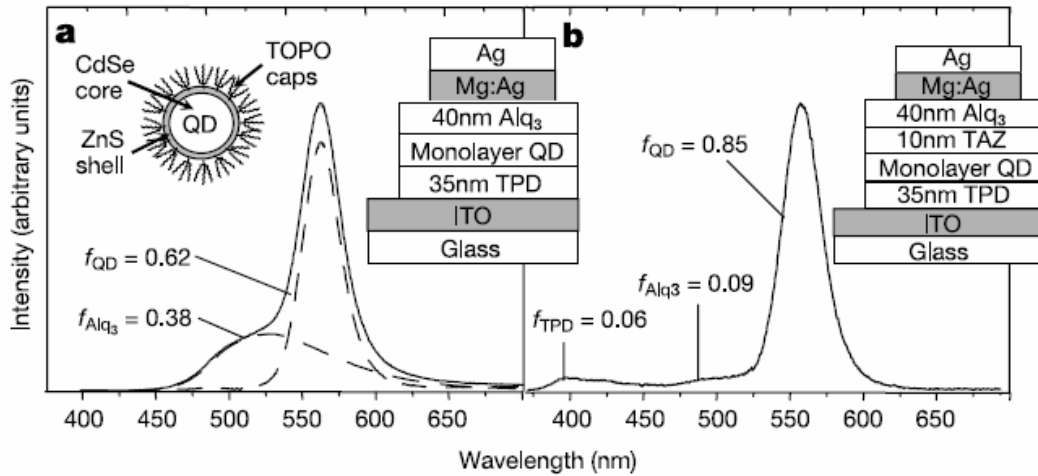
Figure 29. A hybrid device with electrically passive nanocrystals. (a) The nanocrystal layer is sandwiched between an electron-transport and a hole-transport layers (Device I). Electrons and holes are injected into the nanocrystals and recombine radiatively. A contribution to EL from Alq3 is noticeable in the EL spectrum. (b) It can be removed by inserting a hole blocking layer of TAZ (Device II), but with an associated reduction in efficiency around 50%. [After Coe et al. (2002)[136]]
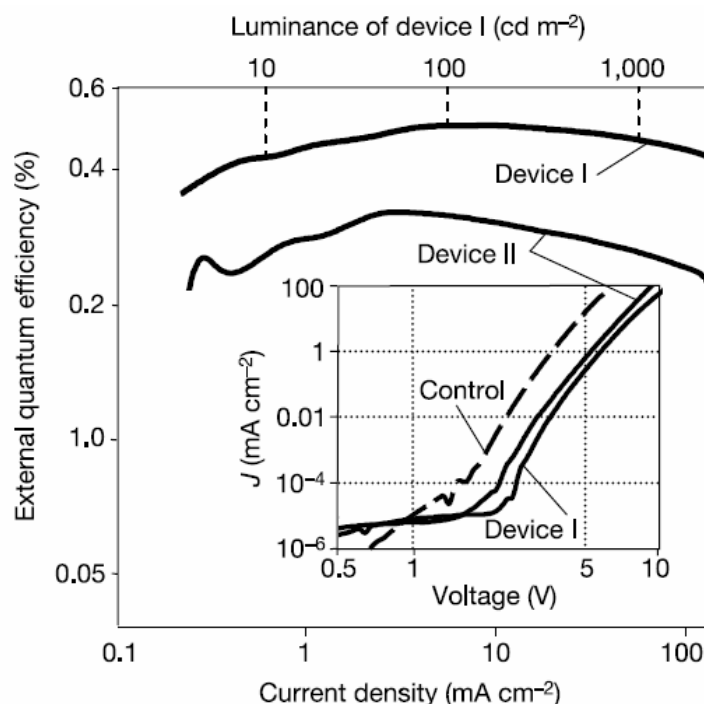
Figure 30. I-V and efficiency curves for the device of Coe et al.[136] The *control* sample is a TPD/Alq3 device, without nanocrystals.

In the device from Coe et al., the nanocrystals act purely as luminescence centres, and take no part in conduction. In all other structures, in general, it is difficult to distinguish the transport mechanisms due to the nanoparticles and those due to the polymer(s). There are also difficulties to characterize the potential barriers involved at the different interfaces. The knowledge gained in OLEDs about the transport mechanisms of semiconducting polymers is not easily extendable in general to hybrid devices, as the electrical characteristics of the nanocrystals modify the overall behaviour of the device. Thus, studies on electrical properties of pure nanocrystals films are necessary in order to further optimize hybrid devices. Also, the use of organic materials for charge transport still poses some of the degenerative problems found in OLEDs[86]. Moreover, the spectral characteristics of organic and inorganic materials for hybrid devices have to be chosen carefully if spectral changes through exciton and energy transfers[16,137] are undesired.

2.4 The all-inorganic Nano LED: NLED

The concept of the NLED refers to a device in which the electrical and emissive properties are due to inorganic nanomaterials only. The aim of this strategy is to isolate

the injection, conduction and emission properties of semiconductor nanoparticles from those of other materials. Also, dynamical degradation effects due to nanoparticles can be investigated in detail. That way, a better understanding of the opto-electronic properties of nanoparticle films is expected.

2.4.1 Energy levels and band diagrams

As presented in section 2.2.1, nano-structured materials have properties that are intermediate between molecules and solids. This may introduce difficulties when dealing with some properties defined in the context of the solid-state theory of bulk semiconductors[40]. An example of these difficulties is the lack of details about carrier densities, mobilities and the position of the energy levels in the nanoparticles[3,37]. The position of the conduction and valence band in nanocrystals is usually approximated from bulk values and bandgap measurements[4,37,137,138]. The position of the Fermi level depends on the stoichiometry of each nanocrystal. Impurities and defects will also affect significantly the shape of the Fermi surface. Thus, it is possible that a range of values for these parameters are found within an ensemble of nanocrystals.

Another difficulty concerns the formation of metal-semiconductor contacts. It is not clear whether it is possible to apply the theory of bulk metal-semiconductor contacts to devices made of nanoparticles. The concepts of charge depletion and band bending used in Schottky barriers involve a continuous semiconductor and spatial dimensions far greater than the size of a nanoparticle[24,139] (e.g. diffusion lengths and depletion area lengths are in the order of micrometres). Moreover, the discontinuity of the nanoparticle multilayer might prevent charge rearrangement, due to poor carrier mobilities (similar problems have been discussed for OLEDs, see Section 2.3.1). The case is even more dubious if these nanoparticles are embedded in a dielectric host.

Due to these limitations, it is impossible to work with an accurate picture of the energy levels involved in a device. Researchers resort to a static band diagram for the analysis of charge injection and transport[6,16,37,132,133,136-138] (see Figure 31). In the static band diagram, the energy levels of a material are represented as if it were isolated from the rest of the device. When taken with due care, the static diagram allows first order

approximations for charge transfer between the different materials. We will adopt this approach for the analysis of the NLED structure.
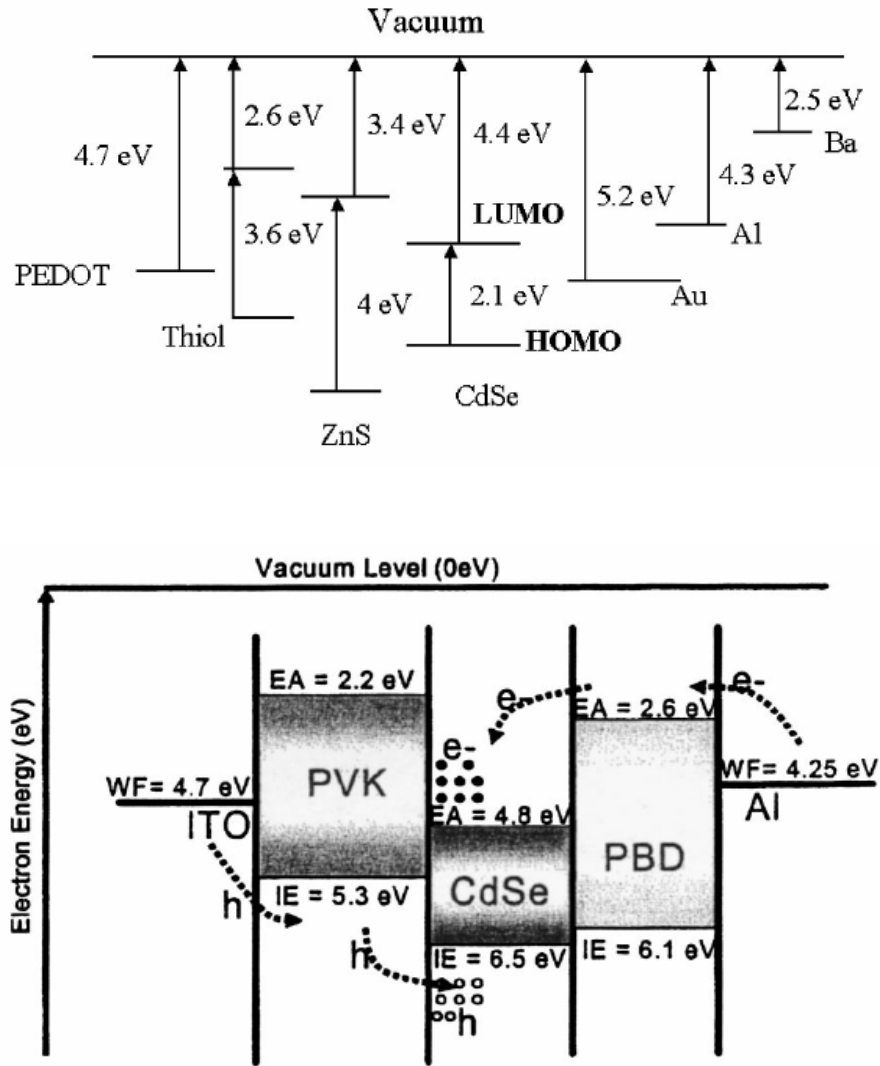
Figure 31. Exaples of static band diagrams. [After Hikmet et al. (2003)[133] (top) and Chaudhary et al. (2004)[6] (bottom)].

2.4.2 Related NLED literature

Currently, the only report of a pure NLED was given by Gao et al. [4]. They built structures identical to those of this work, using a layer-by-layer technique for nanoparticle deposition. PEI was employed over the substrate as first electrolyte, while subsequent polymer layers were made of PDDA. Both polyelectrolytes were dielectrics and played no active role in charge transport. The mean polymer/nanocrystal layer

thickness was *assumed* to be around 3nm, close to the size of the nanoparticles, although no additional details were given about this data. The authors compared current-voltage and electroluminescence-voltage characteristics from samples with 20, 30 and 50 layers of nanoparticles emitting at 622nm measured in air.

They found a field dependency on the current flowing through the device, with current densities in the range of a few mA/cm^2. No explicit calculation was done for the current onset field, although from Fig. 3 on their paper it can be deduced that its value was around $3\text{-}4\times10^7$V/m for the three samples. The origin of this field dependency is not further investigated, although it is attributed either to current injection by tunnelling or carrier transport by hopping. Mention is made to an unexplained shoulder of current for the 50-layer sample, and the possibility of some electrochemical reactions is suggested. It is made clear that this shoulder vanished in subsequent voltage sweeps accompanied with a decrease in electroluminescence. However, no further data is reported about the behaviour of subsequent sweeps in that sample or the others.

The electroluminescence turn-on point was ca. 2.5V for samples with 20 and 30 layers, with higher intensity for the 30-layer sample. For the 50-layer sample, the turn-on point was around 6.5V and the electroluminescence was *much lower* than the other two samples. The fact that the turn-on voltage for the 50-layer sample coincides with a notable increase in current was not investigated.

They also built 30-layer devices with CdTe nanoparticles of different sizes, corresponding to emission wavelengths of 549nm, 589nm, 622nm and 655nm. The electroluminescence turn-on point was in the range 2.5-3.5V for all the samples. Electroluminescence intensity, device efficiency and current density were found to be proportional to the particle size, except for the sample emitting at 655nm in which low levels of emission and current were obtained. This behaviour is attributed to differences in the position of the band edges caused by unequal quantum confinement effects. However, they found no explanation for the anomalous behaviour of the sample emitting at 655nm.

It was argued that electron conduction dominated in these samples. Devices comprising two different sizes of nanoparticles distributed in different halves of the structure were built to prove this point. However, the only data provided from these samples are two

electroluminescence spectra. Although the opinion about preferential electron conduction is shared here, this argumentation does not offer enough evidence. Since carrier injection and transport mechanisms are not explained satisfactorily, it is not possible to draw conclusions based on them.

Some short comments are made about the stability of the samples. It is mentioned that faster device degradation is associated with smaller nanoparticles, but no concrete evidence is presented. Stability problems are explained in terms of nanocrystal oxidation, but the reader is directed to Mattoussi et al. (1998)[37] and Gao et al. (1998)[86] for evidence. Despite the similarities, these two later papers are built with CdSe and PPV, and it is thought that substantial differences can occur, as will be discussed with the results. Stability issues might be obscuring the mechanisms of current injection and conduction. Additional research had to be performed to identify the causes of device degradation.

2.4.3 Charge injection

As discussed in Section 2.3.1, Parker et al.[100,101] proposed field emission as charge carrier injection mechanism in OLEDs. A rigid-band model was justified due to the low carrier concentration in the polymers. They also showed that, for optimal device efficiency, it is convenient to reduce to a minimum the barrier for charge injections. This is done by producing a good match between the Fermi levels of the electrodes and the edges of the band-gap: the anode must be aligned with the top of the valence band, and the cathode aligned with the bottom of the conduction band. They also argued that charge injection, and consequently light emission, started with the flat-band condition. According to this assertion, they defined the turn-on voltage as the flat-band bias, i.e. the energy gap E_g minus the two barrier offsets at the electrodes. In their devices, this offsets were in the order of 0.1-0.2eV.

Chalcogenide nanocrystals assemblies present high resistivity[5,136], e.g. Morgan et al.[140] reported a resistivity greater than 10^{14} Ω/cm in closed-packed CdSe nanocrystal arrays. Also, in NLEDs, the nanocrystals are embedded in a dielectric polymer matrix. Substantial charge mobility is not obtained until fields around 10^7 V/m are applied. These factors can justify the assumption of the rigid-band model and field injection as

carrier injection mechanism for NLEDs[4]. Hikmet et al.[133] investigated the influence of the work function of the electrodes, finding better emission for closer energy level matching. However, in NLEDs based in chalcogenides, the potential barrier for hole injection is in the order of 1-2eV, due to the high electron affinity of the semiconductor (4-5eV)[1,37,132,133]. The barrier for electrons depends on the semiconductor and the cathode material, with a value between 0.2-1eV. These offsets are substantially higher than the offsets found by Parker and collaborators in their devices. In consequence, it is believed that the flat band condition in NLEDs will be associated to the turn-on of the emission. At flat-band bias, the hole current will not be substantial, due to the high barrier for hole injection. The high turn-on voltage obtained by Gao et al. and Hikmet et al. suggest also this discrepancy with Parker's definition. Thus, the turn-on voltage has to be redefined, most suitably to that bias at which emission is first detected.

ITO is commonly used for hole injection, due to its (relatively) high work function and transparency in the visible spectrum, which allows light to escape from the structure. Reported ITO work function values spread from 4.3eV up to 5.2eV, depending on deposition conditions and subsequent surface treatments[141-143]. ITO can be treated in oxygen plasma to improve the conductivity and to increase the work function. Gold (5.3eV) anodes can be used in applications in which anode transparency is not required[98]. A material with a low work function is convenient for electron injection into the nanoparticles. Mg (3.7eV)[16] and Ca (2.9eV)[144] have been employed in organic and inorganic devices. Because of their high chemical activity and they are usually coated with Ag (4.4eV)[134,136] and Al (4.3eV)[145]. The latter is also commonly used individually in the literature[3,37].

2.4.4 Charge transport

In NLEDs, the semiconductor nanoparticles are arranged independently and surrounded with a dielectric polymer. The main conduction mechanisms in bulk semiconductors, field drift and carrier diffusion, will not be applicable in these structures due to the discontinuity of the semiconductor material. Mattoussi et al.[37] proposed hopping as the transport mechanism between CdSe/ZnS core/shell nanoparticles spin-cast on top of a PPV multilayer; at high electron injection level, transport might be affected by electron trapping at nanocrystal interfaces, leading to a space-charge limited (SCL) current.

Hikmet et al.[133] also found SCL electron conduction for the same particles and deposition method. However, Schlamp et al.[132] related the SCL current with the PPV rather than the nanoparticles, but could not clarify the mechanism responsible for charge transport between nanocrystals. Artemyev et al.[146] found evidence of hopping transport for drop-cast nanocrystals of CdS; however, Morgan et al.[140] could not clarify the mechanisms intervening in drop-cast films of CdSe, although indications of tunnelling and hopping where found. From the attempts reported in the literature, it seems that the effects introduced by other conducting materials obscure the nature of charge transport between nanoparticles.

2.4.5 Light emission

In its simplest form, the NLED has no p-n junction in its structure. The formation of excitons happens during the tunnelling or hopping events[146] in a way similar to exciton formation in single layer OLEDs. Charges trapped at the nanoparticles surface or at the nanoparticle-polymer interface help the formation of excitons[86]. The place of exciton formation and its rate depend on injection efficiencies and transport rates of each carrier. Due to the imbalance with hole injection (Section 2.4.3), the majority of the electrons will cross the structure un-recombined, and will reduce the device efficiency[37]. However, the discontinuous nature of the emissive layers will prevent high electronic leakage currents. Holes injected into the structure will encounter a high concentration of electrons; consequently, exciton formation is likely to happen near the anode. The existence of nearly-free electrons at the ITO electrode might induce some losses due to Auger processes[6,137].

3 Experimental

3.1 Substrates

The source of material for substrates is ITO coated glass from Merck, 1.10mm thick, a film thickness of 125nm and a sheet resistivity around $13\Omega/\square$, finished with a SiO_2 polishing layer. Sample substrates are made of cuts of 32mm×24mm. The substrates are brushed in soapy distilled water to remove SiO_2 flakes from the surface, and dried with nitrogen. Then, the substrates are cleaned in an ultrasonic bath first with acetone and later with isopropanol. Exposure to oxygen plasma (20% oxygen in argon) for 10 minutes at 20W follows, to help remove any remaining organic contamination.

Clean substrates are spin-coated with photoresist and exposed to UV light under a shadow mask with a pattern of 2mm-wide strips. The substrates are then developed to eliminate the photoresist from the unexposed areas. An etching solution is prepared with an aqueous solution of hydrochloric acid, 37% by volume. Substrates were etched for 40 seconds at 60ºC and then rinsed in distilled water. A careful examination was carried out with a multimeter; samples with conductive bridges were etched for extra time; samples with defective stripes were discarded. A cleaning procedure identical to the previous one follows; the plasma exposure is changed to 5 minutes and 50W, to induce oxygen adsorption by the ITO.

3.2 CdTe nanocrystals

The nanoparticles for this work were produced through the aqueous route reported by Gaponik et al. (2002)[71]. In this method, a solution of cadmium perchlorate and thiol stabilizers was prepared in a flask filled with nitrogen. Gaseous hydrogen telluride H_2Te is bubbled into this solution, forming CdTe precursors. Then the mixture was refluxed at 100ºC and CdTe nanocrystals start to grow. The colour of emission is monitored by taking aliquots periodically and measuring their photoluminescence. The emission changes gradually as the nanocrystals grow from green (510nm with a size around 2nm) to red (650nm with a nanocrystal size around 5nm). The reflux was interrupted when

the desired wavelength is achieved. Post-preparative treatments, based on size-selective precipitation and selective photochemical etching, were then applied to improve the PL quantum efficiency. The resultant colloids have up to 40% PL quantum efficiency and a FWHM between 35nm and 60nm for the smallest and largest nanocrystals, respectively. 1-thioglycerol and 2,3-dimercapto-1-propanol thioglycolic acid (TGA) were used as stabilizers to provide a negative surface charge to the nanoparticles used in layer-by-layer technique.

3.3 Deposition of nanocrystals multilayers

A layer-by-layer procedure was used to deposit the semiconductor nanocrystal multilayer. PDDA 20% weight in water, 200k-300k molecular weight purchased from Aldrich was used as polycation. A water solution 20mM in PDDA and 0.2M in NaCl is prepared by adding water, G Chromasolv from Aldrich (#34877). Earliest procedures used a first layer of PEI prepared in the same way as PDDA. The CdTe nanoparticles for LbL were capped with a mixture (1:1) of 1-thioglycerol and 2,3-dimercapto-1-propanol thioglycolic acid (TGA), to provide them with a negative surface charge. Nanoparticle suspensions with a concentration around 1mg/ml were diluted 1:3 in water, G Chromasolv from Aldrich (#34877). Substrate rinsing was made with filtered distilled water. For automated deposition, a Zymate II robotic arm from Zymark was used. Sample dipping was 10 minutes long in each solution, with a rinsing time of 2 minutes. The sample removal rate was programmed to be ≈1.18mm/s, so as to remove efficiently the solvents from the surface with the aid of gravity and surface tension. After the LbL procedure, samples were dried in low vacuum for 12h at room temperature.

3.4 Cathode deposition

Cathode deposition was carried out in an Edwards E480 thermal evaporator. A stainless-steel shadow mask was used on the samples to pattern the electrodes. Tungsten filaments and molybdenum boats were used for aluminium and gold deposition respectively. Aluminium was from Goodfellow, 0.25mm diameter wire, 99.5% purity. Gold was from Agar Scientific, 0.2mm diameter wire, 99.99% purity. Working

pressures were below 4×10^{-6} mbar. Film thickness was monitored with a piezoelectric sensor. Typical deposited aluminium and gold films were around 200nm thick. The deposition distance (distance between the boats and the samples) was either 15cm or 32cm.

RF sputtering of aluminium electrodes was also done in a Nordiko Sputtering system. However, severe loss of PL was caused to the samples by the plasma.

3.5 Absorption and fluorescence measurements

Absorption measurements were carried out in a Lambda 7 UV/Vis spectrophotometer from Perkin-Elmer. For nanoparticle liquid phase absorption, source nanoparticle colloidal suspensions 1mg/ml in water were diluted 1:20 in water, G Chromasolv from Aldrich (#34877). For on-substrate nanoparticle absorption, 5 layers of nanoparticles were deposited by LbL on a soda-lime glass slide. Comparative PDDA and PEI absorption spectra were recorded from single polymer+nanoparticle layers deposited by LbL on soda-lime glass.

Fluorescence measurements were performed in a Cary Eclipse spectrofluorimeter. Nanoparticle suspensions were diluted 1:20 in water, G Chromasolv from Aldrich (#34877).

Rapid device photoluminescence checking was done by illuminating the samples with a UV lamp emitting at 365nm (20W).

3.6 Current and electroluminescence measurements

Current-voltage measurements were done using a Keithley 6517 electrometer operated as a source-meter. The voltage step was 0.05V. A silicon photodiode OPT-301 from Texas Instruments collected the light from the device. The integrated amplifier was used with the internal 1MΩ feedback resistor, with a nominal responsivity of 0.47V/μW at 650nm and extrapolated responsivity of 0.35V/μW at 625nm. The photodiode was biased with a regulated $\pm$15V power supply. The photodiode was mounted on a holder

with mobility in three axes. The signal from the photodiode was measured with a Keithley 195A digital multimeter.

The 6517 electrometer and the 195A multimeter were remotely operated from a computer through an IEEE488 connection. A specially designed program coordinated the measurements, and the data collected was stored in electronic format.

4 Results and discussion

4.1 Structure development

In this section, the work carried out to develop a reliable manufacturing route for an NLED will be presented. Although structural problems were not the central issue of this work, the development of a manufacturing technique capable of providing repeatable results was a key factor for further investigations. It is not possible to study the dynamics of a device when the behaviour varies widely and unpredictably among a set of samples manufactured in an identical process.

A further factor is sample stability. The first voltage sweep carried out in a sample is prone to develop singular shoulders or current spikes if some structural imperfections are present. These features are normally smoothed or removed during the first voltage sweep due to the electric current, in what are called electroforming effects. However, these electroforming mechanisms can cause morphological changes in the samples, especially if they involve large currents. The consequence is that subsequent ramps can vary substantially. In the available literature no examples were found of consecutive current-voltage (I-V) sweeps for the same device. Consequently, it is very difficult to distinguish which features are general and which ones correspond to forming effects or peculiarities of an individual voltage ramp. A manufacturing procedure that ensures the minimal introduction of structural defects leading to electroforming features is key for the study of device dynamics.

In this section, it will be shown that the commonly employed manual LbL procedure led to numerous structural inhomogeneities. These inhomogeneities were the cause of electrical failure of the samples and poor electroluminescence. Several modifications were introduced in the LbL technique. These modifications provided important improvements in sample homogeneity that resulted in a reliable manufacturing procedure for functional structures. Electroforming effects were reduced substantially, allowing the repetition of electrical tests on individual devices. Improved stability in time also enabled the use of spectrometric techniques to evaluate light emission properties.

4.1.1 The layer-by-layer (LbL) method

Initial tests with this technique involved a manual dipping procedure into the different solutions, with the aid of a pair of tweezers. Photoluminescence inspections revealed a homogeneous substrate coating, and the intensity of the photoluminescence indicated a high density of nanocrystals. However, current-voltage (I-V) measurements had poor success. High current densities (in the order of 100 mA/cm^2) where obtained from most of the devices even at low voltages (1.0-2.0 V). Current spikes and device sparking signalled electric failure. A high proportion of devices showed ohmic profiles. These were clear indications of the presence of pinholes and short-circuits within the structure. After sample biasing, PL loss was revealed after inspection under UV light. This was attributed to the development of Joule heating within the structure, with some substrates cracking due to thermal shock. Light emission was achieved only from a low percentage of devices. The short duration of light emission prevented the completion of spectral analyses. The emitted light, though faint, was visible to the naked eye and of a red colour.

Pinholes and short-circuits were attributed to porosity and non-uniformity of the CdTe multilayer. A series of roughness and thickness measurements were performed with a stylus profilometer. Results obtained for the roughness and thicknesses of the different layers are reported in Table 3. They revealed that the layered structure presented a roughness higher than 30% of the multilayer thickness. The thickness of a single layer of nanoparticles was ~30nm.

Table 3. Roughness and thickness measurements on 10-layer CdTe devices obtained with a profilometer. It is remarkable the high roughness of the CdTe multilayer.

Material	Roughness (average, nm)	Thickness (nm)
Glass	10	-----
ITO	10	150
CdTe (10 layers with PEI/PDDA)	100	300
CdTe (1 layer with PEI)	5-10	30

These results were confirmed by SEM analysis on samples with 10 layers of CdTe (10×[PDDA+CdTe]). As can be seen from Figure 32, the multilayer thickness was very

inhomogeneous. With an average value around 300nm, this thickness indicated a 30nm-thick layer, in contrast to a particle size of 3nm.
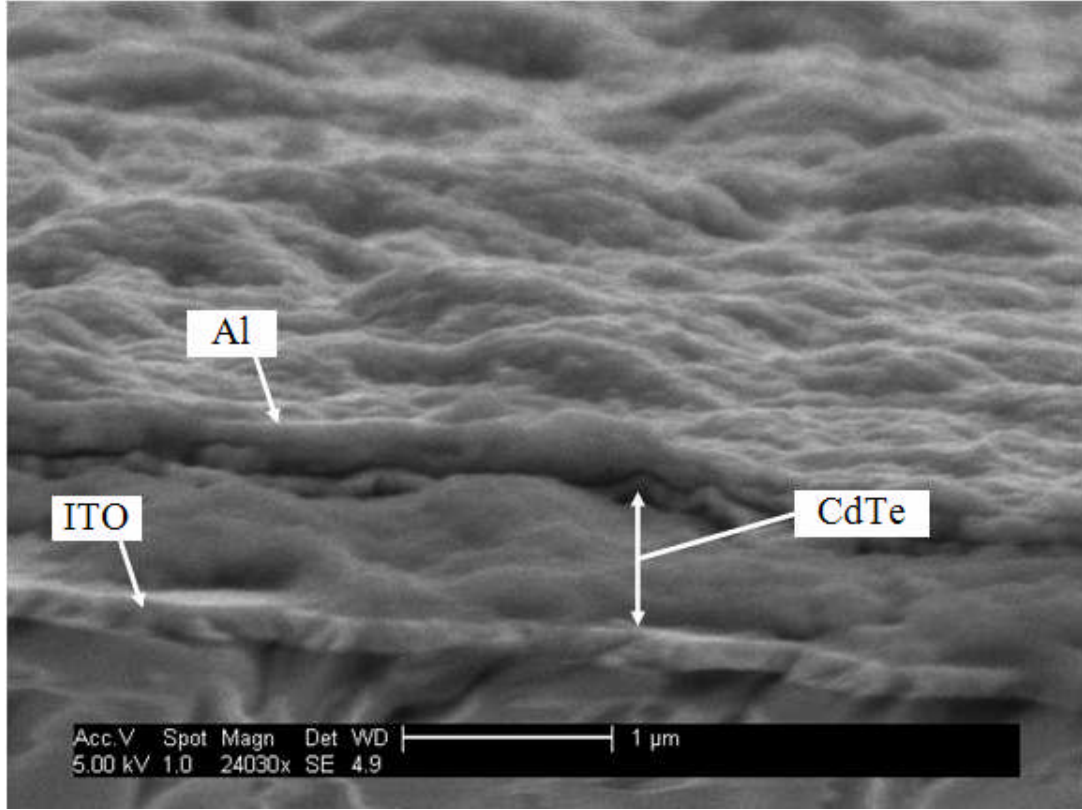
Figure 32. SEM analysis of glass/ITO/CdTe×10/Al device structure. The thickness of the nanoparticle multilayer is around 300nm (the sample is tilted and some dimensions look different). A high roughness is clearly seen.

The investigation of the multilayer surface arrangement through SEM and AFM analysis, revealed that the adsorbed CdTe/polymer material formed a nano-structured porous composite layer (see Figure 33 and Figure 34). In particular, clusters with a diameter of 17-20nm, were identified from both SEM and AFM measurements. The size of these aggregates compared with the quantum dot size (2~5nm), suggests nanoparticle agglomeration. This phenomenon could take place either *in situ* or in suspension due to interactions between the nanoparticles and the polyelectrolytes. It does not affect the nanocrystal photoluminescence but it produces high-roughness nanoparticle multilayers.
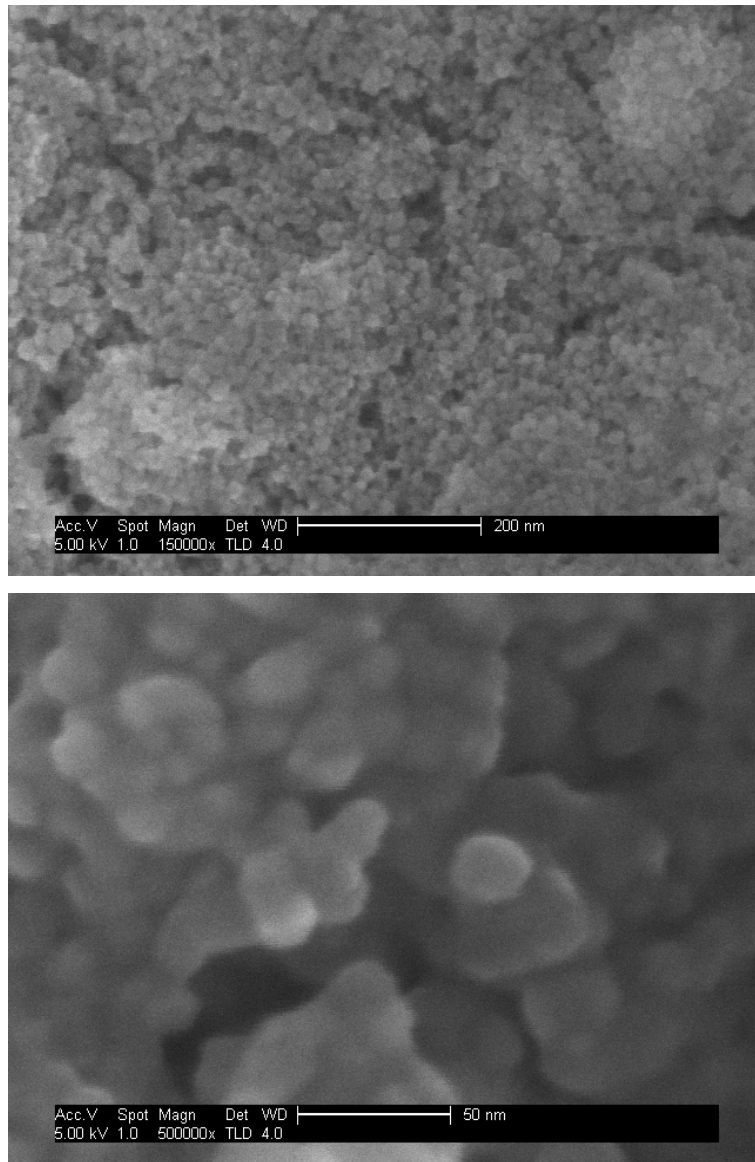
Figure 33. SFEG images of a manually-deposited CdTe multilayer structure. The spherical structures have a size around 20nm, compared to the nanoparticle size of 3nm. This means that the spheres are clusters of nanoparticles. This is due to agglomeration by the action of the polymer. A high porosity of the multilayer favours structure short-circuiting.

The cavernous appearance of the multilayer surface (Figure 33) favours the diffusion of the metal electrode during evaporation. This diffusion of metal towards the bottom electrode is responsible for the formation of short-circuiting metallic paths. Even in regions where there is no physical contact between cathode and anode, an enhanced electric field can be created by the diffusion of metallic filaments close to the anode surface. The high fields developed at these filaments are responsible for additional forming effects.

In summary, the results from microscopy analyses indicated that an improvement in multilayer homogeneity might have an impact in sample reliability and repeatability.
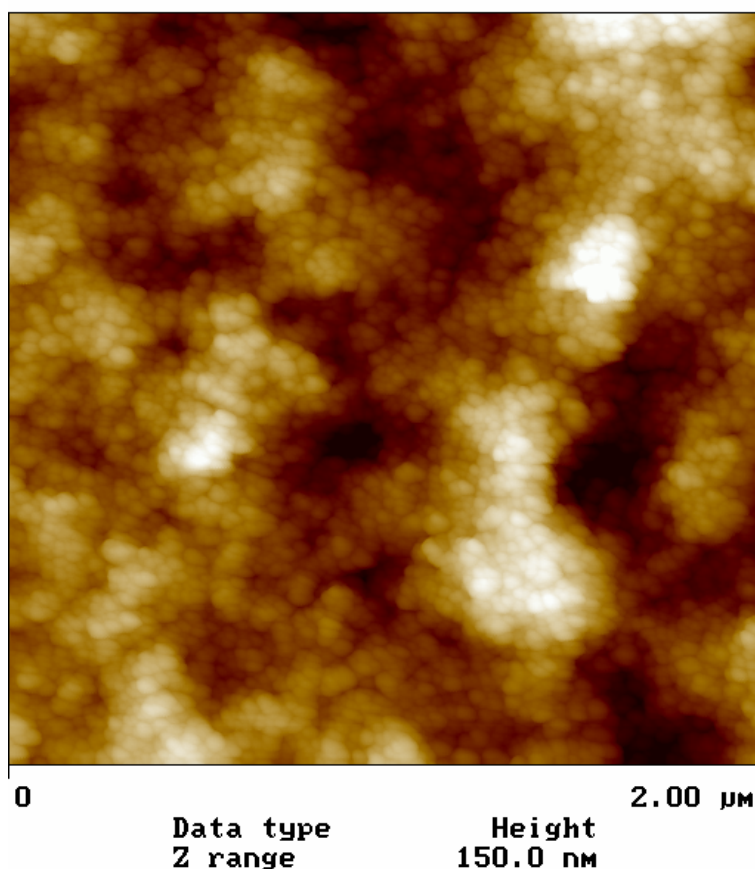
Figure 34. AFM images of a manually-deposited CdTe multilayer structure, confirming the results obtained with SEM.

4.1.2 Improvements in the manufacturing process

The main source of structural defects was thought to be the manual LbL procedure. Manufacturing the samples by hand meant the use of tweezers for sample transport and removal steps. This process could be generating unavoidable surface scratching, despite of great care used in the process, an inhomogeneous movement of the meniscus leading to inhomogeneous distribution of particles. Other factors include the variations in dipping, rinsing and immersion times that manual control introduces. Consequently a Zymate II robotic arm was programmed to perform LbL deposition of CdTe NCs from water solutions (Figure 36), as described in the experimental section.

It was also noticed that when samples were removed from any of the solutions, some small drops remained on the surfaces, probably due to surface tension. If these drops were drying on the surface, they would leave inhomogeneous deposits of polymer or nanoparticles. A vertical sample removal was introduced, with the idea of using gravity and water's surface tension to prevent drops remaining on the surface of the samples. A slow removal routine was specially programmed to allow for efficient drainage.

It has been reported[92] that PEI molecular chains form filaments that hang out off the surface; these filaments can surround a number of particles forming a protruding agglomerate that favours porosity. PDDA forms homogeneous layers without filament formation. Single-layer CdTe samples on glass were prepared by using either PEI or PDDA as binding polymer. Comparative absorption in the visible spectrum was made by using the PEI-sample spectrum as absorption reference (see Figure 35). Results did not reveal substantial changes in the concentration of nanocrystals for samples employing PDDA instead of PEI. Consequently, PEI was excluded from subsequent LbL processes.
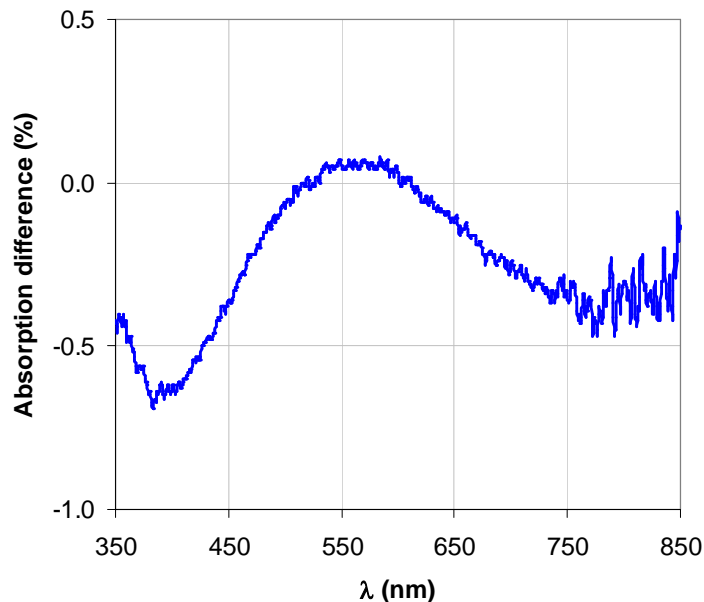
Figure 35. PDDA/CdTe absorption relative to PEI/CdTe absorption. The PEI-sample absorption spectrum is used as reference, then the PDDA-sample absorption is measured. The lower absorption for the PDDA-sample indicates poorer adhesion of CdTe. However, the deviations are below 1%.

A bath of continuously flowing distilled water was added to the apparatus. The samples were rinsed for several minutes after their immersion in each solution. This step helps eliminate excess polymer and loosely bounded nanoparticles, which are attached to the surface after dipping[147].
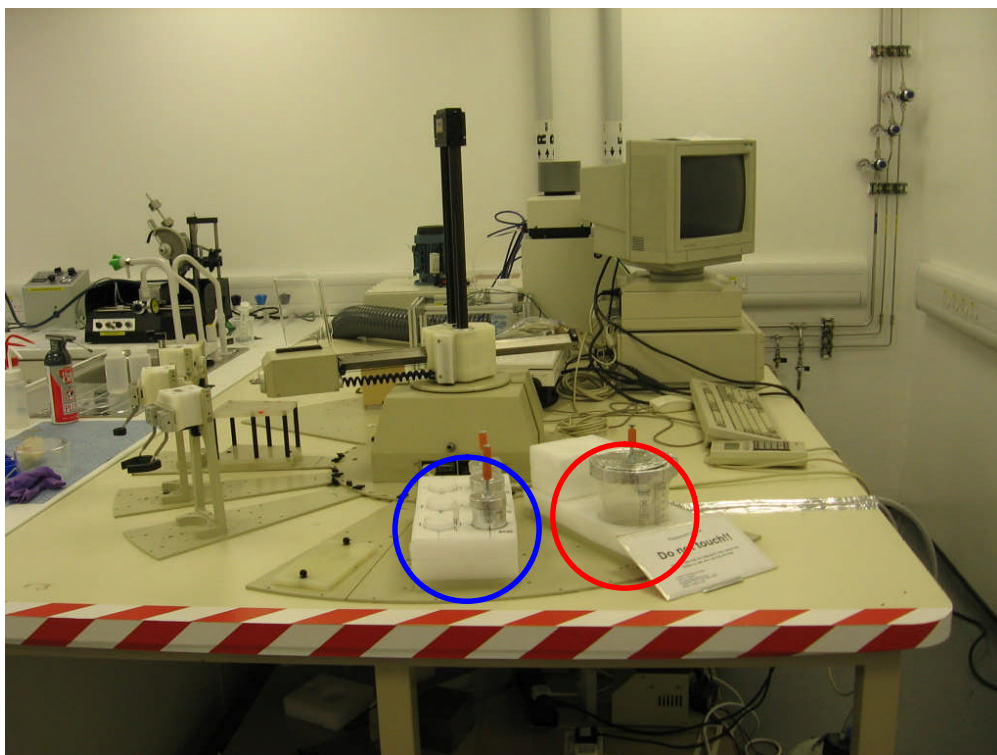
Figure 36. Robotic arm for automated layer-by-layer deposition of CdTe nanoparticles. The vessels for the different solutions are seen at the middle (blue). The continuous-flow washing bath can be seen towards the right (red).

All these modifications led to the results shown in Figure 37, showing an SEM image of 50 layers of CdTe on an ITO electrode (150nm thick). As can be seen the CdTe multilayer looks smooth and uniform over a long distance, while its total thickness is 150nm corresponding to a single layer thickness of ~3nm. Average roughness measurements with the profilometer were below 5nm.

Absorption spectra of light transmitted through the suspension of nanoparticles in water offered a value for the bandgap of 2.0eV (Figure 38 and Figure 39). Photoluminescence spectra from nanoparticle films deposited onto glass gave a band gap value of 1.98eV (Figure 38). The agreement between these two figures indicates that the nanoparticles preserve their properties after deposition. The value obtained for the band gap of the

nanoparticles compared to the bulk value (1.56eV), shows the effects of quantum confinement.
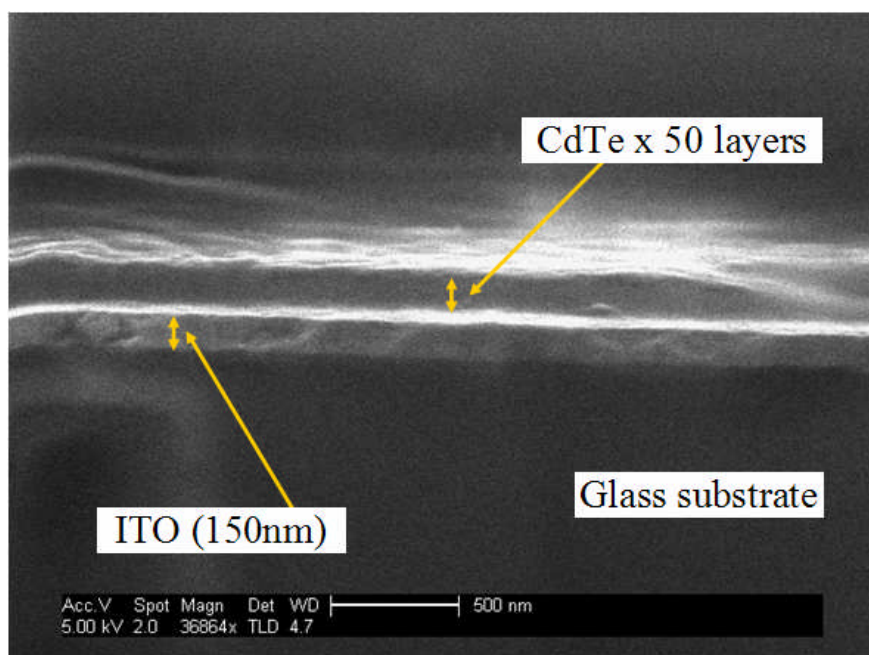
Figure 37. SEM cross-section picture of 50 layers of CdTe multilayer deposited by a robotic arm on top of an ITO sheet. The ITO and the multilayers thicknesses are 150nm each. A mean thickness of 3nm per layer was obtained from this image.
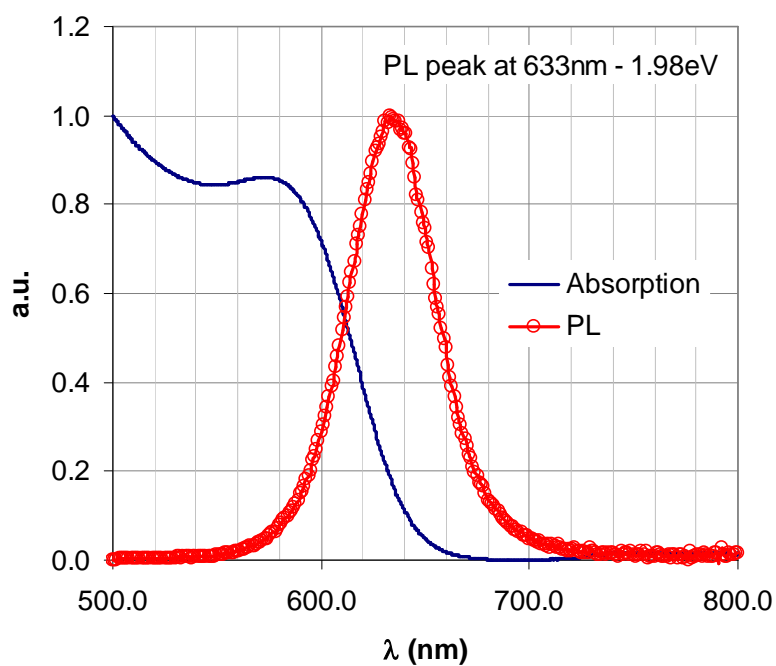
Figure 38. Absorption spectrum from nanoparticles in solution and photoluminescence spectrum from a multilayer. PL peak indicates a bandgap of 1.98eV.
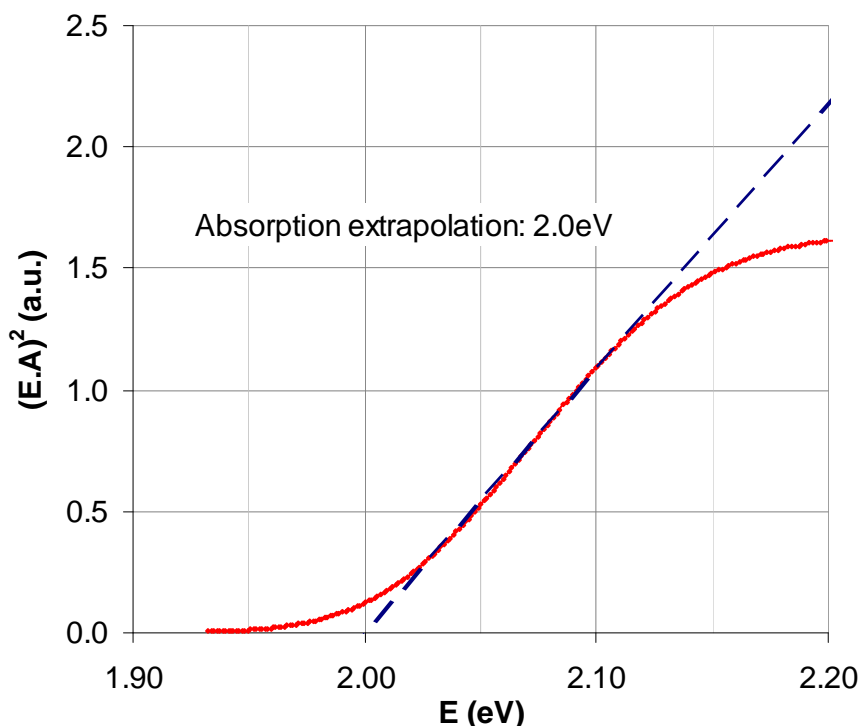
Figure 39. Analyses of the absorption spectrum of Figure 38 gives a 2.0eV value for the band gap, in good agreement with that obtained from PL.

TEM carbon-coated grids were covered with 5 layers of CdTe by the same automated LbL procedure used to produce devices. HRTEM pictures are shown in Figure 40. The pictures present low sharpness, due to the presence of polymer. However, it is possible to observe individual nanoparticles dispersed in a disordered arrangement. The typical particle size is around 3nm, and typical closer-neighbour distance is a fraction of the dimensions of a particle. Small-angle X-ray diffraction analysis of CdTe nanoparticle multi-layers confirmed that the typical nanocrystal size is around 2-3nm. X-ray reflectivity measurements were used to determine the packing density of particles. The results gave density figures of 2.3-2.6g/cm^3 for the emissive layer.

Using the density of CdTe (6.2g/cm^3) and of PDDA (1.04 g/cm^3), the filling factor for CdTe nanoparticles was calculated to be a 27%. A computer simulation was produced to generate a number of 3-D arrays of spherical particles filling a space up to 27% in volume. Particles were added to the volume at random, to form a disordered array in agreement with the HRTEM pictures for particles deposited by layer-by-layer (Figure 40 and Figure 41). A typical 3D-volume generated by the simulation is shown in Figure 42a. It seems reasonable to consider that the extrapolation of Figure 41 to three

dimensions would render a volumetric distribution similar to that on Figure 42. A plot of inter-particle distance distribution (Figure 43) shows that most of the nanoparticles are packed with mean inter-particle distances of around 10% of the particle radius. Hence, the inter-particle separation is in the order of 2–3Å. The HRTEM pictures of Figure 40 and Figure 41 support this result.
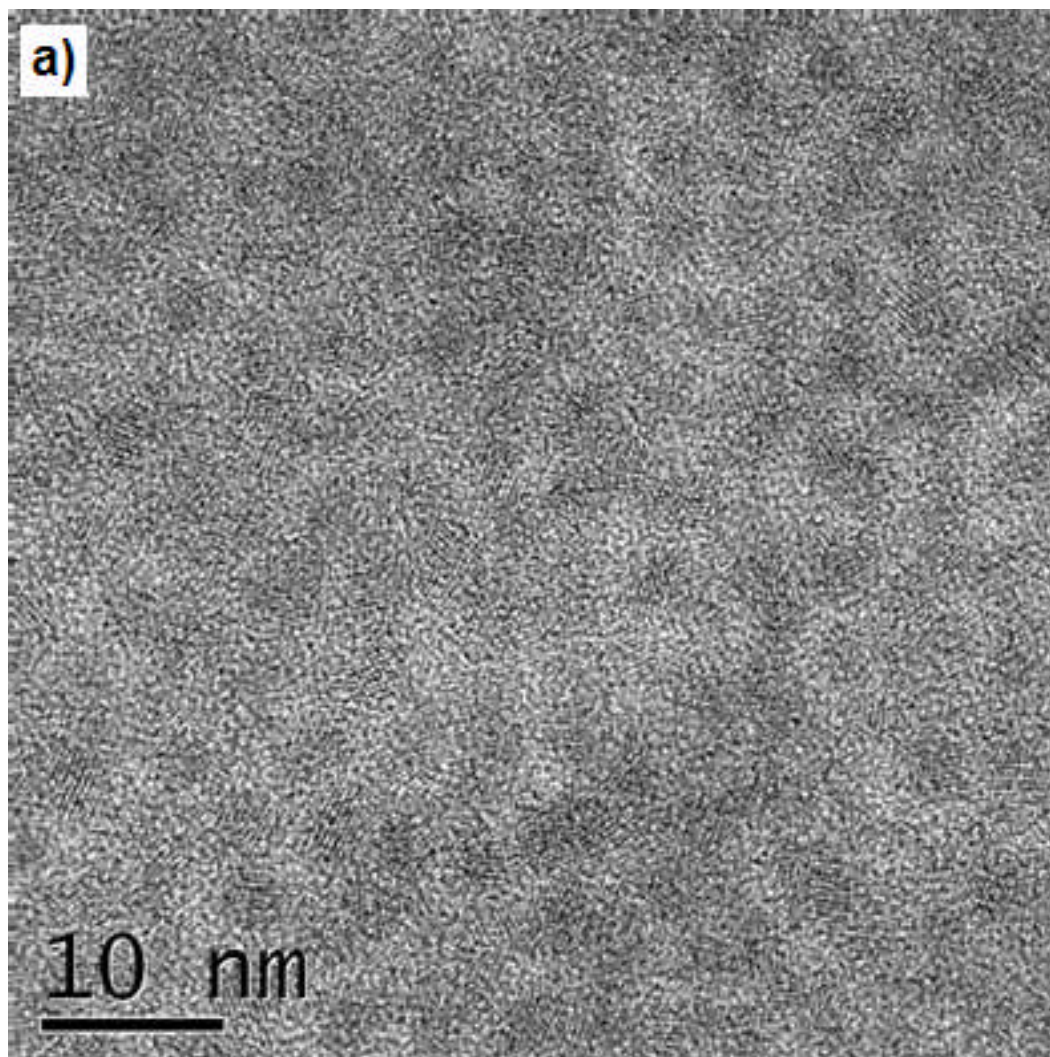
Figure 40. HRTEM picture of 5 layers of CdTe. The multilayer was deposited following the LbL procedure used to manufacture the device. The presence of polymer in the sample makes the imaging process particularly difficult, hence the relative low sharpness of the picture.
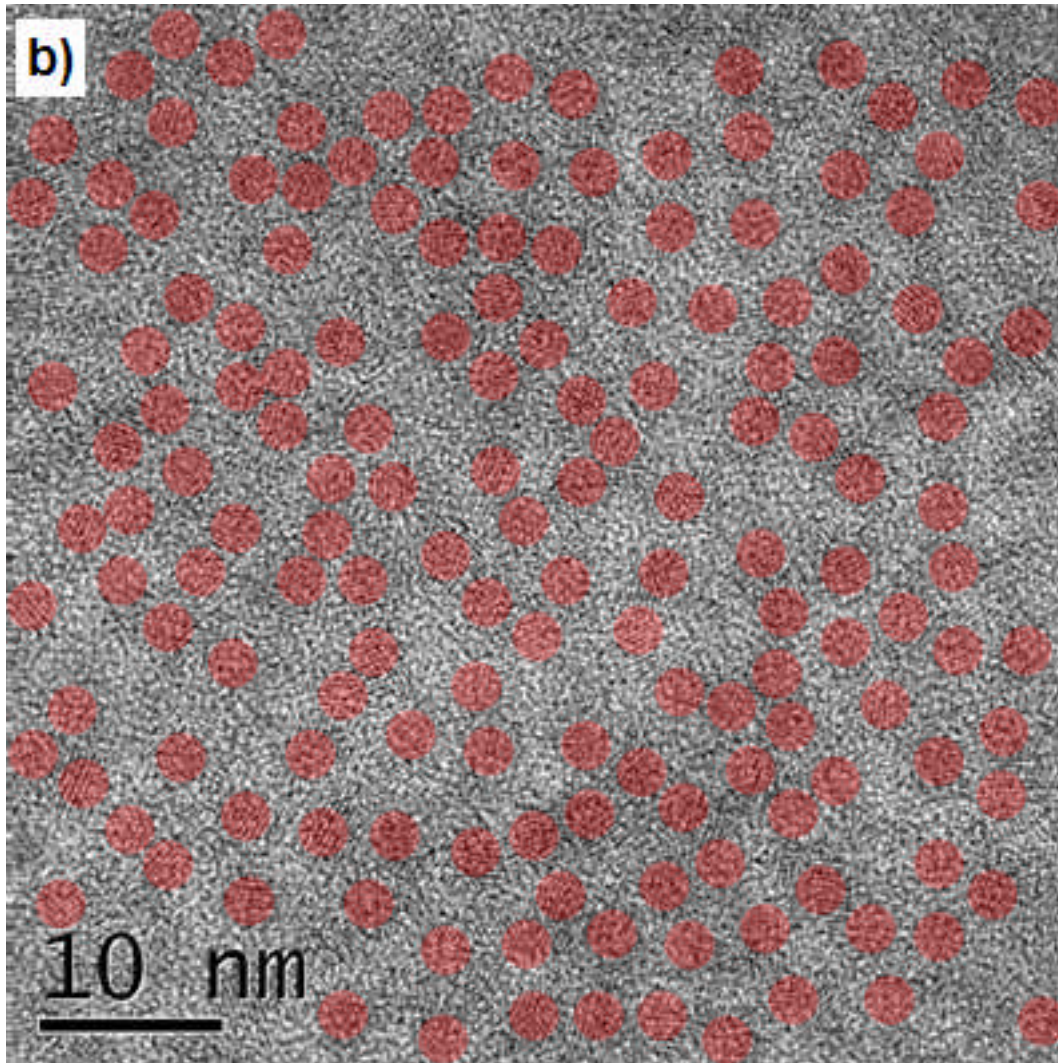
Figure 41. Same picture as shown in Figure 40, with the nanoparticles highlighted with red circles. It can be observed that the nanoparticles have a diameter around 3nm, and that the distances to closest neighbours is in general a fraction of the size of the nanoparticles. Extrapolation of this distribution of particles to three dimensions would result in a distribution like that shown in Figure 42.
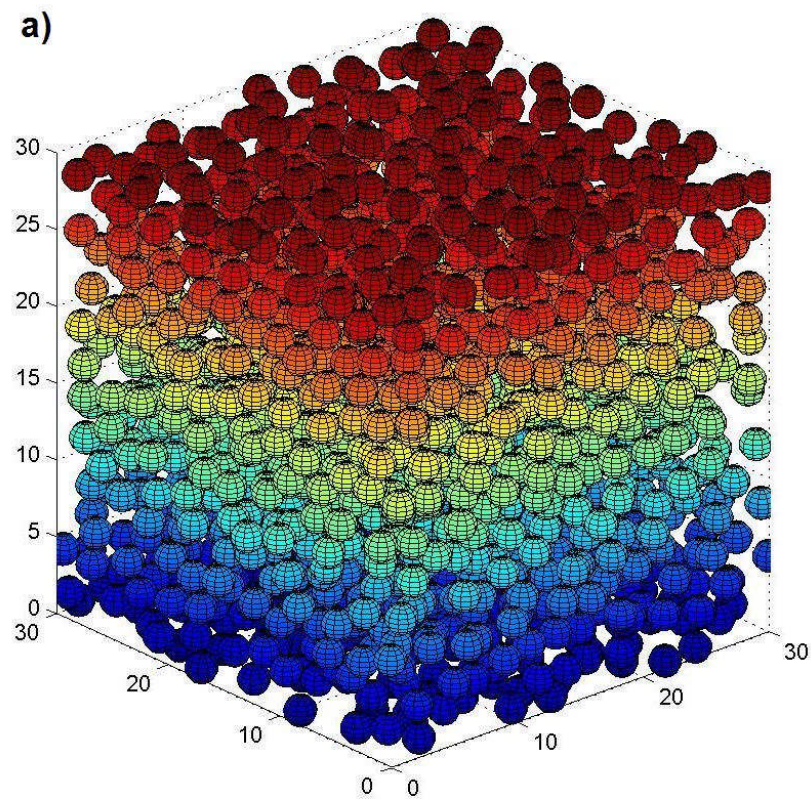
Figure 42. A computer generated array of particles with a 27% packing ratio. The axes are scaled in radius units. The different colours are added for clarity.
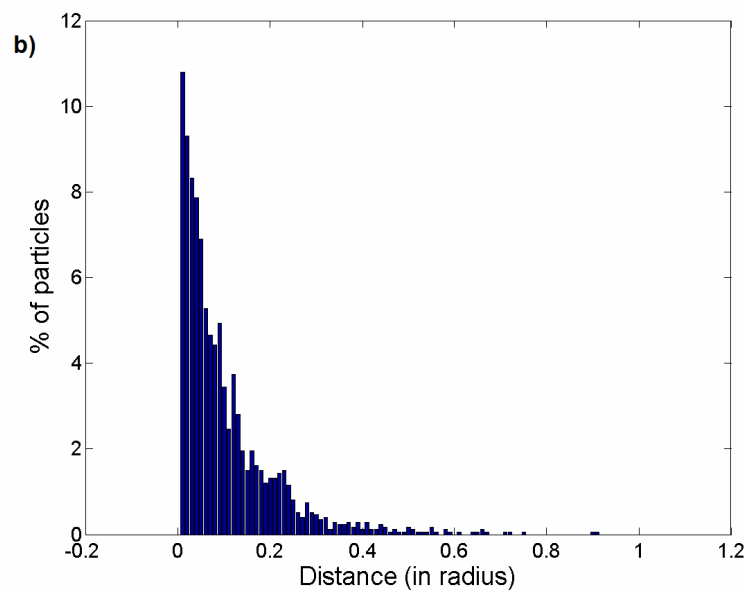
Figure 43. Typical inter-particle distance distribution corresponding to a 27% packing ratio. The distance is expressed in radius units. As can be seen, most of the particles find their closest

neighbours at a distance around 10% of its radius. The typical particle diameter is 3nm, meaning that the distance between closest neighbours is of the order of 2-3Å.

A process improvement has been described in this section, involving changes in the LbL process and the evaporation of metal cathodes. These improvements led from a situation in which light emission was an exception, to a situation in which light emission happened in nearly 90% of the devices. However, the improvements in the coherency of the electrical characteristics were not so encouraging. Approximately 95% of the samples still showed erratic behaviour, characterized by highly unstable current-voltage characteristics and early device breakdown.

The manufacturing process followed in this work was complex and far from industry standards, with the production of devices taking up to 5 days. The device performance was affected by many factors, these included: the manufacturing of the nanoparticles, storage of nanoparticles, the LbL procedure and electrode deposition, or during sample handling and testing. It was impossible at this stage to identify and correct the weak spots further than what has been discussed previously. The objective of the project was to investigate the dynamic effects on CdTe nanoparticle films; therefore once a process was in place to produce working devices no further development of the process was undertaken. The control of the factors highlighted above were out of the scope of this work and so the process was completed as stated.

However, the remaining 5% of the samples have allowed substantial analyses. Section 4.2 covers the results from the samples that showed stable and coherent electric behaviour. The remaining 95% of samples produced have been ignored for the data analysis as they were not suitable due to the low stability of either current or EL.

4.1.3 Metal cathodes and loss of photoluminescence

The stage next to the deposition of the nanocrystal multilayer is the deposition of the cathode. Metal cathodes of gold and aluminium were deposited by thermal evaporation at pressures below 4×10^{-6} mbar. Immediate inspection under UV light of the areas coated with metal revealed a loss of photoluminescence that was inhomogeneous across the device area (see Figure 44 and Figure 45). Some samples showed a total loss of photoluminescence under the electrode area; some others presented loss in patches;

some others presented no loss at all. The drop in photoluminescence was between a slight decrease and total loss. However, in samples with an aluminium cathode, around 70% of the areas recovered their photoluminescence after a time approximately 20 minutes in air. The remaining 30% of darkened areas remained damaged. It was also noticed that nanocrystal multilayers deposited on top of discontinuous films of platinum or gold produced substantially less photoluminescence than surrounding areas uncoated with metal.
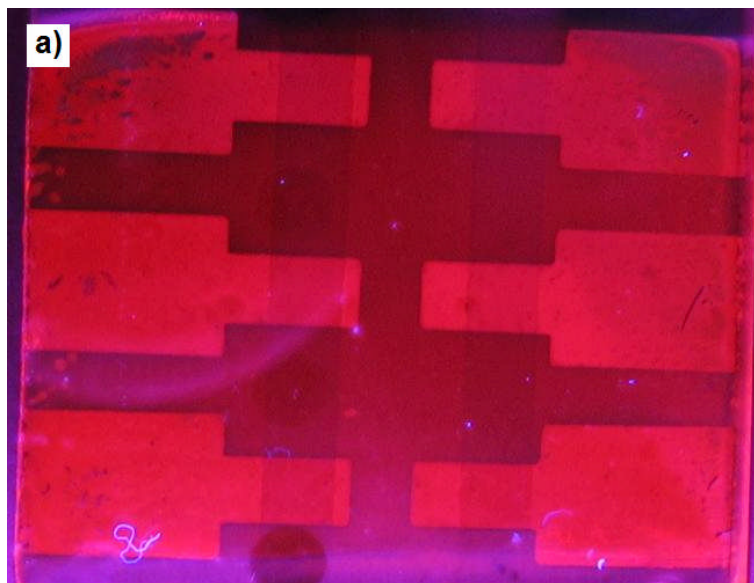
Figure 44. Visual inspection of photoluminescence from the glass side of samples under UV light, showing a sample with a good photoluminescence. The clear rectangular shapes are the aluminium electrodes. The ITO stripes are noticeable due to differences in optical transmittance. The emissive area is located in the square where both electrodes cross.

The quenching of photoluminescence near electrodes is commonly known[6,15,16]. It is related to Auger recombination processes near the metal electrode. The recovery of photoluminescence in samples with aluminium cathodes is indicative of a secondary process occurring. In this case it is likely that the oxidation of the metal at the interface with the nanocrystals prevents interaction with the metal. As both platinum and gold are inert to oxidation, the metal/nanoparticle contact remains, thus preserving the quenching effects. The consequences of the oxidation of the interfacial aluminium are of great importance to device performance and stability. This will be the object of investigation in Sections 4.2.3 and 4.2.5.
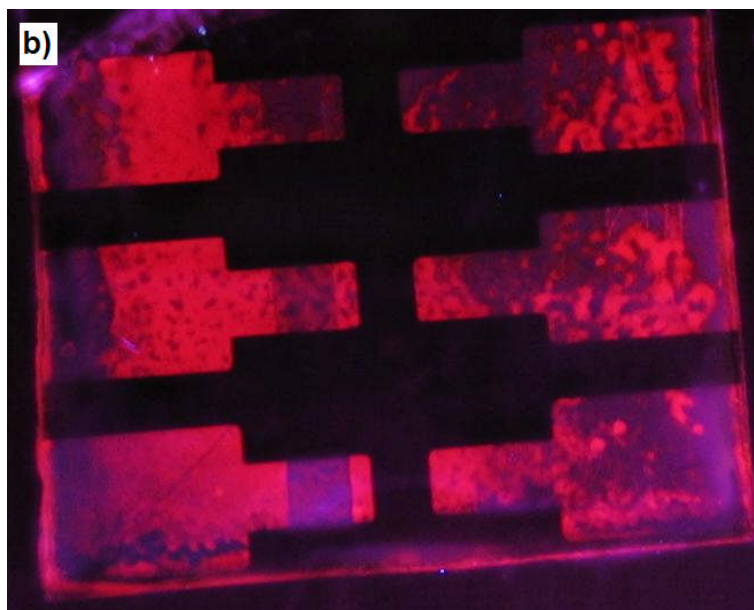
Figure 45. A sample right after being coated with aluminium electrodes. The photoluminescence is poor and the areas are full of dark patches. Some of these patches would recover their luminescence after being exposed to the air. Other patches might remain where permanent damage has been inflicted upon the nanoparticles during metal evaporation.

As highlighted above, some areas coated with aluminium did not recover their photoluminescence. The reason for this effect is related to the metal deposition procedure. During evaporation, the boat containing the metal source reaches high temperatures (the melting point for aluminium is over 930K and higher temperatures are required for evaporation); if the samples are too near the boat, thermal radiation damages the nanoparticle multilayer. Thus, the deposition distance was doubled in order to reduce heating of the device structure.

Metal sputtering was also tested for cathode deposition. However, every attempt resulted in a substantial loss of photoluminescence, independently of the metal and sputtering techniques DC or RF. This loss was attributed to an electric-field induced damage on the layers exposed to the plasma, due to the impact of high-energy charges. The effect has not been investigated further.

4.1.4 First electroluminescence results

In the previous sections, several modifications to the manufacturing process have been presented. The improvements that these modifications introduced will be shown here.

The modified automated LbL deposition was used to produce device structures. The deposition of aluminium cathodes at long distance from the boats effectively reduced, to a low percentage (5%), the number of devices spoiled at this stage.

Light emission was detected from a batch of samples made of 10 layers of CdTe. The number of emitting areas in a batch of devices was raised to near 90%. Although the emission was faint, it was possible to obtain pictures of emissive areas (4mm^2 and 8mm^2) with a digital camera (Figure 46).
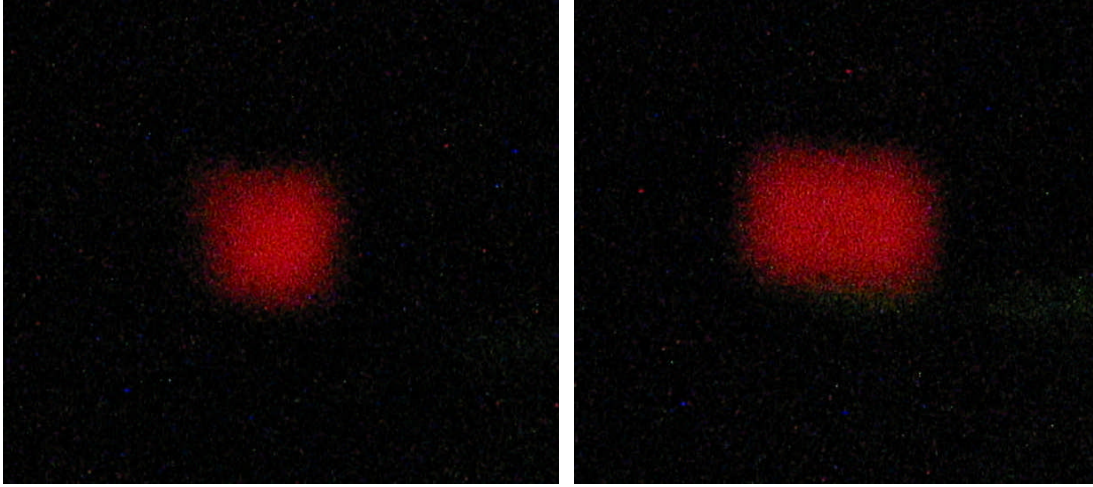
Figure 46. Light emission from 4mm^2 and 8mm^2 structures of 10 layers of CdTe. The emission was very faint and it required an exposure of 1 second to obtain the pictures, hence the blurred appearance.

For these devices, the turn on voltage was typically 3V, while the current density flowing into the device was around 1.0-5.0mA/cm^2. Typical normalized EL and PL spectra are shown in Figure 47. As can be seen, there was a steady growth of EL intensity with bias, until a maximum was achieved (6V in Figure 47). If the bias was increased further, EL intensity was not improved further (see 7V curve in Figure 47). In order to measure stability, a 6V bias was applied to an active area and kept constant while taking EL spectra every 5 minutes. The spectra showed persistent profiles and intensities for one hour as shown in Figure 47 (the experiment had to be terminated for non-technical reasons). This indicates that the operation mechanisms of the samples were stable during this period.
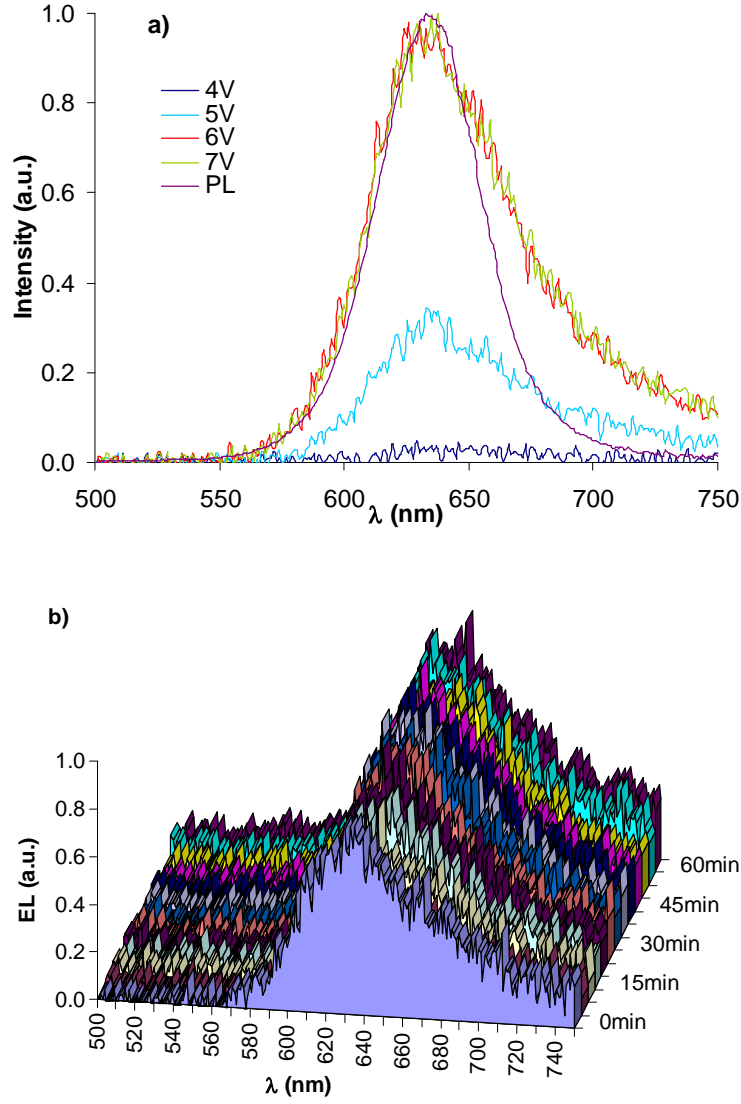
Figure 47. a) Photoluminescence spectrum and electroluminescence spectra at various biases. The peak emissions were obtained at 6 and 7 volts. b) Succession of electroluminescence spectra spaced 5 minutes apart covering 1 hour of operation. The persistence of their shape and intensity indicates emission stability through the period of analysis.

4.2 Device dynamics

In Section 4.1, the development of a process for the manufacture of samples with repeatable results was presented. The elimination of structural failures and the achievement of a high throughput for light emission allowed the study of the dynamics

of device operation. In Section 4.2 several topics concerning electric conduction and light emission mechanisms will be discussed.

First, the optimal number of layers for the device will be empirically established, in order to justify why 30-layer samples are thoroughly employed for the rest of the analyses. Section 4.2.2 will present the best results obtained for 30-layer samples, but also it will introduce a number of stability problems found due to the operation of the device (in contrast to the structural instabilities that had been already corrected). The following sections will show the results of the investigations on these problems, involving single-carrier devices and experiments in nitrogen atmosphere. The crucial role of cathode oxidation for charge injection and device stability and efficiency will be established. After that, in light of the results of previous sections, a model based on the Fowler-Nordheim effect will be used to explain the operation of the devices. Finally, different operational constraints in the applied field will be presented in relation to the concepts of multilayer critical field and dielectric breakdown.

4.2.1 Influence of the number of layers

In the structure investigated in this work, the thickness of the nanocrystal multilayer fixes the distance between electrodes. Thus, the internal electric fields during operation will depend on the number of nanoparticle layers deposited. Excessively high fields might cause electric breakdown of the structure. Fields too low will result in poor charge injection. Consequently, a first approach to the study of these devices was to experimentally find the number of layers that produces the best results in terms of stability and light output. For this purpose, samples with 20, 30, 40 and 50 layers were produced and tested by current-voltage (I-V) and electroluminescence-voltage (EL-V) measurements. Assuming a 3nm thickness per layer, a range of 60nm to 150nm in the thickness of the multilayer was covered.

The current-voltage characteristics obtained from a set of samples of 20 layers are shown in Figure 48, while those from 30, 40, and 50-layer samples are shown in Figure 49; for clarity purposes, the curves corresponding to samples with 20 layers have been plotted on a separate graph. The voltage sweeps were stopped at those points in which a surge of current was detected, or when the light emission started to drop.
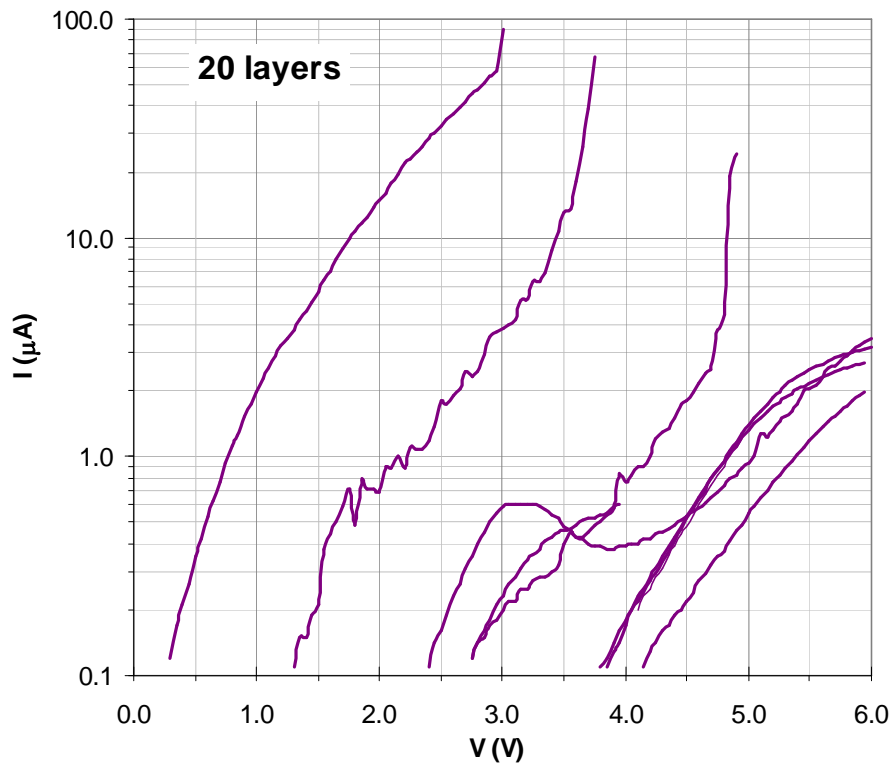
Figure 48. Current-voltage characteristics for 20-layer samples. The curves are very irregular in terms of conductivity, sometimes reaching several tens of microamperes. The shapes are also irregular, with samples showing noisy patterns and negative resistance areas

Samples with 20 layers presented a very irregular behaviour. Some devices were conductive at low voltages, presenting current densities up to $2.5mA/cm^2$ or greater at biases of 3-5V, with the consequent destruction of the sample. Other samples needed several volts to start conducting over the noise level; their currents were of $50\mu A/cm^2$ at voltages as around 6V, with little or no emission. Some samples presented irregularities like negative resistance regimes, with an associated irreversible drop in EL and PL (see Figure 50). These irregular behaviours were not related to the structural issues described in Section 4.1, due to the absence of ohmic characteristics and Joule heating. The large variations of behaviour revealed an excessive sensitivity to variations in the operational conditions. This is a characteristic of an unstable region of operation. A possible explanation for this instability of 20-layer samples will be offered in Section 4.2.8.
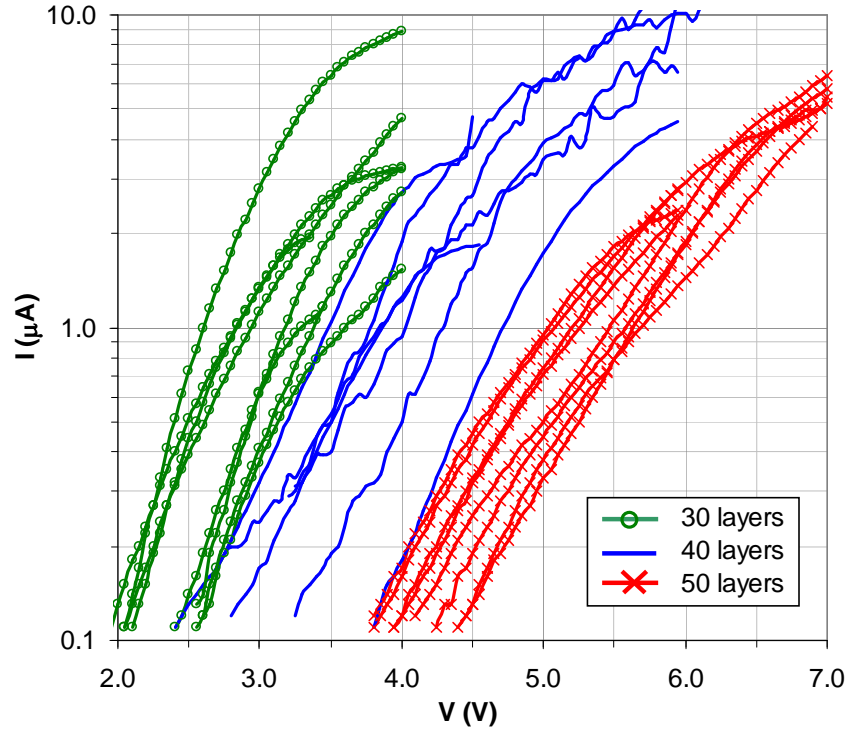
Figure 49. Current-voltage characteristics of 30, 40 and 50-layer samples. The curves are regular for the three sets, although 40-layer samples showed slightly noisier patterns. The lines span regularly from lower to higher voltages in accordance to the number of layers; this suggests a field dependency of current, as the number of layers determine the thickness of the emissive layer.

Samples with 30, 40 and 50 layers presented a more regular behaviour. With the exception of unavoidable faulty devices, all the samples grouped together in the same ranges of voltage and current, as seen in Figure 49. The curvature that can be noticed at the top of the curves is a feature common to all samples operated in air and will be discussed in detail in Section 4.2.3.

Figure 50. Irreversible loss of photoluminescence is promptly spotted after a voltage sweep by inspection under UV light. Photoluminescence loss reveals permanent damage to the nanocrystals.

It is readily noticeable that the curves in Figure 49 are distributed in voltage according to the number of layers. As the number of layers is associated with the thickness of the emissive multilayer, a field dependency seemed to be responsible for current flow.

Plots of current versus electric field are shown in Figure 51. The current onset field spans 2×10^7V/m to 3×10^7V/m, and depends only on the characteristics of each individual sample (the details of this process are thoroughly studied in Section 4.2.6). The curves were interrupted when symptoms of device rupture were found, such as a sudden current surge or irreversible loss of EL and PL. For most of the samples, these symptoms started at field values around 4.5×10^7V/m, irrespective of the number of layers. This field value, referred as *critical field*, marks the limit of the operational region. (Its origins will be discussed in Section 4.2.7).
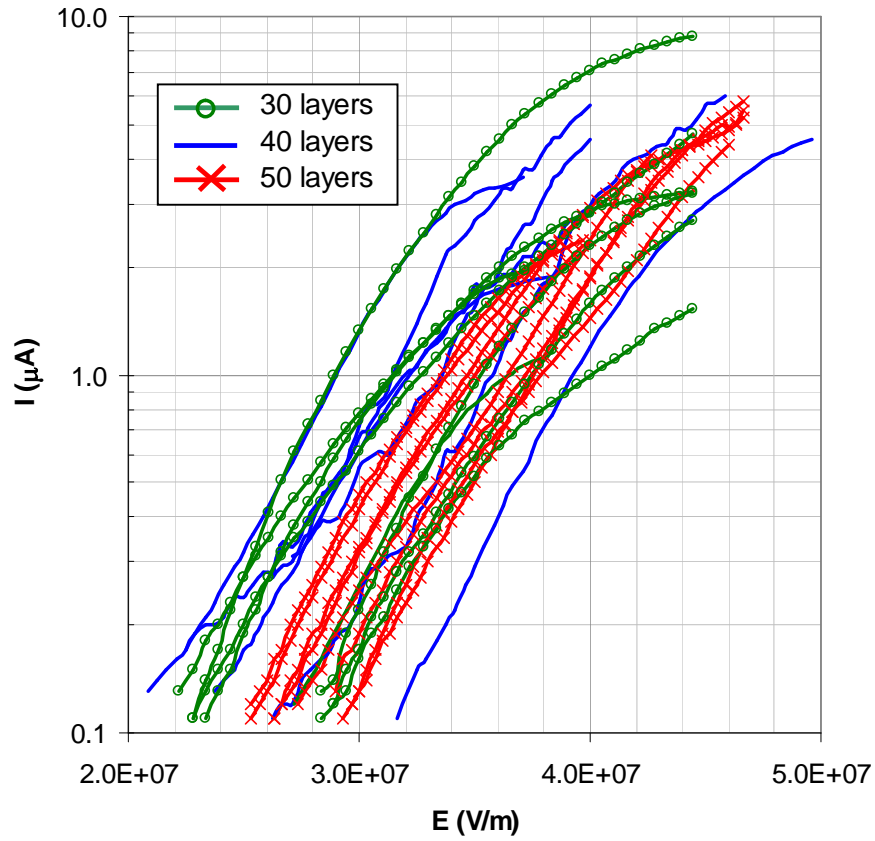
Figure 51. Current versus electric field for 30-layer (green), 40-layer (blue) and 50-layer (red) samples. In contrast with Figure 49, the curves corresponding to different number of layers are mixed within a narrow range of field values, confirming a field dependency of the current. A remarkable fact is that samples started to degrade a fields close to 4.0-4.5$\times 10^7$ V/m, where the sweep was interrupted to prevent failure.

Electroluminescence generally followed the current, as shown in Figure 52. In general, more current means more carriers available for radiative recombination. However, a certain proportion of carriers might cross the entire structure without recombination, in what is known as leakage current. Hence, the carriers responsible for the leakage current do not contribute to the emission of light.
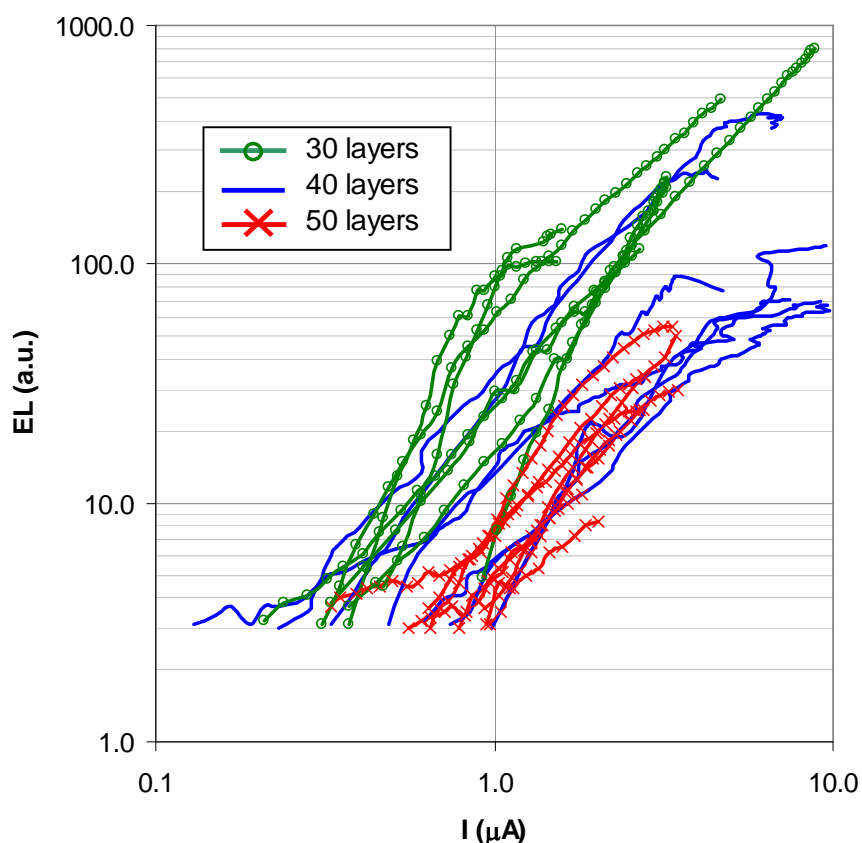
Figure 52. Electroluminescence intensity versus current for 30-layer (green), 40-layer (blue) and 50-layer (red) samples. It can be seen that the intensity is roughly proportional to the squared current. This was expected, as the number of photons emitted is proportional to the abundance of electrons and holes flowing through the device. However, the noisy shape of some electroluminescence curves indicates that some current could be lost into non-radiative effects.

Figure 53 illustrates the differences in device performance as a function of the number of layers. It can be seen that the best performances are obtained for 30 and 40 layer samples, whereas 50 layer samples are 10-15 times fainter. Samples with 30 layers outperform 40 layers samples, as their brightness was almost double and their operating bias was 1-2 volts lower, improving both quantum and power efficiencies. Consequently, 30-layer samples were considered optimal and adopted as the standard for all subsequent studies.
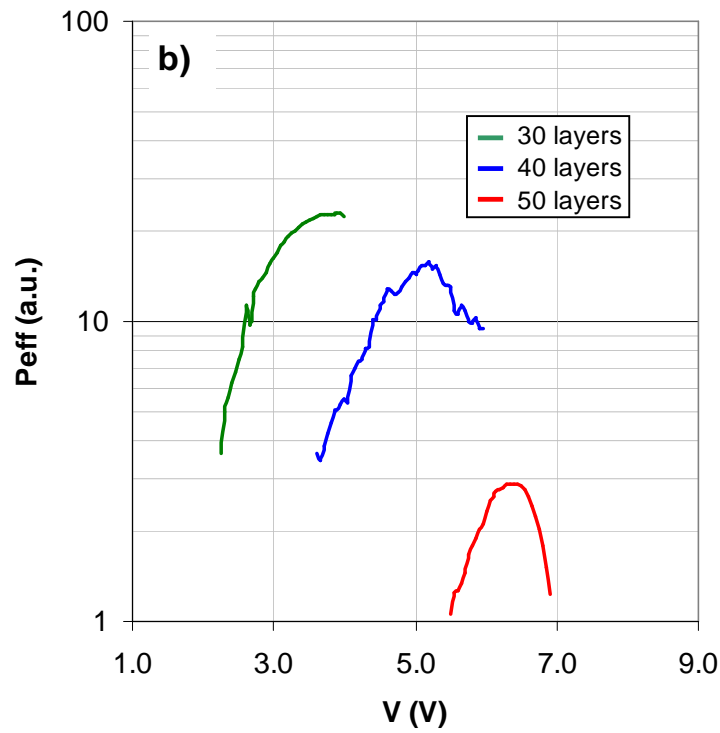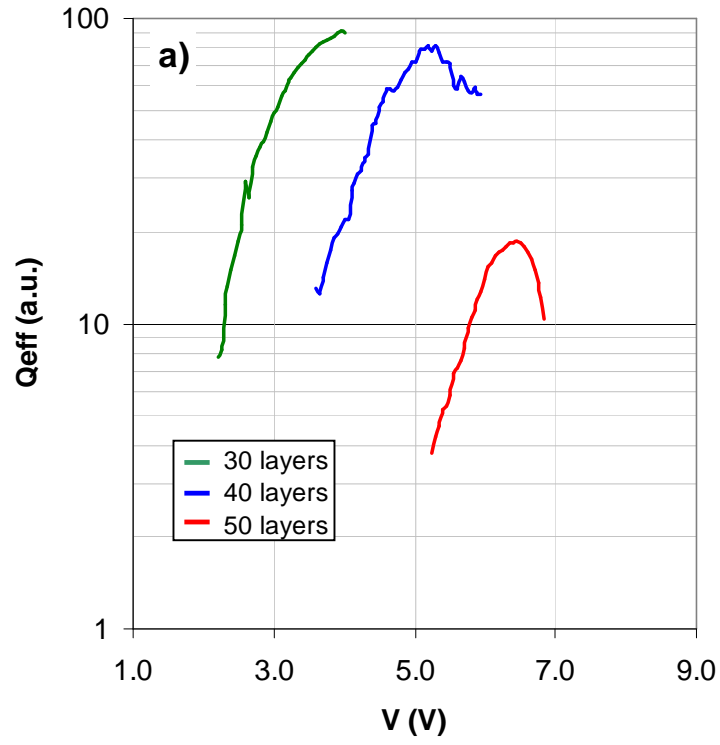
Figure 53. (a) Relative external quantum efficiency and (b) relative power efficiency versus voltage for best devices with 30, 40 and 50 layers. In general, 30-layer devices outperform those with 40 and 50 layers. In addition, current profiles and light emission are more stable for 30-layer devices.

4.2.2 Optimal performance of 30 layer devices

It has been shown in Section 4.2.1 that 30-layer samples offer better stability and efficiency. Several batches of 30-layer samples were produced and tested to find the operational conditions for optimal performance, defined in terms of external quantum efficiency, power efficiency and average device lifetime.

Figure 54 shows an NLED operating on a laboratory bench (air atmosphere, standard humidity) emitting a clear red light. The peak of emission was at 630nm ($E_{photon} \approx 1.97$eV) (Figure 55). Analysis of the current-voltage plots, shown in Figure 56, indicated a turn-on voltage of approximately 2.5V with an associated current density of 115μA/cm^2. Under optimal working conditions, a lighting power of W_L=141nW was measured at current densities of 350μA/cm^2 ($I \approx 14.05$μA) and 3.3V. If the emission is considered monochromatic (630nm), the external quantum efficiency can be calculated through:

$$Ext.\,Q_{eff} = \frac{\#\,photons}{\#\,electrons} = \frac{W_L\,(\mathrm{nW})}{E_{photon}\,(\mathrm{eV}) \cdot I\,(\mathrm{\mu A})}$$

This gives an external quantum efficiency of 0.51% (see Figure 57). The human eye has a photopic response of approximately 0.35 for light of 630nm; thus, the maximum power emitted corresponded to 0.8lm/W and 0.4cd/A, with a brightness peak of 1.42cd/m^2. The viewing angle is limited only by the total reflection of light at the air/glass interface.

The red tail observable in the EL spectrum is thought to be related to surface states and defects (Figure 55). Surface states and defects involve excitons of lower energy[30,87]. EL involves a higher surface contribution than PL, because carriers are injected through the nanocrystal surface. This increases the contribution of excitons associated to surface states and defects, generating the red tail[87].
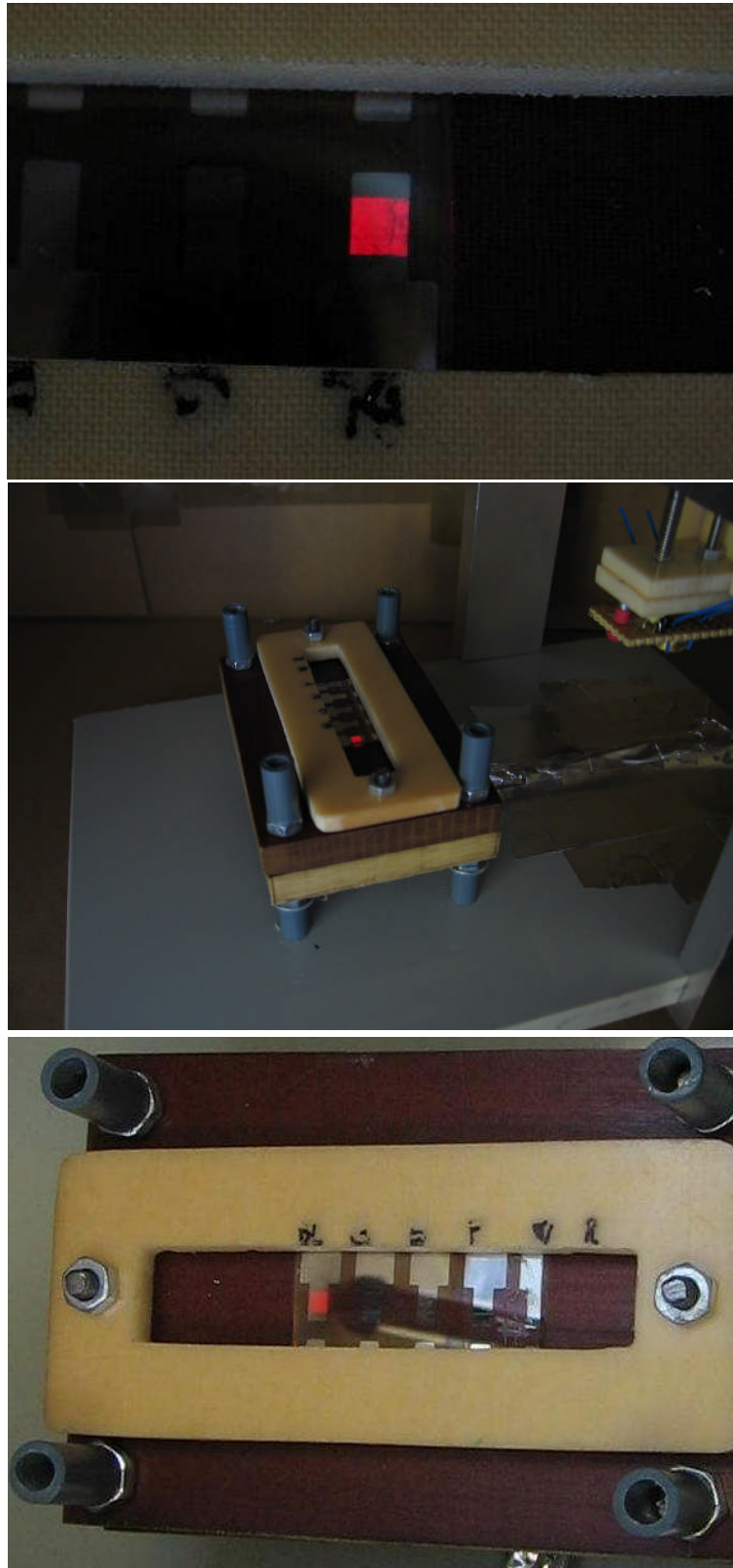
Figure 54. Electroluminescence from a 30-layer device biased at 3.3V. The device is shown at the measurements rig, although the photodiode used to collect the light has been removed to allow observation. The photoluminescence and electroluminescence spectra are also shown; the red tail on electroluminescence is thought to be caused by surface states and defects.
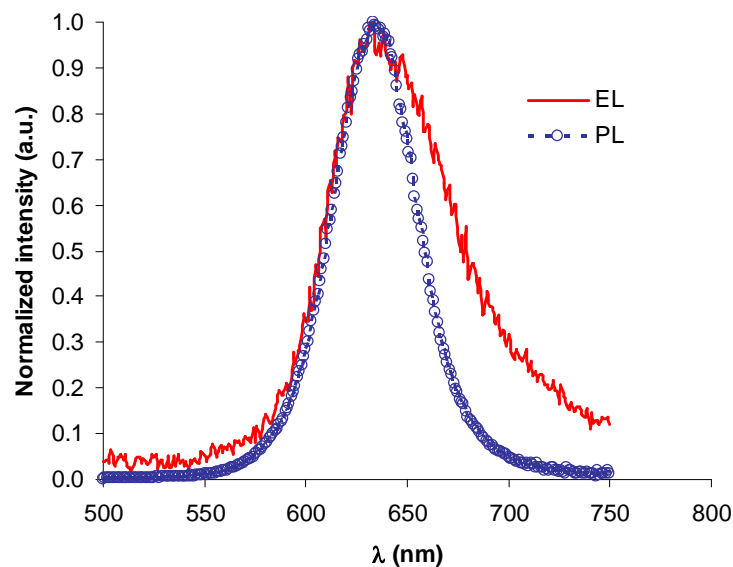
Figure 55. Electroluminescence from a 30-layer device biased at 3.3V. The photoluminescence of the same device is also shown; the red tail on electroluminescence is thought to be caused by surface states and defects.
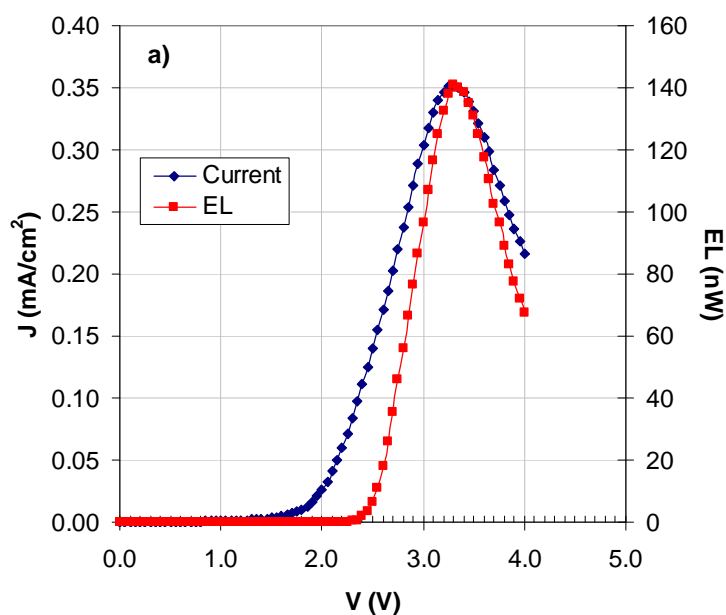
Figure 56. Typical current-voltage characteristic for an optimal 30-layer device, together with the associated electroluminescence intensity. A sudden drop in current and electroluminescence marks the beginning of device degradation.

An external quantum efficiency of 0.51% in electroluminescence is equivalent, in a first approximation, to an internal quantum efficiency of 8.3%, due to the refractive index of CdTe (n=2.85). The nanoparticles used for these samples had a photoluminescence

efficiency around 30-40%[*]. This means that the devices rendered into electroluminescence around 20-25% of the luminous capability of these particles. Brighter samples with the same levels of efficiency would be desirable, and future work should address this aim.
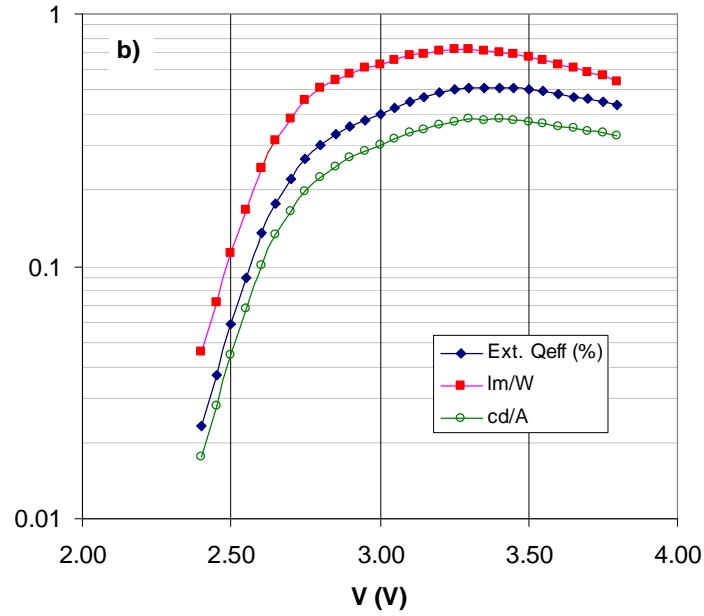
Figure 57. Several figures of merit for the device of Figure 56. Scale units are indicated in the legend.

When considering the figures of merit reported in this section, it is important to remember that this device is not optimized. This structure fits into a preliminary stage where materials characterization is the goal, somewhat similar to the works of Burroughes et al. in OLEDs[98]. As mentioned in the literature review, substantial improvements have been obtained in hybrid structures, and it is believed that similar improvements can be expected from more elaborate NLEDs.

4.2.3 Current degradation

The current-voltage curve in Figure 56a corresponds to a voltage sweep on a *fresh* (not previously biased) sample. Figure 58a shows three consecutive voltage sweeps from a sample of the same type. The maximum current level for the first sweep was

---

[*] This number was provided by Dr Nikolai Gaponik, of the Technical University of Dresden, Germany.

0.37 mA/cm^2 (15.0μA). This maximum decreased to 0.22 mA/cm^2 (8.7μA) for the second sweep and 0.07 mA/cm^2 (2.7μA) for the third, i.e. around 70% loss between consecutive sweeps. EL intensities also decreased with the ordinal of the sweep (Figure 58b). PL loss revealing nanocrystal degradation was not detected. Consequently, the drop in EL is due to the lower number of carriers available for recombination. For the first sweep, the current onset is around 2.0V, while the EL turn-on is near 2.3V. Both values shift to higher voltages in the following sweeps.

According to the band diagram in Figure 59, the barrier for hole injection is some three times higher than for electron injection. Thus, electron injection should happen at a bias substantially lower than hole injection. However, the onset of current and the EL turn-on are only 0.3V apart (Figure 58). Since both holes and electrons are needed for EL, it seems that electron and hole injection are separated by around 0.5V at most. Thus, the band diagram of Figure 59 is inconsistent with these results. Additional data is necessary to clarify this inconsistency, and they will be examined in this section.

The drop in current and emission observed in these devices is a dynamical rather than structural effect. There are no spikes of current or loss of photoluminescence that might signal a structural defect. The degradation originates from mechanisms occurring during device operation. Charge injection, charge transport or carrier recombination must be causing changes in the way the device behaves. Determining which mechanism or combination of mechanisms is responsible for the degradation of the device is a complex problem.

A convenient way of reducing the complexity is to analyse the dynamics of each type of carrier separately. It is possible to favour the injection of one type of carrier against the other into the device by choosing the material of the electrodes[100]. This is shown in the band diagrams of Figure 60. If both electrodes are made with a low work function material, e.g. aluminium, a current dominated by electrons will be obtained, whereas holes will be scarce due to high barriers at both electrodes; the device is commonly referred to as an electron-only device (ED). Alternatively, if both electrodes have a high work function, e.g. ITO or gold, holes will dominate in current, whereas there will be few electrons; the device is referred to as a hole-only device (HD). A device intended to have both types of carrier, like the ones already presented in this work, will be referred as a standard device (SD).
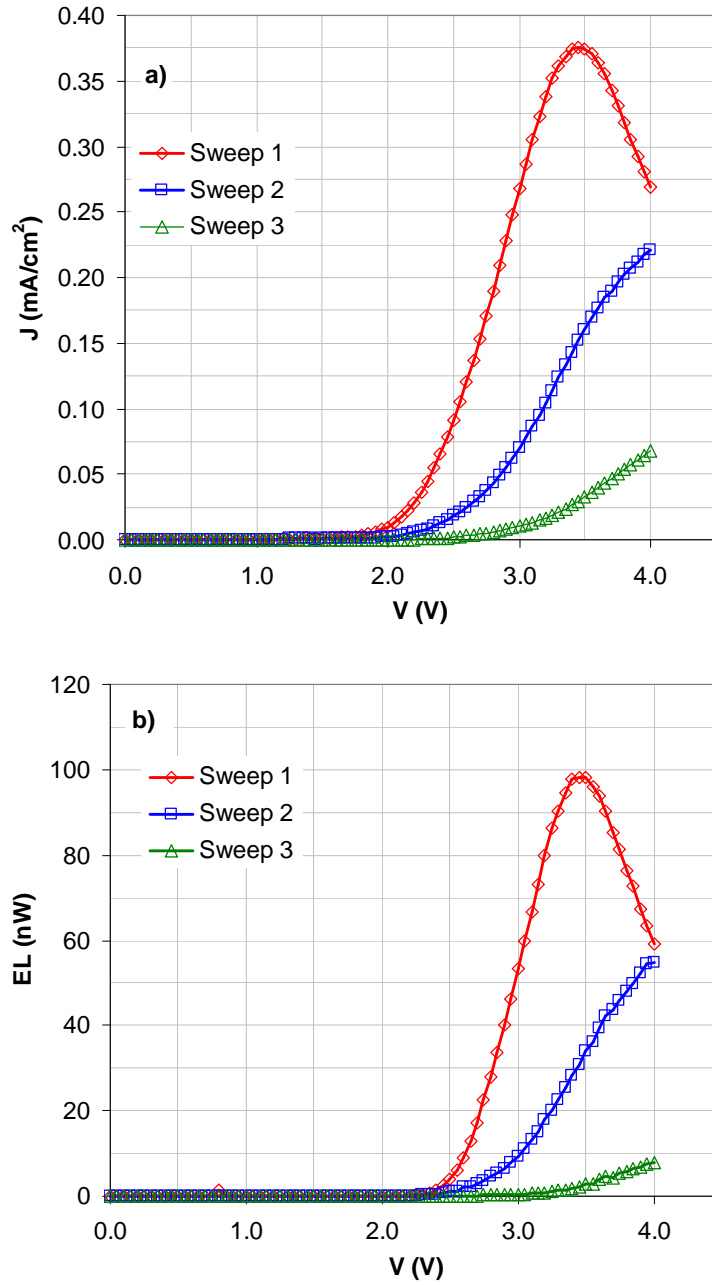
Figure 58. Current (a) and electroluminescence (b) for successive voltage sweeps for a 30-layer device operated in air. The current drops substantially with the ordinal of the sweep, and so does the associated light emission. The current onset is around 2.0V for the first sweep, while the EL turn-on is near 2.5V. These quantities shift towards higher voltages for successive sweeps.
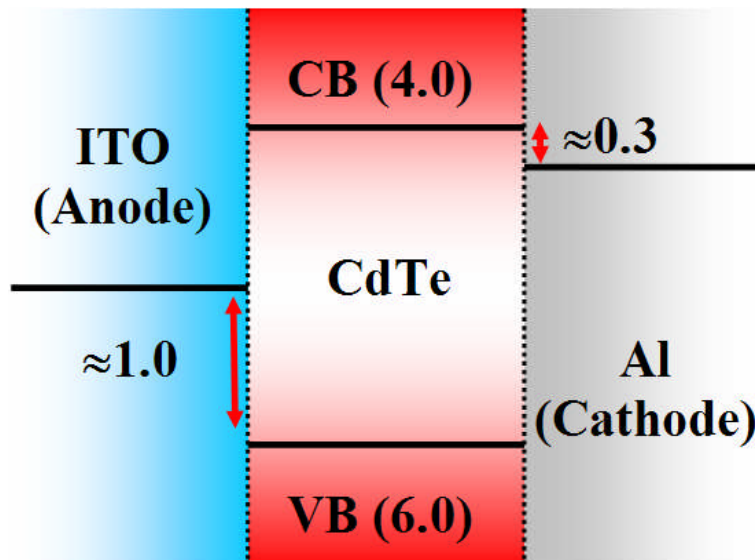
Figure 59. The band diagram of the device, with the barrier values for carrier injection (in eV). The barrier for electron injection is only of 0.3 eV, therefore currents higher than those of Figure 58 were expected.
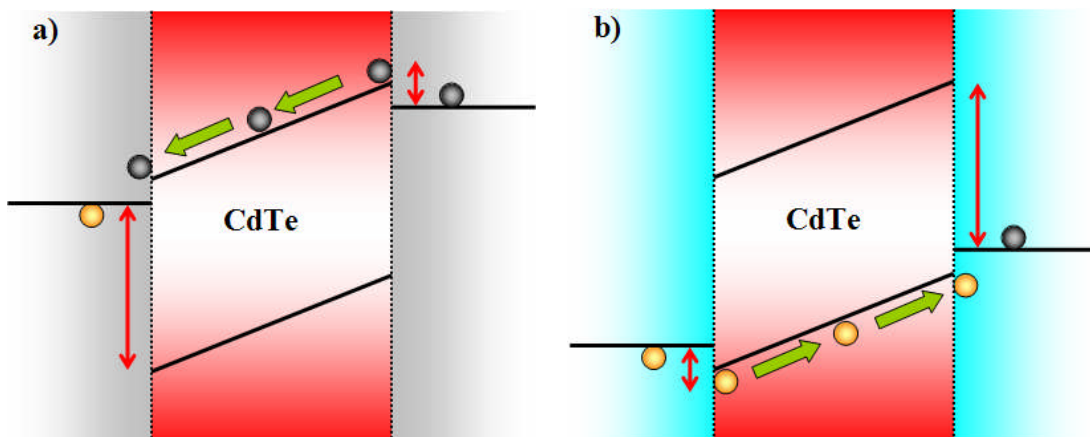
Figure 60. a) An electron-only device (ED). Both electrodes have a low work function; in consequence, electrons can easily penetrate the barrier, whereas holes are blocked. b) A hole-only device (HD). Both electrodes have high work functions, blocking the electrons while allowing the flow of holes. Single carrier devices help to study the behaviour of each type of carrier independently.

Hitherto, all devices have been operated in air. There is a possibility that device dynamics are influence by the presence of an oxygen-containing atmosphere. To test this possibility, the devices can be tested in an inert atmosphere, e.g. in nitrogen.

The next subsections will present the tests carried out with single-carrier devices and in nitrogen. First, the results of each of these experiments will be presented. Then, the

analyses of the combined results will follow. The data reveal that the oxidation of aluminium cathodes is causing the degradation of standard devices (SDs) measured in air.

4.2.3.1 Electron-only devices (EDs)

EDs were fabricated sandwiching 30 layers of CdTe nanocrystals between two aluminium electrodes. Figure 61 shows the band diagram of an ED, and Figure 62 shows typical I-V curves obtained in air from the device.
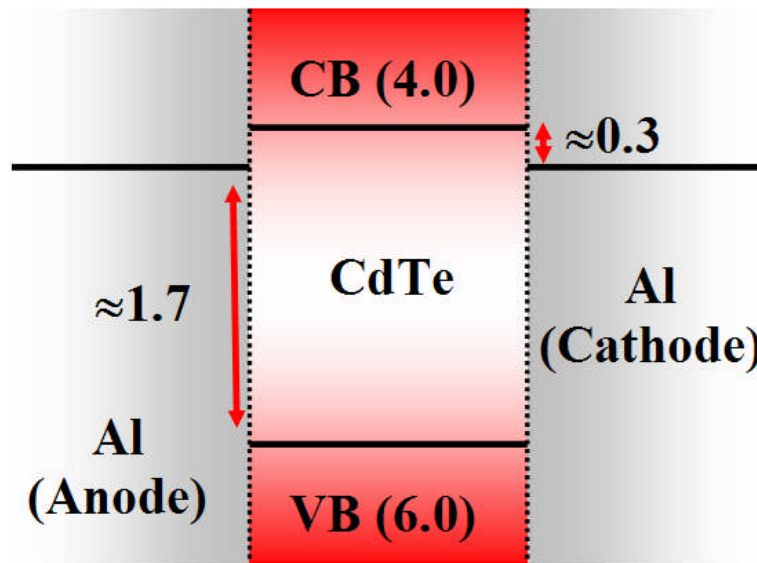
Figure 61. Band diagram of an ED (values are in eV). According to the low barrier for electron injection, more current was expected, compared with currents obtained in SDs (Figure 58).

The first sweep on the ED exhibited a steep current onset around 1.0V that was sustained until a shoulder developed at around 1.5V. The maximum current was 55.3 $\mu A/cm^2$ (2.2μA). A loss of 90% in current was obtained between consecutive sweeps. At the same time current onset points shifted to higher biases. Sweeps one and two in Figure 62 were interrupted when signs of degradation were detected. Sweep three was stopped at 3.0V to prevent irreversible damage to the sample. The decay of current in EDs was 20% greater than that found for SDs. Current levels in EDs (2.2μA max.) were near one order of magnitude lower than in SDs (15.0μA max.). Also, the current onset values are lower in EDs (1.0V) than in SDs (2.0V), despite of sharing the same

barrier height for electron injection. As in EDs both electrodes are made of aluminium (around 200nm thick each), EL from these samples could not be measured.
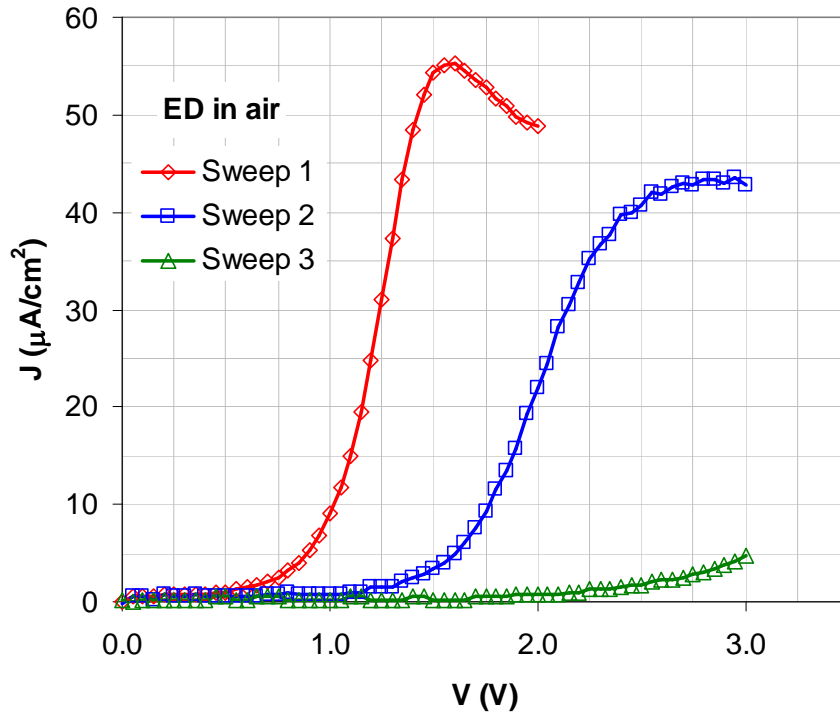
Figure 62. Current-voltage curves for an electron-only device (ED). The current decreases with the ordinal of the sweep. For the first sweep, the current onset is slightly below 1.0V, and it grows up to a maximum value around 55.3 μA/cm^2 (2.2μA). The maximum current decreases around 90% in consecutive sweeps, while the onset point shifts towards higher voltages. No electroluminescence can be measured, as both electrodes are opaque.

4.2.3.2 Hole-only devices (HDs)

HDs were fabricated sandwiching 30 layers of CdTe between ITO (anode) and gold (cathode) electrodes. Figure 63 shows typical current-voltage and electroluminescence-voltage curves for a HD, and Figure 64 shows the band diagram of the device. The current showed three distinguishable sections. There was no current until point A ($\approx$2.0V), where the current started flowing in a first conduction regime. At point B ($\approx$4.0V) there was an inflexion point towards a higher conductivity regime.
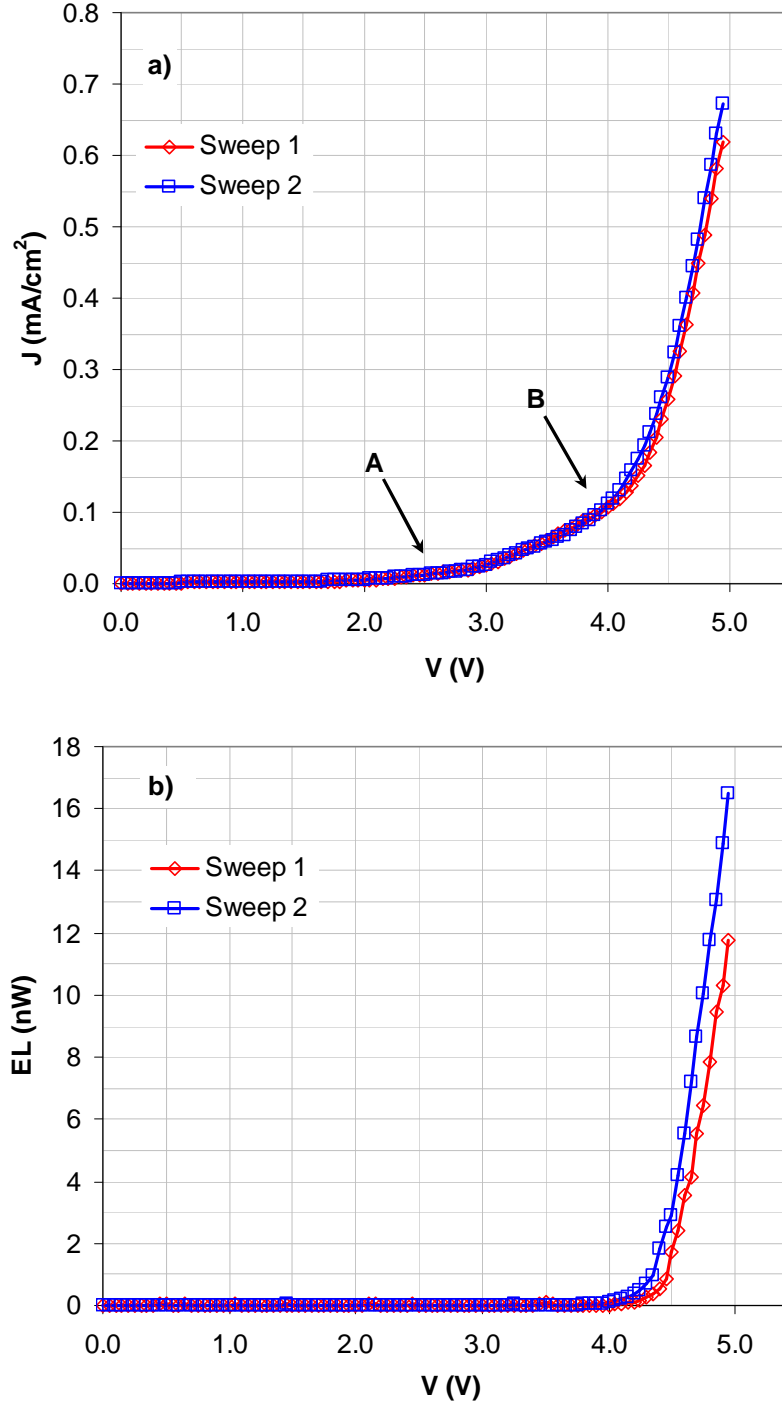
Figure 63. Current (a) and electroluminescence (b) curves for a hole-only device (ED). The current onset happens around 2.5V (point A). A second current regime starts near 4.0V (point B). The EL turn-on voltage is around 4.3V. This means that both electrons and holes are present since point B. The segment A-B is attributed to hole current, whereas electron injection starts at point B. This is consistent with the band diagram of the device. The degradation of current found in EDs and SDs does not happen in HDs, which show stable current end EL profiles for consecutive sweeps.

The electroluminescence turn-on happened slightly after point B (at $\approx$4.2V). This indicates that point A marks the injection of one type of carrier, whereas the second type is not injected until point B. The higher barrier in HDs corresponds to electrons, as shown in the band diagram. Fresh SDs also had EL turn-on points near 2.3V (Figure 58), which means that holes are already being injected from ITO at this bias. Thus, points A and B mark the thresholds for hole and electron injection in HDs respectively. Current and EL profiles were stable for consecutive sweeps and presented no shoulders, unlike EDs and SDs. The highest current was around 0.67 mA/cm^2 (27μA) at 5.0V.
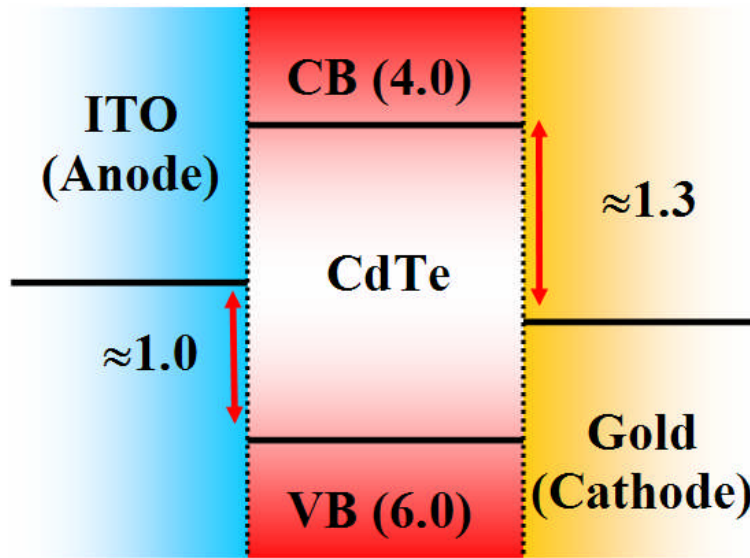
Figure 64. Band diagram of a hole-only device (HD). The barrier for electron injection is larger than the barrier for holes.

4.2.3.3 Time evolution of current and EL in air

Time evolution of current and electroluminescence were studied in fresh SDs, EDs and HDs. SDs and HDs were biased over their respective electroluminescence turn-on points, whereas EDs were biased at 2.5V to ensure the injection of carriers (see Figure 62). Figure 65 shows typical results for devices operated in air. Currents for EDs and SDs dropped 90% in about a minute, whereas HDs kept steady currents. Electroluminescence for SDs and HDs also dropped 90% in a minute (no light is obtained through the aluminium in EDs), without photoluminescence loss. For SDs, the decay in electroluminescence can be related to the decrease in current. However, this explanation is not valid for HDs, as the current remains steady in these devices.
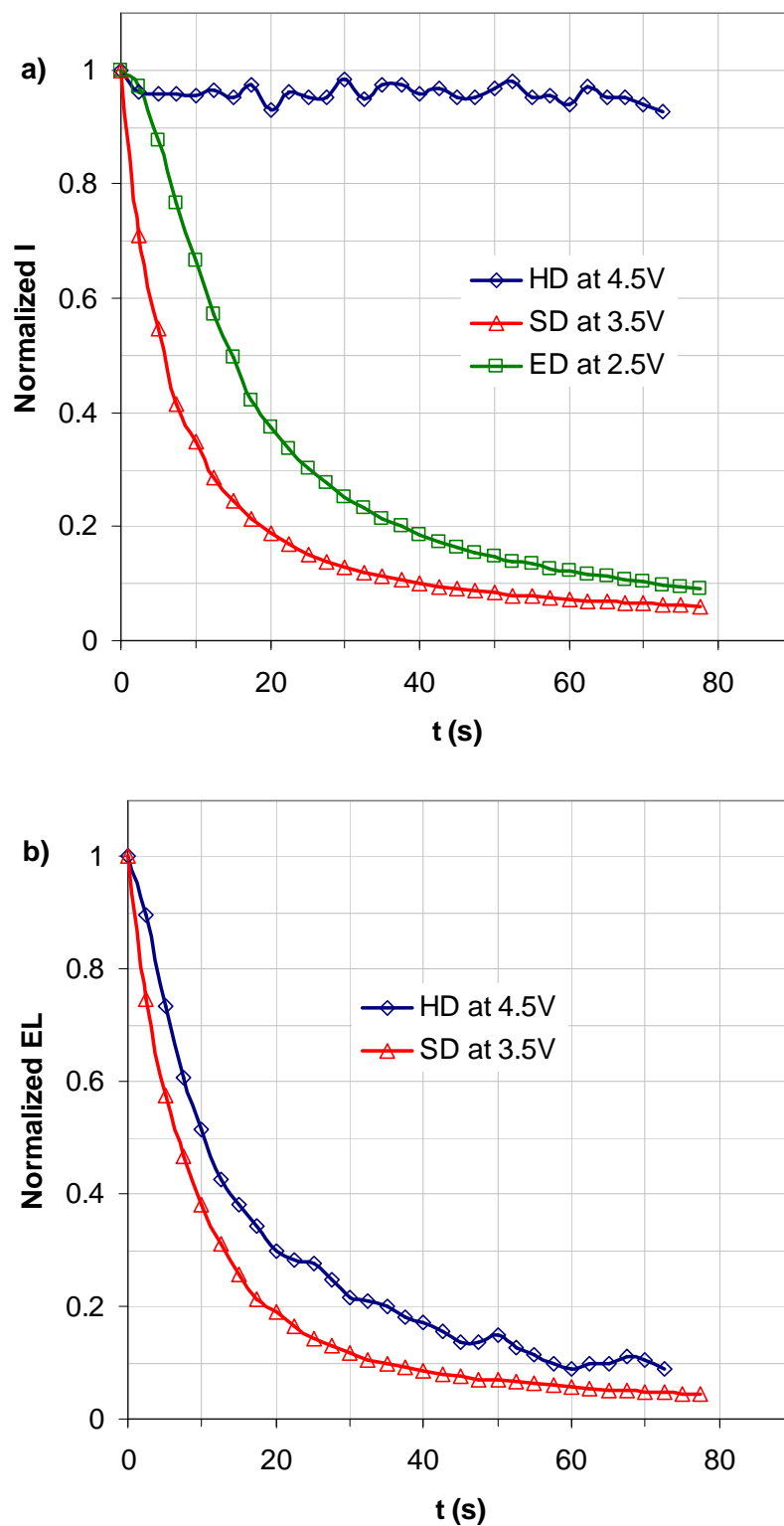
Figure 65. Normalized time evolution of (a) current and (b) electroluminescence of different types of devices operated in air. Current is stable only for HDs. Electroluminescence decays steeply for both HDs and SDs (light is blocked in EDs). In SDs, the electroluminescence decay is related to the loss of current. In HDs, the loss of emission is attributed to holes leaking to the cathode.

4.2.3.4 SDs operated in nitrogen (SDNs)

Fresh SDs where introduced in a chamber flooded with nitrogen, with only a small aperture for the connections to the external measurement equipments. A continuous flow of nitrogen was established, providing a positive pressure to balance losses through the aperture. Current and electroluminescence grew monotonically with increasing applied voltages (Figure 66 and Figure 67), showing no shoulders or collapse. Current onset point and EL turn-on voltage occurred around 2.1V and 2.5V respectively. A 10% loss of conductivity was noticeable between consecutive sweeps. Current levels were at least four times higher for SDNs over SDs in air. A 35% loss in conductivity and electroluminescence was measured after 10 minutes of continuous operation at 3.8V (Figure 68). These results show that SDNs are generally more stable than SDs, with maximum currents around four times higher than in SDs. However, according to the current onset and EL turn-on points, SDNs present the same inconsistency with the band diagram of Figure 59 as SDs do.
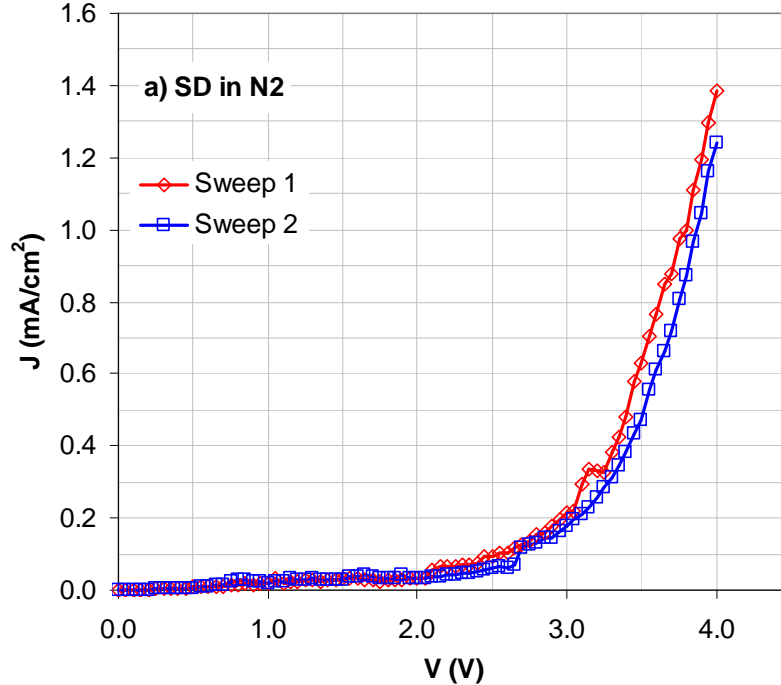
Figure 66. SDs operated in nitrogen (SDNs). Consecutive current-voltage curves grew monotonically, showing no shoulders or collapse. A slight decrease in current can be noticed between the first and second voltage sweeps. The current onset happened at 2.0V and the maximum current was around 1.38 mA/cm^2 (55μA) at 4.0V.
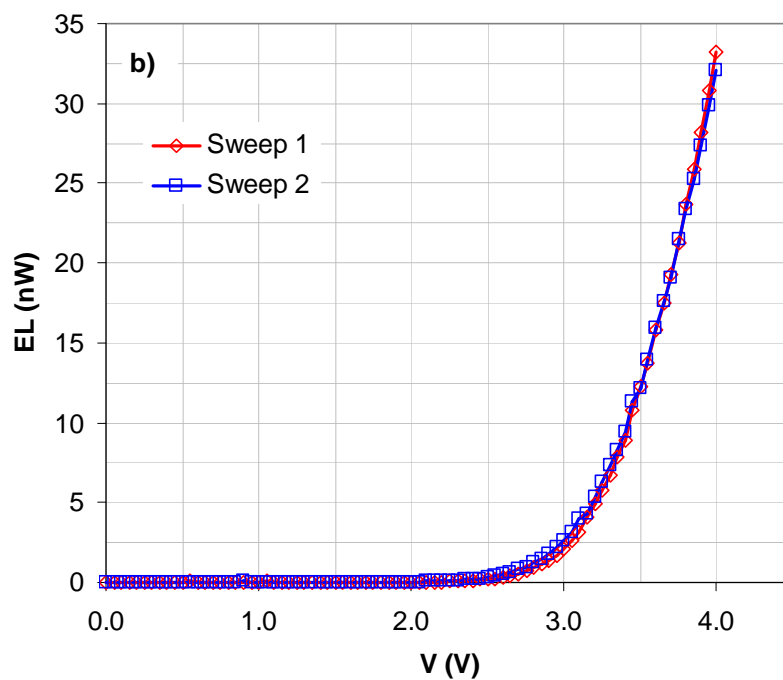
Figure 67. Electroluminescence in SDNs also grew monotonically, following the current, with no shoulder or collapse. The turn-on point was around 2.5V.
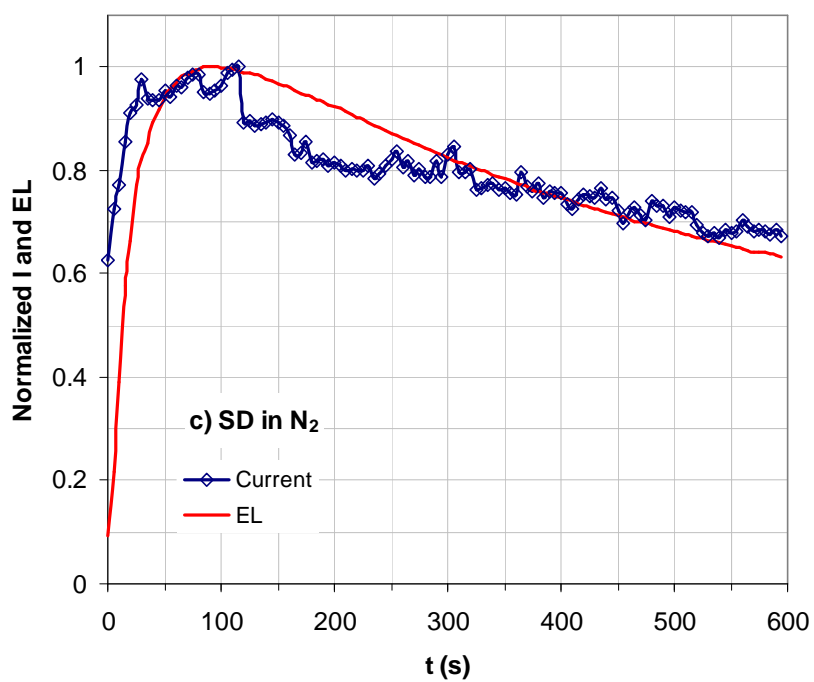
Figure 68. Time evolution of current and EL at 3.8V. A loss of 35% is observable in both quantities after 10 minutes of operation.

4.2.3.5 Aluminium cathode oxidation

The results presented previously have revealed a set of unexplained features. An explanation is presented in this subsection. The most important characteristics can be summarized as follows:

- Current in SDs and EDs drops steeply in time and in consecutive voltage sweeps
- Current in HDs is stable in time and in consecutive voltage sweeps
- Current in SDNs drops in time and in consecutive sweeps, but substantially less than in SDs and EDs
- Current profiles in EDs, SDs and SDNs do not match the behaviour predicted by their band diagrams, that predict lower current onsets.
- Current profiles in HDs are as expected from the band diagram
- EL drops 90% in about a minute for SDs and HDs, without associated PL loss
- EL drops 35% in 10 minutes in SDNs, without associated PL loss
- Maximum currents per device were: 1.38 mA/cm2 (55μA) in SDNs, 0.67 mA/cm2 (27μA) in HDs, 0.37 mA/cm2 (15.0μA) in SDs and 55.3 μA/cm2 (2.2μA) in EDs.

Although SDs and EDs have a low barrier for electron injection, their currents are lower than the current in HDs. This fact indicates the presence of a barrier for electron injection in SDs and EDs. This barrier must be related to the presence of air, as SDNs have higher currents than HDs, SDs and EDs. The evidence suggests that the barrier is located at the interface between the multilayer and the cathode. Degradation of the nanoparticles near the cathode interface might cause electron blocking. However, nanocrystal degradation would also cause loss in photoluminescence that can be readily investigated through visual inspection. The photoluminescence from the emissive area was checked after every test as explained in the experimental section (see also Figure 44Figure 45 and Figure 50), and no damage was detected.

The absence of damage indicates that the nanoparticles are not affected by physical changes that may cause the formation of a barrier. Thus, the only option remaining is an effect happening at the cathode itself. The development of an aluminium oxide barrier at the interface with the emissive layer is proposed as being responsible for the poor electron injection. According to this hypothesis, growth in interface coverage and/or in

thickness of this oxide barrier is induced by electrochemical reactions caused by the applied field. Continued operation causes a steady and irreversible drop in current and electroluminescence, as shown in the time-evolution curves (Figure 65). This would be also the cause of the collapsing current profiles for consecutive voltage sweeps in EDs and SDs.

The aluminium oxide layer introduces a modification in the band diagrams of devices with aluminium cathode. The modified band diagram of an SD is shown in Figure 69. The exact position of the edge of the conduction band of alumina depends on the conditions of formation of the interface with the aluminium[148]. Reported barriers with aluminium are around 1.6eV and 2.5eV.
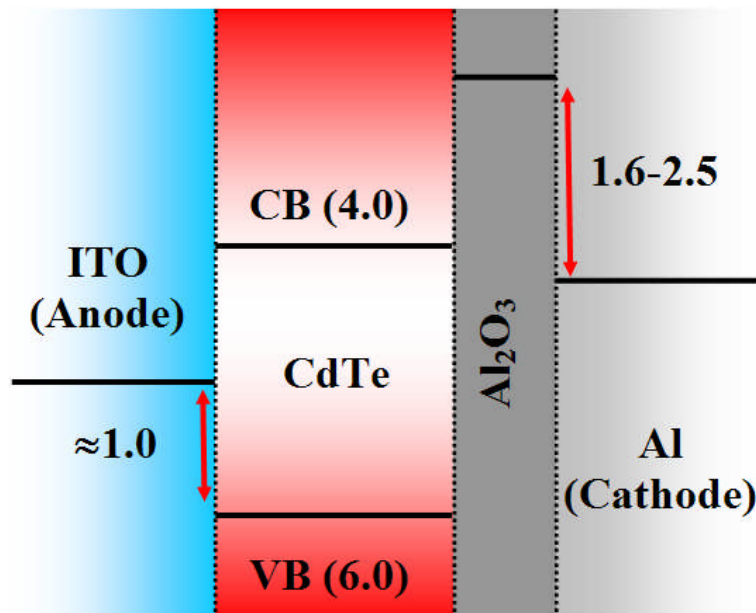
Figure 69. Alternative band diagram for the NLED (unit is eV). The alumina layer presents a barrier between 1.6eV and 2.5eV for electron injection. The barrier for hole injection is around 1.0eV.

When the samples are taken out of the chamber after cathode evaporation, the aluminium is fresh and it is not oxidised. This causes the photoluminescence quenching reported in Section 4.1.3. Exposure to air produces a thin coating of aluminium oxide on the surface of the cathode, responsible for the recovery of sample photoluminescence. The oxidation is possible due to the penetration of atmospheric oxygen through the multilayer, due to its porosity and the fact that the device is not sealed. The coating film produced spontaneously by contact with air, is called a *passivation layer* and is well

known in the industry. The oxide passivation layer in aluminium prevents its continued corrosion and weathering, a property that is widely used in a multitude of products. In SDs operated in air, the thickness of the oxide layer develops further due to electrochemical reactions, causing the collapse of current and electroluminescence.

The thickness of the passivation layer at the interface with the CdTe multilayer depends on the length of time the sample has spent in contact with air. It is thought that oxygen needs some time to diffuse through the multilayer and oxidise the metal. An indication of this is that the recovery of PL after cathode deposition does not happen immediately, but requires some 20 minutes. Environmental conditions like temperature and humidity also influence the rate of oxidation.

The different degrees of oxidation of the cathode are responsible for the differences found in the current onset points of EDs and SDs. Fresher aluminium favours a lower onset bias, while older aluminium films, with thicker passivation layers, would cause higher onset biases. Figure 70 illustrates this effect with a 30-layer sample with an aluminium-gold cathode. This composed cathode is made by depositing a thin layer of aluminium (around 1nm thick) and a layer of gold on top (*ca.* 200nm). When voltage sweeps were applied to the device, the aluminium layer started oxidising. The current onsets shifted to higher voltages in consecutive sweeps. Eventually, when the aluminium layer was completely oxidised, injection from gold was dominant and the current stabilized.

Samples tested in nitrogen also had a passivation layer. SDNs were exposed to the air after their manufacture, and the PL inspection after each sweep was done in air. However, nitrogen prevents further cathode oxidation during device operation. The comparatively slower degradation observed in SDNs is due to residual oxygen during device operation, entering through the small aperture in the chamber. Another cause might be the formation of aluminium nitride. HDs showed no degrading effects, as gold does not develop an oxide layer.
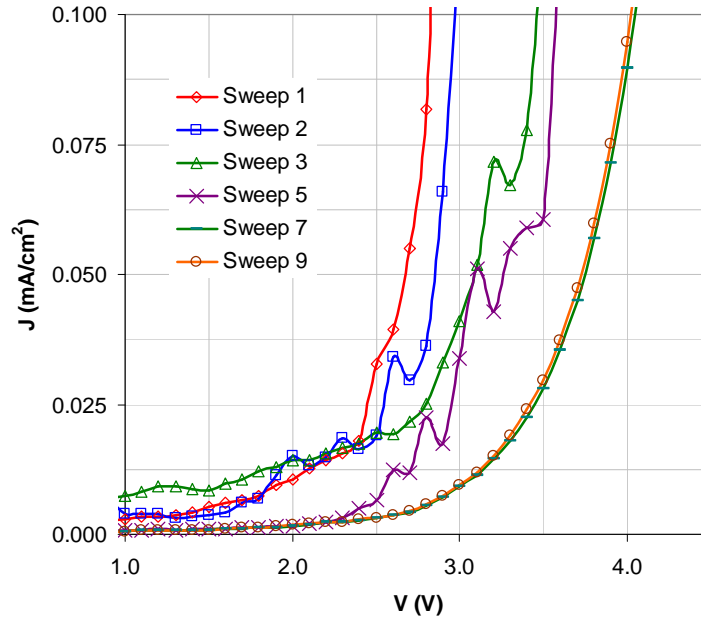
Figure 70. I-V curves from a 30-layer sample with Al+Au cathode. The aluminium layer is around 1nm thick. Each time a sweep is applied, the aluminium oxidises further. As this happens, the current onset point shifts towards higher voltages. In sweeps seven and nine the aluminium layer is completely oxidised, and injection from gold dominates. As gold does not oxidise, the onset points stabilize and the I-V curves become repeatable. The noisy patterns corresponding to sweeps one to five are due to the instability caused by the ongoing oxidation of the aluminium layer.

4.2.4 Field-assisted carrier injection

In the previous section, a new band diagram was proposed for the devices operated in air (Figure 69) in which the oxide layer is included. In a device with non-oxidised aluminium, the barrier for electron injection is smaller than the barrier for holes. However, the oxide makes the barrier for electrons higher than for holes. In this section, the I-V and EL-V data obtained from the different types of devices will be analysed to find out the biases at which electrons and holes are injected.

As shown in the band diagrams of Section 4.2.3 and subsections, the typical potential barriers involved in these devices are in the order of an electron-volt. As all the measurements were carried out in ambient laboratory conditions, the thermal energy (k_BT) was around 0.026eV, and can be ignored. Conversely, the electric field increased by 10^7 V/m for each volt applied, due to the small thickness of the emissive layer. The

field dependency of current was established in Section 4.2.1 with devices with different number of layers. At the same time, the drastic dependence of current and electroluminescence on the electrode materials indicates that the current is injection-limited. All these factors suggest that field emission is likely to be playing an important role[101].

In 1928 Fowler and Nordheim[149] published a study of the problem of emission of electrons at high electric fields. They found an equation for the electron emission from a metal to vacuum over a triangular barrier current, known the Fowler-Nordheim equation. Since then, it has been adapted to injection into semiconductors and insulators instead of the vacuum, in the form[100,101,148,150,151]:

$$I \propto F^2 \exp\left(-\frac{\kappa}{F}\right)$$

Eq. 12

where I is the current, F the electric field and κ is given by:

$$\kappa = \frac{8\pi\sqrt{2m^*}\phi^{3/2}}{3qh}$$

Eq. 13

Here m^* is the effective mass of the carrier in the semiconductor, ϕ is the barrier height, and q and h are the elementary charge and Planck's constant respectively. As discussed in the introduction (Section 2.4.3), band bending near the electrodes can be discarded due to the discontinuous nature of the semiconductor multilayer and its low conductivity. This allows us to consider triangular barriers for injection under the applied electric field, and the Fowler-Nordheim formula is then applicable[100,149]. The data from I-V curves will be represented in a Fowler-Nordheim (FN) plot through the equation:

$$Ln\left(\frac{I}{V^2}\right) = b - \frac{a}{V}$$

Eq. 14

where ($-a$) is the slope and b is the intersection with the I/V axis. Here, the applied voltage V is used instead of the field F, related to the thickness of the multilayer s by $F=V/s$. FN plots for a HD, an SDN and an SD in air are shown in Figure 71, Figure 72 and Figure 73 respectively, where A and B mark points of interest. Table 4 gives the

average voltages for current onset, EL turn-on, and points A and B for the different types of samples.

For the HD and SDN, there were two different regimes, joined by a transition region. From Table 4, point A can be related to the current onset, while point B happened near the EL turn-on. This indicates that the two different regimes represent areas dominated by different carriers. Data from HDs indicated that hole injection from the ITO happened near 2.0V. In consequence, point A marks the beginning of hole injection, whereas point B marks approximately electron injection.
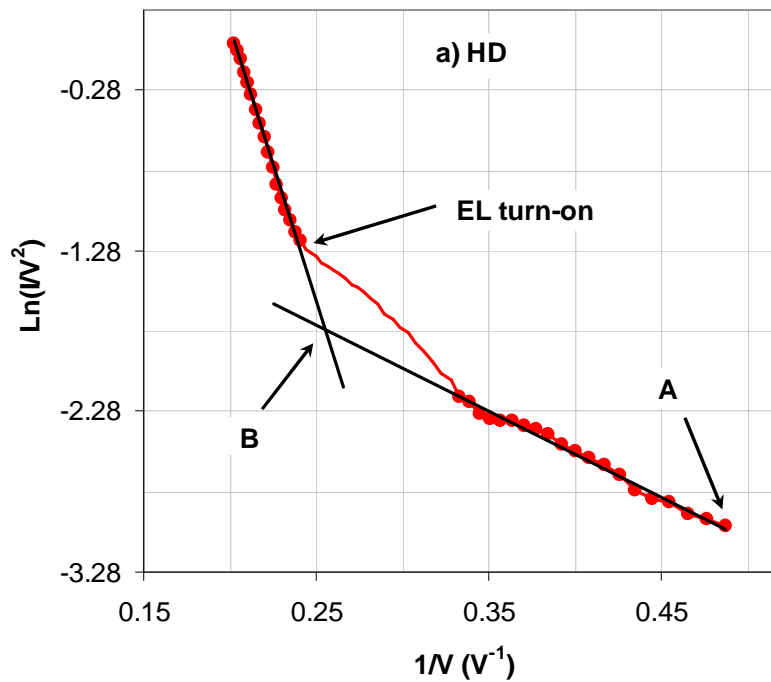
Figure 71. Fowler-Nordheim plot for the a HD. Points A and B mark hole and electron injection respectively.

For the SD the FN plots are different, as only one regime is observed. In SDs, point A happened near 2.0V, near the current onset, so it is related to hole injection. Point B marks the beginning of deviation from the FN fit, and always happened at higher bias than EL onset. EL marks the beginning of electron injection, as there is emission of light. The collapse of the current after point B indicates that the deviation from the FN fit is related to the beginning the oxidation of the cathode. Section 4.2.6 will try to explain the mechanisms for cathode oxidation in detail.
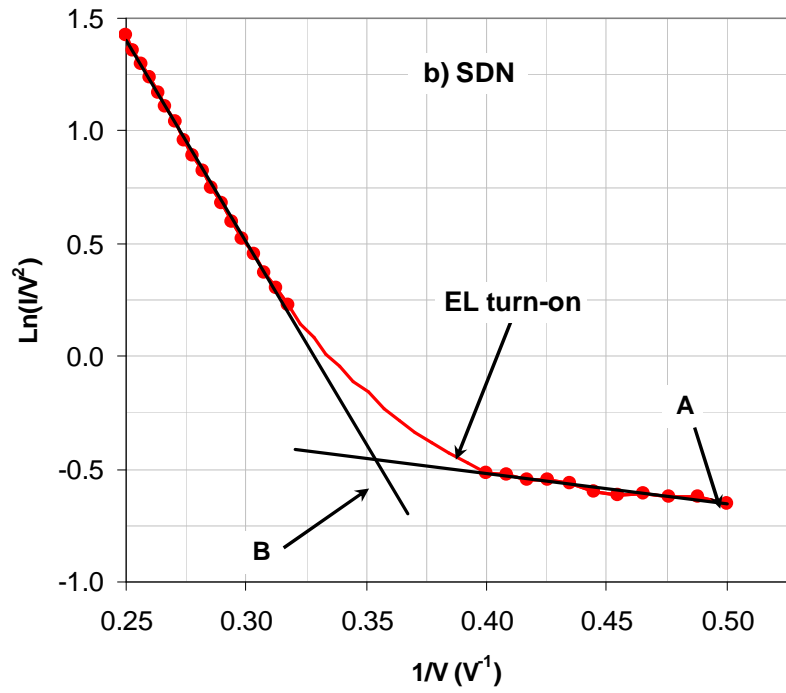
Figure 72. Fowler-Nordheim plot for the an SDN. Points A and B mark hole and electron injection respectively.
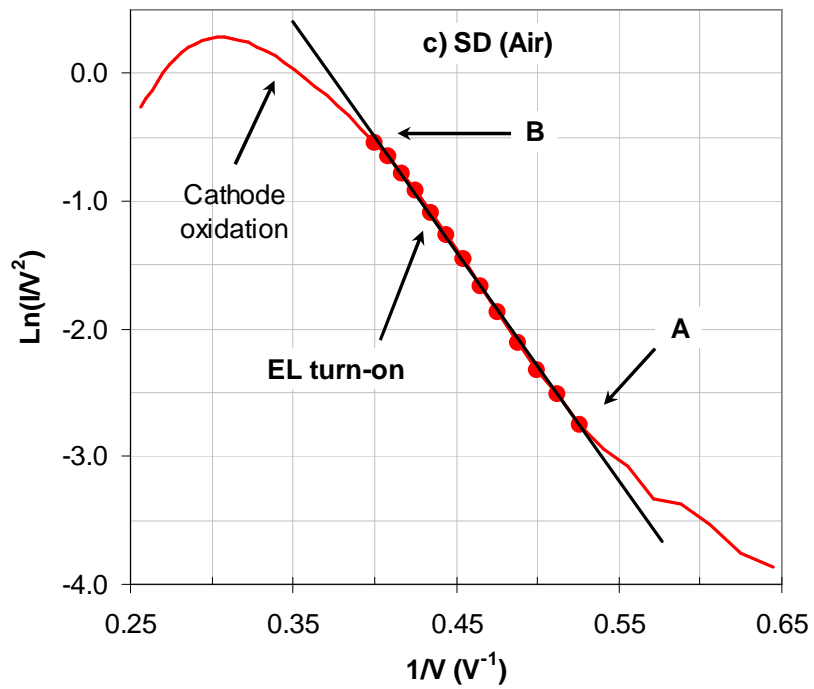
Figure 73. For an SD, point A generally marks hole injection of holes, whereas point B marks the beginning of the aluminium oxidation, characterized by a departure from the FN fit.

Table 4. Parameters from the Fowler-Nordheim fits. The parameters are compared with the average current on-set and turn-on voltages for each type of sample. (5 sweeps per sample type).

Sample	Onset		Turn-on		FN	
	V	Carrier	V	Carrier	A (V)	B (V)
HD	1.90 ± 0.17	h	4.18 ± 0.11	e	2.05	4.00
SDN	2.13 ± 0.13	h	2.55 ± 0.05	e	2.00	2.80
SD	1.97 ± 0.35	h	2.23 ± 0.08	e	1.90	2.50

The data presented in Figure 71 and Table 4 show that hole injection happens at lower bias than electron injection in SDs and SDNs, despite of the value of aluminium's work function. This further supports the hypothesis of the oxide barrier, as the aluminium-alumina barrier is higher than the ITO-multilayer barrier. An idea of how SDs work, based in the oxide hypothesis, is as follows: when the bias is applied, holes are injected first into the multilayer; the field transports them towards the multilayer-oxide interface. There, electrons and holes accumulate at opposite sides of the oxide layer (Figure 74). Increasing accumulation of holes triggers electron injection by concentrating the applied field across the oxide layer. The voltage at which this triggering happens defines the turn-on bias. The collapse of the current at point B is caused by further development of the oxide layer. A thicker oxide hampers the injection of both carriers, eventually causing the collapse of current and electroluminescence. Although this statement needs additional evidence, it is compatible with the absence of collapse in SDNs and HDs.
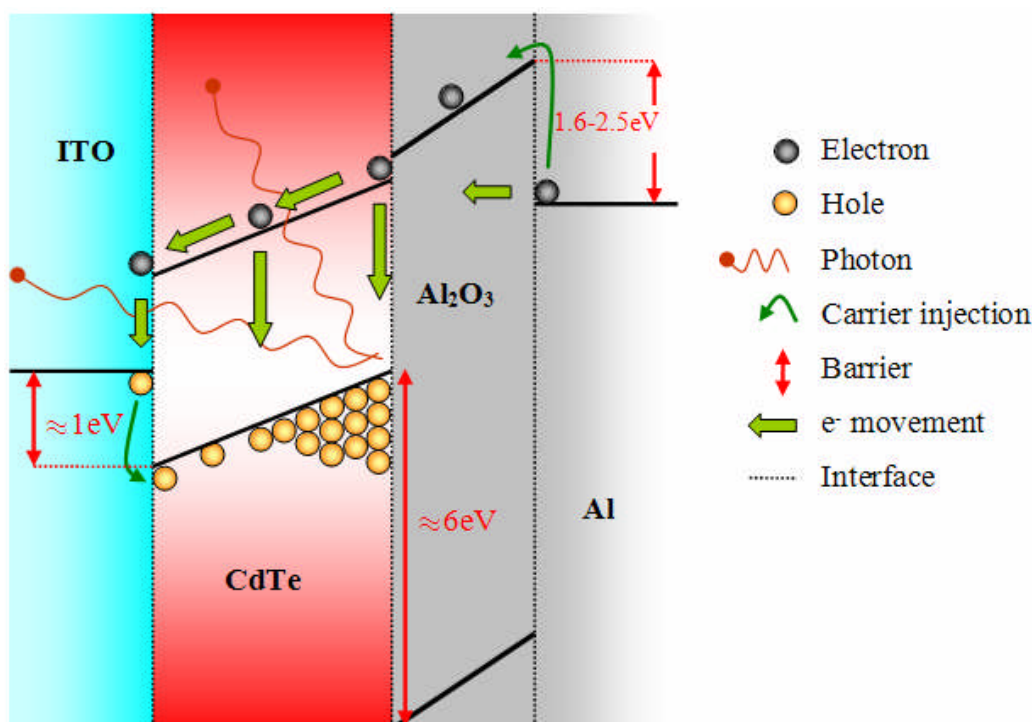
Figure 74. Schematics of an SD with an already developed aluminium oxide layer. When the device is biased, holes and electrons accumulate at both sides of the oxide, due to the high potential barriers for both carriers (around 6eV for holes and 1.6-2.5eV for electrons). At low fields, only a tiny amount of electrons cross the barrier through tunnelling, due to the relatively high thickness of the oxide. At sufficiently high fields, the electrons start tunnelling through the barrier into the conduction band of the aluminium oxide, and then into the conduction band of the nanoparticles. At this point, the electrons encounter a high concentration of holes in the nanoparticles; thus, a high proportion of the electrons recombine with the holes at the top of the valence band, emitting photons. The remaining electrons that did not recombine, would eventually cross the device and recombine at the anode; these electrons would contribute to the current, reducing efficiency.

4.2.5 Effects of the oxide layer on device performance

Light output from samples in an inert atmosphere was substantially lower compared to samples tested in air. The peak emission of SDs is almost 10 times higher than the peak of SDNs (Figure 75). Also, emission in SDNs peaks at higher currents than in SDs. (see Figure 75 and Figure 76). Despite the better stability found in SDNs, SDs have almost 10 times better external quantum efficiency (EQE) and power efficiency (Figure 77 and Figure 78). HDs also present efficiencies around 10 times lower than SDs. Hence, the oxide layer at the cathode interface plays a beneficial role for light emission.

In Section 4.2.4, it was proposed for SDs that the oxide layer accumulates holes and electrons at opposite sides, and that the field concentrates across the oxide (Figure 74). At the EL turn-on point, electrons start going through the oxide and enter into the multilayer. There, electrons encounter a high concentration of holes, representing a situation which is similar to minority carriers in a p-n junction. The result is a high probability that these electrons recombine radiatively. The high probability for radiative recombination caused by the oxide layer might justify the higher efficiency of SDs. Additionally, the oxide prevents *leakage currents*, caused by electrons flowing directly into the anode. Suppression of quenching effects near the metal electrode might also increase the efficiency.

In SDNs, the oxide barrier is incomplete or thin; thus, the accumulation of carriers at both sides of the oxide is not as high as in SDs, lowering the probability of radiative recombination. Also, leakage current is higher in SDNs, as they have higher current levels than SDs, but lower levels of EL. A higher leakage current reduces the efficiency.
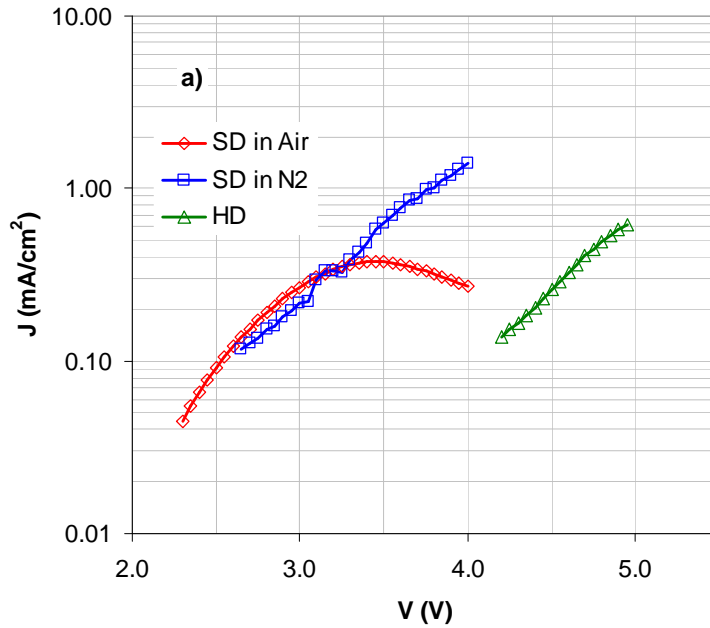
Figure 75. Comparison of current densities from SDs, SDNs and HDs. Both plots are restricted to the range of bias for which the devices emit light. SDs curves bent due to the oxidation of the cathode. The three types of device carry comparable current densities, but HDs need higher voltages to operate.
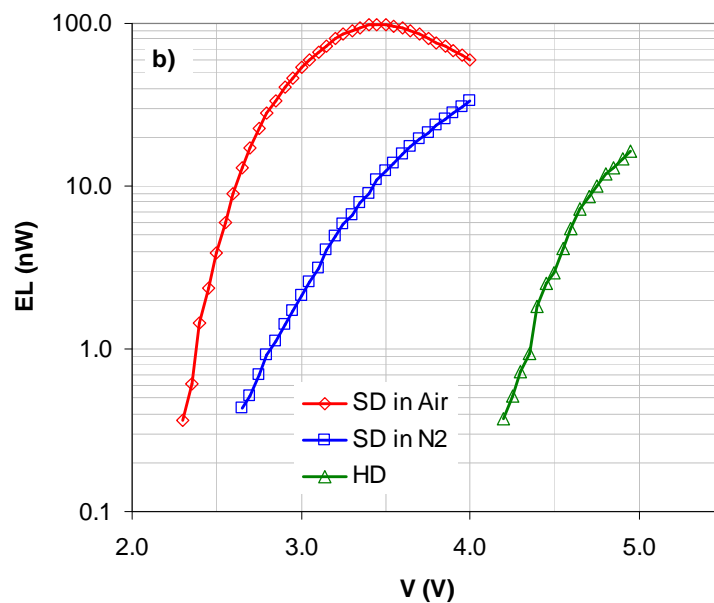
Figure 76. Comparison of EL power from SDs, SDNs and HDs. In terms of lighting power, SDs are the brightest devices by far, followed by SDNs and then HDs.
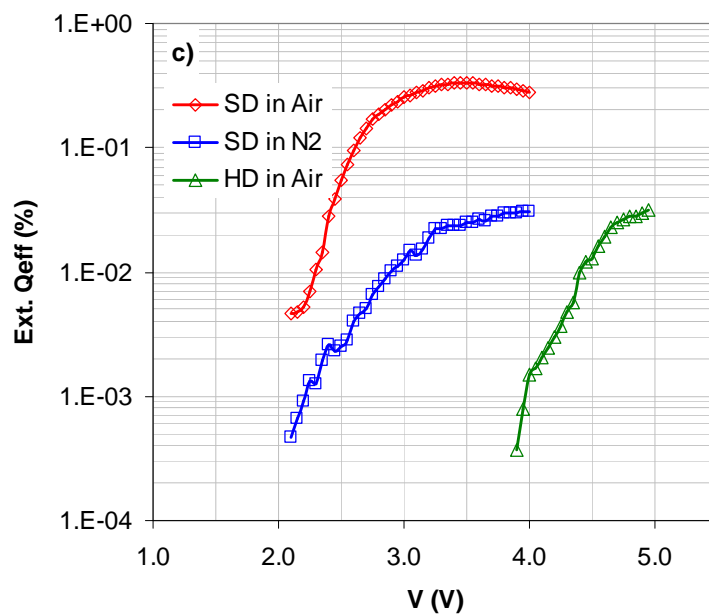
Figure 77. Comparison of the external quantum efficiency of SDS, SDNs and HDs. The efficiency of SDs is nearly an order of magnitude higher than the efficiency of SDNs and HDs.

105
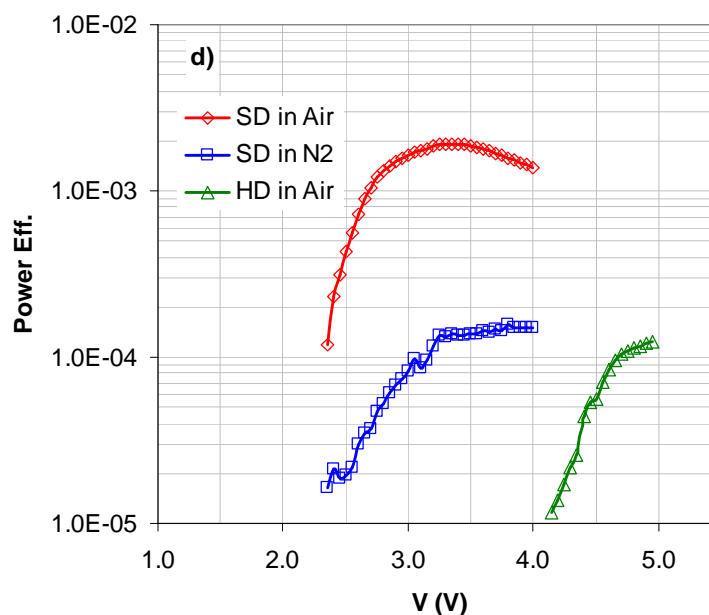
Figure 78. Comparison of the power efficiency of SDS, SDNs and HDs. The efficiency of SDs is nearly an order of magnitude higher than the efficiency of SDNs and HDs.

In summary, the aluminium oxide improves the efficiency by creating complementary charge accumulations across a thin interfacial layer. It also minimizes leakage current and prevents quenching effects at the cathode. The negative effects come from the dynamic growth in thickness of the oxide. The deposition of an interfacial dielectric layer of controlled thickness below the cathode could enable both current and time stability and high device efficiency through carrier accumulation.

The positive effects of field concentration at the oxide interface are similar to those found in OLED bilayers (Section 2.3.1). Moreover, a parallel can be established with the results of Fou et al. with PMA[89], Hung et al. with LiF[116,117] and Li et al. with alumina[120] (Section 2.3.1).

The absence of an oxide barrier can explain the short duration of EL in HDs (Figure 65b). A certain amount of holes might be stored in the device after hole injection and before electron injection. These holes might get trapped in sites along the multilayer in their way towards the cathode. When electrons are finally injected, they harvest the trapped holes, causing the emission transient. Once electron injection is steady, it dominates over hole current, as the CdTe nanoparticles are n-type. Most of the electron current will flow directly into the anode, due to the absence of barriers. This leakage current causes the substantial drop in light emission observed in HDs[37]. The transitory

build up of charge accumulation might be taken into advantage by using a pulsed operation[134]. The pulsed mode could also help to minimise leakage current.

4.2.6 The strength of the oxide barrier: rupture field

Experimental and theoretical current-field characteristics corresponding to the first voltage sweep on samples of 30, 40 and 50 layers have been plotted in Figure 79. The theoretical curves have been calculated using the coefficients *a* and *b* (Eq. 14) obtained from FN plots of the experimental data. It can be observed that for the three samples the departure from the theoretical FN model happens near the field value of 3×10^7 V/m. In Table 5 a more extended set of values is presented for samples of different number of layers; it can be seen that the field is the only common parameter for the divergence point. This value of field marks the point at which the aluminium layer starts to oxidize due to the operation of the device. At this point, the properties of the dielectric layer change and the consequence is a shoulder in current. From that point on, the measured currents are below the amount predicted by the model. It is believed that these changes might involve an increase in the thickness of the oxide layer, enlarging the barrier for electron injection.

Table 5. Parameters at the point of deviation of the experimental current at the first voltage sweep from the field emission model for a set of samples with different number of layers. The only common magnitude is the electric field, with an average value of 3×10^7 V/m and a deviation of 10% over the set.

Sample	Layers	Voltage	Field (V/m)	Current (µA)
CR#51-3	25	2.15	2.87E+07	0.28
CR#26-5	30	2.85	3.17E+07	0.80
CR#26-3	30	3.15	3.50E+07	0.35
CR#45-5	30	2.10	2.33E+07	5.42
CR#45-3	30	2.40	2.67E+07	4.45
CR#45-1	30	2.70	3.00E+07	6.13
CR#37-5	30	2.80	3.11E+07	0.74
CR#30-1	40	3.95	3.29E+07	2.50
CR#67-1	40	3.85	3.21E+07	0.71
CR#33-5	50	4.40	2.93E+07	1.57
CR#33-1	50	5.05	3.37E+07	1.54
CR#33-3	50	4.60	3.07E+07	1.09
		Average:	3.04E+07	
		Deviation (%):	10.46	
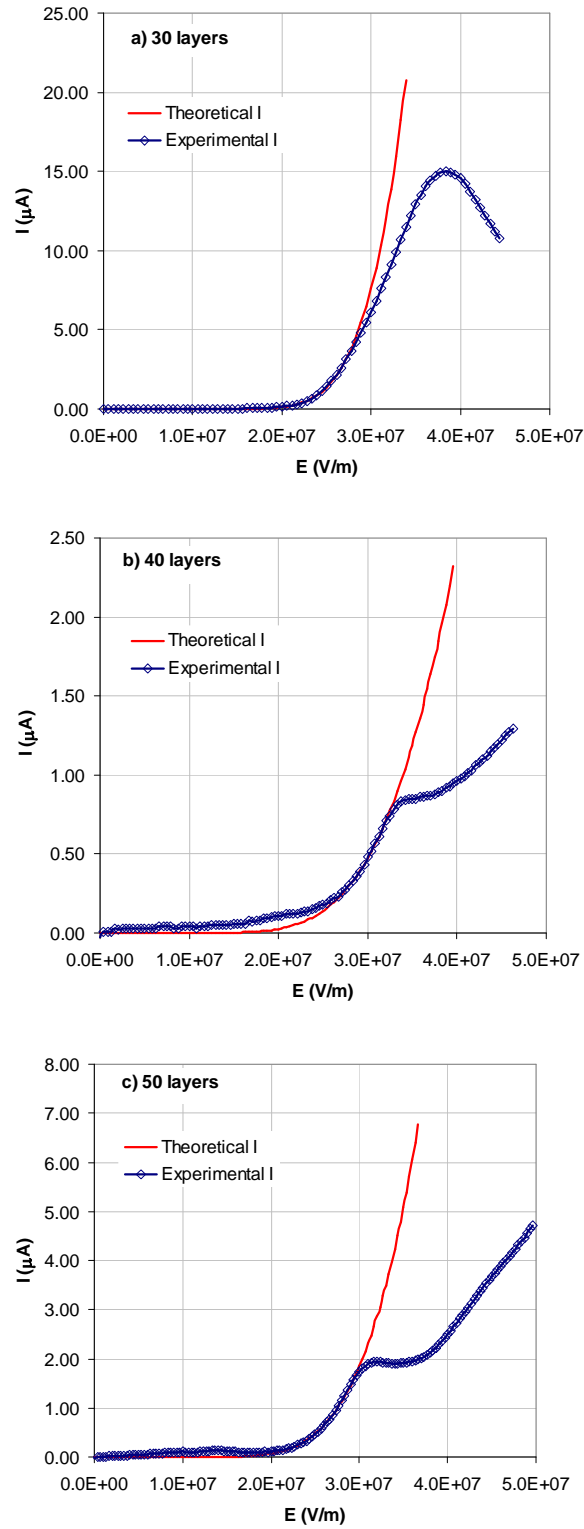
Figure 79. Experimental current-field plots for the first voltage sweep for samples of 30, 40 and 50 layers, compared with their best fits to the field emission model. The departure from the model happens at field values around 3×10^7 V/m , independently of the number of layers. This field is thought to be related to the electric breakdown of the interfacial aluminium oxide.

The dielectric strength of aluminium oxide varies depending on a number of parameters: thickness, impurity concentration, density of defects and others. A search in the literature provides values from 1×10^7 V/m up to 5×10^8 V/m, depending on deposition conditions and impurities concentration (e.g. Ahmed et al. (2005)[152] and Kolodzey et al. (2000)[153]). Thus, it seems plausible that the mechanism that takes place at the oxidation threshold is related to a dielectric breakdown in the oxide layer. Electrons would pass through the barrier by field emission, until the field is so high that the dielectric breaks down. This rupture would be a localized process, taking place at weak points randomly distributed across the oxide, in which the field is locally enhanced by defects or impurities. At these points, impact ionization can strip neighbouring non-oxidized aluminium atoms from valence electrons at a rate high enough as to favour the formation of aluminium oxide. Oxygen would be present due to diffusion, as the devices are operated in air. This could justify the oxidation of the aluminium in an electron-rich environment. Successive weak points would then be reinforced through additional oxidation, effectively increasing the thickness of the oxide layer. The field value at which the oxide undergoes breakdown will be referred as *rupture field*.

The rupture field is an average value that takes into account the thickness of the nanocrystal multilayer. However, the local field across the oxide might be higher than this average field. The relationship between the average field and the local field at the oxide will be investigated in future work. Experiments with metal-insulator-metal (MIM) structures with ultra-thin dielectric films have been planned in this direction.

4.2.7 Critical electric field and device degradation

The concept of critical field was introduced in the Section 4.2.1. At this value of field, the current starts rising at high rates while the electroluminescence drops substantially (Figure 80). The value of the critical field was found to be close to 4.5×10^7 V/m for 90% of the samples (mark the end of curves in Figure 51). This fact suggests the occurrence of a fundamental effect, independent of the particularities of each sample.

A possible explanation is that this field value might be close to the avalanche threshold[36]. When a carrier is injected into the emissive layers, it is accelerated by the electric field, acquiring momentum until it collides with the lattice, impurities,

nanoparticle boundaries or defects, releasing energy. At high field values, the injected carriers can gain enough energy between collisions to cause impact ionization. In this process, the carrier excites new electron-hole pairs. These newly created carriers can themselves gain enough energy to excite new pairs in an avalanche process. If the avalanche is not interrupted in its early stage, the changes in device conductivity are permanent and the device is destroyed. The energy released through collisions by a large number of high-energy carriers can raise the temperature locally causing structural damage to the nanocrystals and the device.

Although electroluminescence drops substantially after the critical field, it is still possible to observe some electroluminescence (Figure 80). In fact, pair production by impact ionization could favour radiative recombination. However, the proliferation of damaged nanoparticles results in an overall loss of electroluminescence. Irreversible nanoparticle damage over the critical field is confirmed by the permanent loss of photoluminescence. Also, subsequent voltage sweeps show no electroluminescence, signalling damage to the nanoparticles.
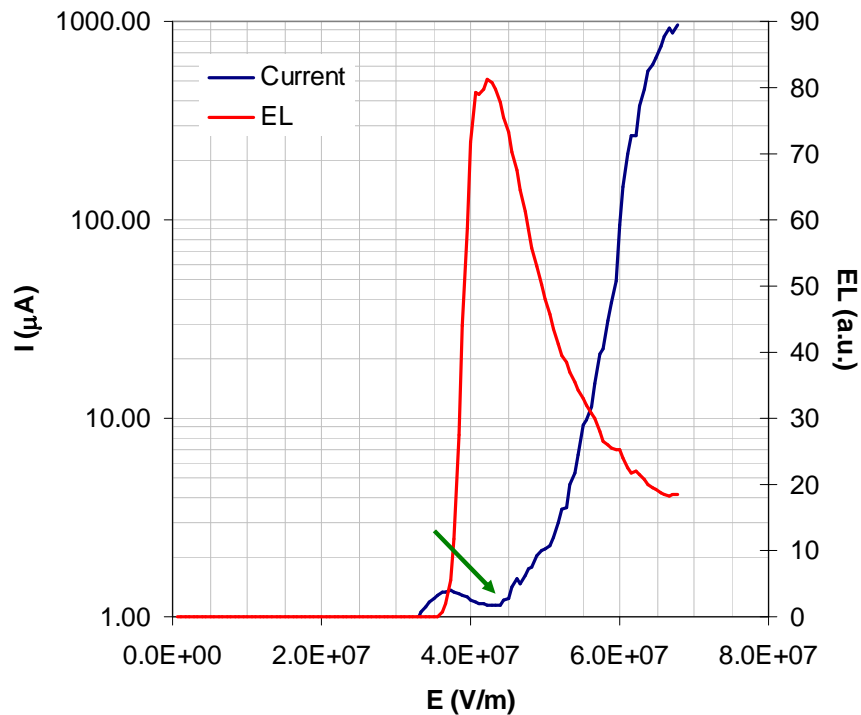
Figure 80. Device damage for a 30-layer sample at the critical field, around 4.5×10^7 V/m (marked by a green arrow). The current surge is accompanied by a drop in electroluminescence. There is still light emission after the critical field, but the decrease in its

intensity is associated to an irreversible degradation of the nanoparticles, as accounted by the loss of photoluminescence.

No specific research could be conducted within the timeframe of this work to investigate the cause of these degenerative effects. A possible explanation for nanocrystal damage might be related to the rupture of the sulphur-cadmium bonds at their surface and their substitution for oxygen-cadmium bonds[71]. These changes must be detectable and possible experiments are already under consideration.

4.2.8 Operational field range

It was shown in Section 4.2.1 that current starts flowing at fields between 2×10^7 V/m and 3×10^7 V/m for samples with 30, 40 and 50 layers. In order to include all cases, 2×10^7 V/m will be considered the lower limit of the field for device operation. The upper limit for operational fields is the critical field (4.5×10^7 V/m, Section 4.2.7), at which nanoparticle degradation starts.

According to these limiting fields it is possible to show the field region of operation for devices with different number of layers, as shown in Figure 81. The biases corresponding to the limiting fields depend on the number of layers of the device. The lower the number of layers, the narrower the range of operational biases. This explains the erratic behaviour found in 20-layer samples: small thickness inhomogeneities translate into high local variations of the field; these variations put the device out of the operational region. As the number of layers increases, the influence of thickness inhomogeneities decreases. However, higher voltages are required for light emission, lowering the efficiency. Consequently, a better control over thickness inhomogeneities might allow the use of lower number of layers; this could improve further the efficiency, as well as shortening the manufacturing time.

The rupture field could be also an important parameter for devices incorporating a controlled dielectric layer under the cathode. The breakdown of the dielectric allows additional current into the device. A certain increment in the number of electrons injected might increase the efficiency by increasing the number of radiative recombinations. However, an excessive amount of electrons would deplete the

accumulated reservoir of holes at the emissive layer; also, leakage current would be higher, lowering the efficiency. Consequently, the material of choice should have an appropriate dielectric strength.
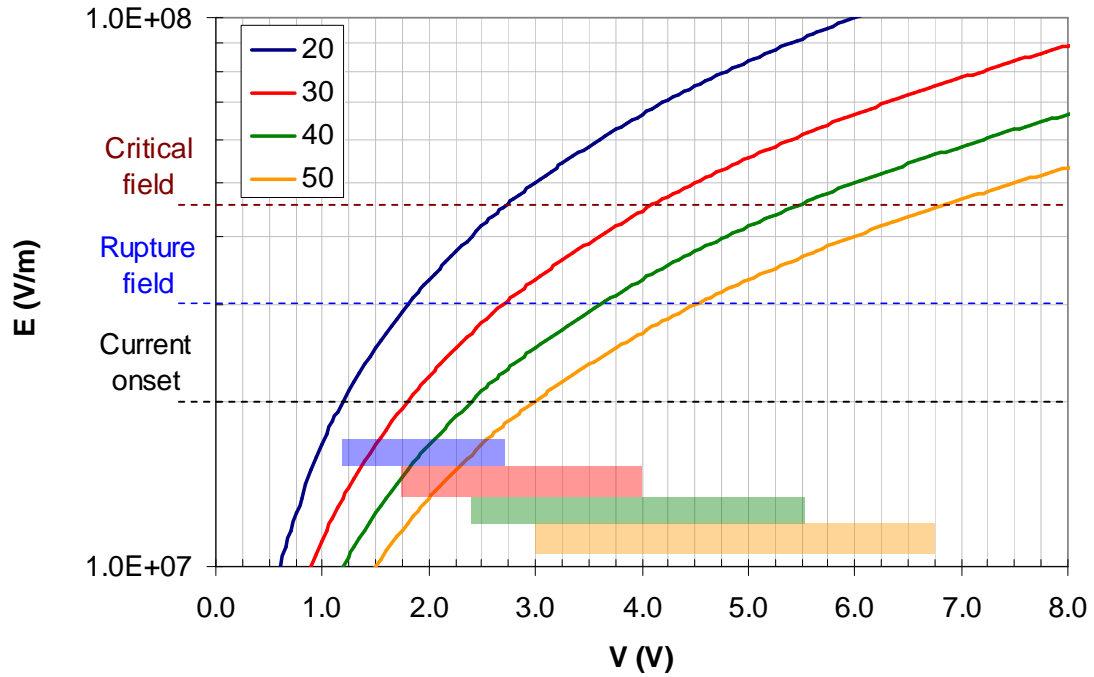
Figure 81. The region of device operation for samples with different number of layers. The operational region is limited from below by the onset of current (2×10^7 V/m) and from above by the critical field (4.5×10^7 V/m). The corresponding voltages depend on the number of layers of the device. The coloured bars at the bottom cover the ranges of operation of the different devices. It can be noticed that the range of operational biases increases with the number of layers.

MIM structures will help to identify a suitable blocking insulator. Experiments with MgF_2 and LiF have been scheduled for the near future. A more accurate definition of the device operational region is also an objective to be covered in future work.

5 Conclusions

It was pointed out in the introduction that it was necessary to gain a better understanding on the electrical characteristics of semiconductor nanocrystal films in order to enable the hybrid technology to a full development. This knowledge will also open the path for an NLED technology in a further step. Our efforts in this direction have been reported in this work.

In a first stage, a manual LbL technique was tested as a nanocrystal deposition technique. Despite the good results in terms of nanoparticle incorporation to the film and photoluminescence, electrical tests showed poor electrical stability. Samples presented frequent occurrence of pinholes and short-circuits, causing high current bursts and the early destruction of the sample. Electroluminescence results were poor in intensity and duration, making impossible spectral analyses. Microscopy observations revealed that the cause of electric failure was the porosity and inhomogeneity of the nanocrystal multilayer. Manually deposited films presented a porous network of clusters of nanoparticles; when the top metal electrode was deposited, the metal vapour penetrated through the pores and created short-circuits or areas of field enhancement that caused device failure.

Once the causes of device rupture were identified, it was thought that an automated LbL procedure might help producing smoother films. A robotic arm was programmed to do the deposition. It was also observed that, when the samples were retrieved from the different solutions, small drops remained attached to the surfaces. These drops might cause cross-contamination of the solutions, as well as inhomogeneous deposition at the surfaces. A slow sample removal routine was programmed, by which gravity and surface tension helped removing the drops and leaving a smooth, uncontaminated surface. A continuous-flow bath was also inserted in the setup, substituting a static bath. This helped in the removal of dangling polymer chains and poorly adhered nanocrystals. These modifications resulted in a substantial improvement in multilayer homogeneity and smoothness. Additionally, cathode evaporation distance was doubled to prevent thermal damage to the multilayer. First electrical tests showed a substantially higher throughput in electroluminescent samples. Improved electrical and luminescence

stability allowed spectral analysis, showing a good correspondence between electroluminescence and photoluminescence spectra.

After the establishment of a reliable manufacturing technique, the influence of the multilayer thickness on the electric behaviour was evaluated by measuring the effect of voltage on current and electroluminescence. A field dependency of the current-voltage characteristics was observed, with a current-onset field around $2\text{-}3\times10^7$ V/m. Also, it was found that 20-layer samples were much more unstable than samples with 30, 40 and 50 layers. Posterior analyses showed that the causes were related to avalanche effects into the multilayer, which were more pronounced and less controllable in samples with smaller thickness. The brightness was proportional to the current flowing through the samples. Samples with 30 layers were the brightest (1.42 cd/m^2) and most efficient (0.51% external quantum efficiency and 0.8 lm/W). For this reason, further analyses were done with 30-layer samples.

It was soon noticed that 30-layer samples presented degradation effects that were exclusively related to device operation, unlike previous issues related with structural defects. It was also noticed that the levels of current were substantially lower than expected from the band diagram of the structure. Single carrier devices were prepared to study these degenerative effects. Electron-only devices showed the same kind of current and electroluminescence collapse as standard samples, with even lower currents. Hole-only devices did not present degrading effects, but they showed very short-duration electroluminescence. To test the possible influence of operation in air, a batch of standard samples was tested in nitrogen. These samples showed substantially less current and electroluminescence drops than standard devices operated in air.

The conclusions from these experiments were that the aluminium cathodes were developing an oxide layer at the multilayer/cathode interface. This oxide layer grows when the device is operated in air, causing the collapse in current and electroluminescence. Despite this negative effect, it was noticed that samples with an oxide layer had better performance before the collapse than samples without the oxide. The reasons for this improvement are mainly three. First, the oxide causes the accumulation of holes and electrons at opposite sides of the oxide interface. Once electrons are injected into the multilayer, the high concentration of holes enables a high rate of radiative recombination. Second, the oxide concentrates the applied electric field

across itself, lowering the injection onset field. Finally, the presence of the oxide reduces the leakage current responsible for the poor electroluminescence in hole-only devices. The main conclusion from these analyses is that, if the thickness of the oxide layer could be kept stable, the effects of a blocking layer will be beneficial for device performance.

Fowler-Nordheim plots revealed that field emission is responsible for charge injection into the nanocrystal film. This result supports the adoption of a rigid-band model for the multilayer, with no band-bending or charge accumulation at the electrodes interfaces. This is justified by the poor charge densities and mobilities of carriers in the multilayer. Studies on the conduction mechanisms in the multilayer were not possible, due to the dominance of injection effects. However, now that carrier injection is better understood, reliable experiments to measure conductivity and carrier densities can be designed.

Fowler-Nordheim plots for samples with 30, 40 and 50 layers revealed that the beginning of aluminium cathode oxidation was taking place at fields near 3×10^7 V/m. We have found preliminary evidence supporting that this rupture field value is related with the dielectric breakdown of the aluminium oxide film. Although it will require additional evidence, it seems a reasonable explanation for the oxidation of aluminium in an electron-rich condition. A critical field of 4.5×10^7 V/m was also found, for which irreversible damage was inflicted upon the nanocrystals. This damage is associated with a dramatic increment in the current flow. Thus, we link this critical field with an avalanche effect caused by the high applied fields. Consequently, the operational range of these devices is limited from below by the current onset field, around 2×10^7 V/m, and from above by the critical field, around 4.5×10^7 V/m.

In summary, it has been demonstrated that the introduction of an interface providing charge separation and accumulation, and field concentration, is not only convenient to improve efficiency, but also necessary in order to minimize the effects of imbalanced injection barriers and of leakage current. The knowledge gathered on injection barriers, limiting operational fields and dynamic effects of operation in air, will enable reliable analyses on the conduction properties of nanocrystal films, like capacitance-voltage and photoconductivity measurements. The inclusion of inorganic buffer and carrier-transport layers could also introduce improvements, and will be studied in the

immediate future. The knowledge gained through this research will benefit the further development of the hybrid and NLED technologies.

6 Future work

The device structure used in this work has proved useful to reveal several electric and electroluminescence properties of nanocrystal films. However, the structure was just a first prototype for initial research on the topic. Some ideas for future investigation have come up during this research. The most immediate are listed here:

- The interfacial aluminium oxide layer in SDs will be studied by secondary ion mass spectrometry (SIMS). This technique can provide accurate information about the thickness of the oxide layer, as well as some details about the dynamics of its development.

- Charge transport mechanisms will be studied through capacitance-voltage and photocurrent measurements. Experiments will be carried out under vacuum or inert atmosphere, and with noble metal electrodes, to prevent oxide formation.

- Ultra-thin insulating film breakdown studies will be done in MIM structures with several insulating materials. These studies will try to identify suitable materials for carrier accumulation.

- The avalanche effects in nanocrystal films and the critical field will be investigated further, in order to clarify the limiting fields. X-ray diffraction (XRD) and X-ray photoelectron spectroscopy (XPS) will be used to determine the changes induced by the critical field.

- The inclusion of inorganic carrier-transport layers made of different materials will receive special emphasis, in an attempt to overcome the carrier transport limitations of nanocrystal films.

7 Reference List

1. S.H. Demtsu and J.R. Sites (2006), *Thin Solid Films*, Vol. 510, pp. 320-324.

2. E. Janik and R. Triboulet (1983), *J. Phys. D: Appl. Phys.*, Vol. 16, pp. 2333-2340.

3. B.O. Dabbousi , M.G. Bawendi, O. Onitsuka and M.F. Rubner (1995), *Appl. Phys. Lett.*, Vol. 66(11), pp. 1316-1318.

4. M. Gao, C. Lesser, S. Kirstein, H. Mohwald, A.L. Rogach and H. Weller (2000), *J. Appl. Phys.*, Vol. 87(5), pp. 2297-2302.

5. C.A. Leatherdale, C.R. Kagan, N.Y. Morgan, S.A. Empedocles, M.A. Kastner and M.G. Bawendi (2000), *Phys. Rev. B*, Vol. 62, pp. 2669-2680.

6. S. Chaudary, O. Mihrimah and W.C.W. Chan (2004), *Appl. Phys. Lett.*, Vol. 84, pp. 2925-2927.

7. M.A. Omar (1993), in *Elementary solid state physics: principles and applications*, Addison-Wesley Pub. Co., pp. 175-251.

8. M.G. Bawendi, M.L. Steigerwald and L.E. Brus (1990), *Annu. Rev. Phys. Chem.*, Vol. 41, pp. 477-496.

9. J. Singh (1996), in *Optoelectronics. An introduction to materials and devices*, McGraw-Hill, USA, pp. 177-235.

10. M. Voos, R.F. Leheny, and J. Shah (1980), in *Handbook on Semiconductors. Optical properties of solids.*, M. Balkanski (Editor), North-Holland Publishing Company, The Netherlands, pp. 329-416.

11. M. Lannoo, C. Delerue and G. Allan (1996), *Journal of Luminescence*, Vol. 70, pp. 170-184.

12. A.P. French and E.F. Taylor (1978), in *An introduction to quantum physics.* CRC Press, US, pp. 605-643.

13. P.W. Atkins (1994), in *Physical Chemistry*, Oxford University Press, UK, pp. 421-460.

14. Y. Marfaing (1980), in *Handbook on Semiconductors. Optical properties of solids.*, M. Balkanski (Editor), North-Holland Publishing Company, The Netherlands, pp. 417-495.

15. A.R. Brown, N.C. Greenham, J.H. Burroughes, D.D.C. Bradley , R.H. Friend, P.L. Burn, A. Kraft and A.B. Holmes (1992), *Chem. Phys. Lett.*, Vol. 200, pp. 46-54.

16. V.L. Colvin, M.C. Schlamp and A.P. Alivisatos (1994), *Nature*, Vol. 370, pp. 354.

17. S.V. Gaponenko (1998), in *Optical properties of semiconductor nanocrystals*, Cambridge University Press, Cambridge, UK, pp. 1-26.

18. Y. Wang and N. Herron (1991), *J. Phys. Chem.*, Vol. 95, pp. 525-532.

19. V.P. Gribkovskii, L.G. Zimin, S.V. Gaponenko, I.E. Malinovskii, P.I. Kuznetsov and G.G. Yakushcheva (1990), *Phys. Status Solidi B*, Vol. 158, No. 1, pp. 359-366.

20. M.A. Omar (1993), in *Elementary solid state physics: principles and applications*, Addison-Wesley Pub. Co., pp. 253-318.

21. M.H. Pilkuhn (1981), in *Handbook on semiconductors. Device Physics*, C. Hilsum (Editor),

Elsevier Science Publishers, The Netherlands, pp. 539-616.

22. L. Brus (1986), *J. Phys. Chem.* , Vol. 90, pp. 2555-2560.

23. L.I. Berger and B.R. Pamplin (2006), in *CRC Handbook of Chemistry and Physics, Internet Version 2006, <http://www.hbcpnetbase.com>*, D.R. LideCRC Press,

24. M.P. Shaw (1981), in *Handbook on semiconductors. Device Physics*, C. Hilsum (Editor), Elsevier Science Publishers, The Netherlands, pp. 1-85.

25. J. Singh (1996), in *Optoelectronics. An introduction to materials and devices*, McGraw-Hill, USA, pp. 294-337.

26. P.W. Atkins (1994), in *Physical Chemistry*, Oxford University Press, UK, pp. 539-589.

27. D. Ingert, N. Feltin, L. Levy, P. Gouzerh and M.P. Pileni (1999), *Adv. Mater.*, Vol. 11, No. 3, pp. 220-223.

28. Y.C. Tseng, M. Tzolov, E.H. Sargent, P.W. Cyr and M.A. Hines (2002), *Appl. Phys. Lett.*, Vol. 81, pp. 3446-3448.

29. S. Perkowitz (1993), in *Optical characterization of semiconductors*, Academic Press, US, pp. 45-59.

30. A.M. Kapitonov, A.P. Stupak, S.V. Gaponenko, E.P. Petrov, A.L. Rogach and A. Eychmüller (1999), *J. Phys. Chem B*, Vol. 103, pp. 10109-10113.

31. S.R. Forrest , D.D.C. Bradley and M.E. Thompson (2003), *Adv. Mater.*, Vol. 15, No. 13, pp. 1043-1048.

32. Palmer, J. M., Research Prof. Optical Sciences Centre. University of Arizona., *Radiometry and photometry FAQ*, (http://www.optics.arizona.edu/Palmer/rpfaq/rpfaq.htm).

33. N.C. Greenham, R.H. Friend and D.D.C. Bradley (1994), *Adv. Mater.*, Vol. 6, No. 6, pp. 491-494.

34. J.S. Kim, P.K.H. Ho, N.C. Greenham and R.H. Friend (2000), *J. Appl. Phys.*, Vol. 88, No. 2, pp. 1073-1081.

35. Yeo, R. (*Basics of display masurements*, 18/Jan./2006, Bletchley Park. Milton Keynes. MK3 6EB. UK.

36. C. Hilsum. *Handbook on semiconductors. Device Physics,* Vol.4, First Edition, Elsevier Science Publishers, 1981.

37. H. Mattoussi , L.H. Radzilowski, B.O. Dabbousi, E.L. Thomas , M.G. Bawendi and M.F. Rubner (1998), *J. Appl. Phys.*, Vol. 83, No. 12, pp. 7965-7974.

38. S.V. Gaponenko. *Optical properties of semiconductor nanocrystals*, Cambridge University Press, 1998.

39. H. Weller (1993), *Adv. Mat.*, Vol. 5, No. 2, pp. 88-95.

40. A.P. Alivisatos (1996), *Science*, Vol. 271, pp. 933-937.

41. Y. Kayanuma (1988), *Phys. Rev. B*, Vol. 38, No. 14, pp. 9797-9805.

42. A.L. Efros and A.L. Efros (1982), *Sov. Phys. Semicond.*, Vol. 16, pp. 772-775.

43. S.V. Gaponenko (1998), in *Optical properties of semiconductor nanocrystals*, Cambridge

University Press, Cambridge, UK, pp. 27-54.

44. Y. Kayanuma (1986), *Solid State Commun.*, Vol. 59, No. 6, pp. 405-408.

45. L.E. Brus (1983), *J. Chem. Phys.*, Vol. 79, No. 11, pp. 5566-5571.

46. R. Rossetti, S. Nakahara and L.E. Brus (1983), *J. Chem. Phys.*, Vol. 79, pp. 1086-1088.

47. C.B. Murray, D.J. Norris and M.G. Bawendi (1993), *J. Am. Chem. Soc.*, Vol. 115, pp. 8706-8715.

48. A.L. Rogach, A. Katsikas, A. Kornowski, D. Su, A. Eychmüller and H. Weller (1996), *Ber. Bunsenges. Phys. Chem.*, Vol. 100, pp. 1772-1778.

49. Al.L. Efros and M. Rosen (1998), *Phys. Rev. B*, Vol. 58, No. 11, pp. 7120-7135.

50. A.L. Efros, M. Rosen, M. Kuno, M. Nirmal, D.J. Norris and M. Bawendi (1996), *Phys. Rev. B*, Vol. 54, pp. 4843-4856 .

51. M. Nirmal, D.J. Norris, M. Kuno and M.G. Bawendi (1995), *Phys. Rev. Lett.*, Vol. 75, No. 20, pp. 3728-3731.

52. A. Eychmüller (2000), *J. Phys. Chem. B*, Vol. 104, pp. 6514-6528 .

53. D. Wasserman and S.A. Lyon (2004), in *Handbook of electroluminescence materials*, D.R. Vij (Editor), IOP Publishing Ltd, London, UK, pp. 245-281.

54. R.M. Penner (2001), in *Electrochemistry of nanomaterials*, G. Hodes (Editor), Wiley-VCH, Weinheim, pp. 1-24.

55. G. Hodes and I. Rubinstein (2001), in *Electrochemistry of nanomaterials*, G. Hodes (Editor), Wiley-VCH, Weinheim, pp. 1-24.

56. T.A. Klar, T. Franzl, A.L. Rogach and J. Feldmann (2005), *Adv. Mater.*, Vol. 17, pp. 769-773.

57. M. Grundmann (1999), *Physica E*, Vol. 5, pp. 167-184.

58. A. Henglein (1982), *J. Phys. Chem.*, Vol. 86, pp. 2291-2293.

59. Kalyuzhny G. and Murray R. W. (2005), *J. Phys. Chem. B*, Vol. 109, pp. 7012-7021.

60. B.O. Dabbousi, J. Rodriguez-Viejo, F.V. Mikulec, J.R. Heine, H. Mattoussi, R. Ober, K.F. Jensen and M.G. Bawendi (1997), *J. Phys. Chem. B*, Vol. 101, pp. 9463-9475.

61. D.V. Talapin , S. Haubold, A.L. Rogach, A. Kornowski, M. Haase and H. Weller (2001), *J. Phys. Chem. B*, Vol. 105, pp. 2260-2263.

62. Y. Cao and U. Banin (2000), *J. Am. Chem.Soc.*, Vol. 122, pp. 9692-9702.

63. L. Bakueva, S. Musikhin, M.A. Hines, T.W.F. Chang, M. Tzolov, G.D. Scholes and E.H. Sargent (2003), *Appl. Phys. Lett.*, Vol. 82, pp. 2895-2897.

64. H. Bao, Y. Gong, Z. Li and M. Gao (2004), *Chem. Mater.*, Vol. 16, pp. 3853-3859.

65. Z.A. Peng and X. Peng (2001), *J. Am. Chem. Soc.*, Vol. 123, pp. 183-184.

66. L. Qu and X. Peng (2001), *J. Am. Chem. Soc.*, Vol. 124, No. 9, pp. 2049-2055.

67. L. Spanhel, M. Haase, H. Weller and A. Henglein (1987), *J. Am. Chem. Soc.*, Vol. 109, pp. 5649-5655.

68. T. Vossmeyer , L. Katsikas, M. Giersig, I.G. Popovic, K. Diesner, A. Chemseddine, A. Eychmüller and H. Weller (1994), *J. Phys. Chem.*, Vol. 98, pp. 7665-7673.

69. A.L. Rogach, A. Kornowski, M. Gao, A. Eychmüller and H. Weller (1999), *J. Phys. Chem. B*, Vol. 103, pp. 3065-3069.

70. A. Rogach, S. Kershaw, M. Burt, M. Harrison, A. Kornowski, A. Eychmüller and H. Weller (1999), *Adv. Mater.*, Vol. 11, No. 7, pp. 552-555.

71. N.P. Gaponik , D.V. Talapin, A.L. Rogach, K. Hoppe, E.V. Shevchenko, A. Kornowski, A. Eychmüller and H. Weller (2002), *J. Phys. Chem. B*, Vol. 106, pp. 7177-7185.

72. M. Gao, S. Kirstein, H. Möwald, A.L. Rogach, A. Kornowski, A. Eychmüller and H. Weller (1998), *J. Phys. Chem. B*, Vol. 102, pp. 8360-8363.

73. A.L. Rogach (2000), *Mater. Sci. Eng. B*, Vol. 69-70, pp. 435-440.

74. J. Aldana, Y.A. Wang and X. Peng (2001), *J. Am. Chem. Soc.*, Vol. 123, pp. 8844-8850.

75. L. Qu, Z.A. Peng and X. Peng (2001), *Nano Lett.*, Vol. 1, No. 6, pp. 333-337.

76. E. Hetch (1998), in *Optics*, Addison-Wesley, US, pp. 37-84.

77. T. Tanaka, Y. Kobayashi, T. Mitani, K. Nakazawa, K. Oonuki, G. Sato, T. Takahashi and S. Watanabe (2004), *New Astronomy Reviews*, Vol. 48, pp. 309-313.

78. K.B. Blodgett and I. Langmuir (1937), *Phys. Rev.*, Vol. 51, pp. 964-983.

79. K. Blodgett (1934), *J. Am. Chem. Soc.*, Vol. 56, pp. 495.

80. G. Decher, J.D. Hong and J. Schmitt (1992), *Thin Solid Films*, Vol. 210, pp. 831-835.

81. J. Schmitt, G. Decher, W.J. Dressick, S.L. Brandow, R.E. Geer, R. Shashidhar and J.M. Calvert (1997), *Adv. Mater.*, Vol. 9 (1), pp. 61-65.

82. G. Decher (1997), *Science*, Vol. 277, pp. 1232-1237.

83. A.V. Dobrynin and M. Rubinstein (2005), *Prog. Polym. Sci.*, Vol. 30, pp. 1049-1118.

84. S.L. Clark, M.F. Montague and P.T. Hammond (1997), *Macromolecules*, Vol. 30, pp. 7237-7243.

85. M. Gao, B. Richter and S. Kirstein (1997), *Adv. Mater.*, Vol. 9, pp. 802-805 .

86. M. Gao, B. Richter, S. Kirstein and H. Mohwald (1998), *J. Phys. Chem.*, Vol. 102, pp. 4096-4103.

87. W. Chen, D. Grouquist and J. Roark (2002), *J. Nanosci. Nanotech.*, Vol. 2, No. 1, pp. 47-53.

88. M. Gao, X. Zhang, B. Yang, F. Li and J. Shen (1996), *Thin Solid Films*, Vol. 284-285, pp. 242-245.

89. A.C. Fou, O. Onitsuka, M. Ferreira, M.F. Rubner and B.R. Hsieh (1996), *J. Appl. Phys.*, Vol. 79 (10), pp. 7501-7509.

90. Y. Lvov, K. Ariga, I. Ichinose and T. Kunitake (1995), *J. Am. Chem. Soc.*, Vol. 117, pp. 6117-6123.

91. Y. Lvov, K. Ariga, I. Ichinose and T. Kunitake (1996), *Langmuir*, Vol. 12, pp. 3038-3044.

92. Z. Tang, Y. Wang and N.A. Kotov (2002), *Langmuir*, Vol. 18, pp. 7035-7040.

93.   T. Tsutsui (2002), *Nature*, Vol. 420, pp. 752-755.

94.   W. Hwang and K.C. Kao (1973), *J. Chem. Phys.*, Vol. 58, No. 8, pp. 3521-3522.

95.   P.S. Vincett , W.A. Barlow, R.A. Hann and G.G. Roberts (1982), *Thin Solid Films*, Vol. 94, pp. 171-183.

96.   C.W. Tang and S.S. VanSlyke (1987), *Appl. Phys. Lett.*, Vol. 51, No. 12, pp. 913-915.

97.   D.C. Freeman and C.E. White (1956), *J. Am. Chem. Soc.*, Vol. 78, pp. 2678-2682.

98.   J.H. Burroughes, D.D.C. Bradley, A.R. Brown, R.N. Marks, K. Mackay, R.H. Friend, P.L. Burns and A.B. Holmes (1990), *Nature*, Vol. 347, pp. 539-541.

99.   H. Eckhardt, L.W. Shacklette, K.Y. Jen and R.L. Elsenbaumer (1989), *J. Chem. Phys.*, Vol. 91, No. 2, pp. 1303-1315.

100.   I.D. Parker (1994), *J. Appl. Phys.*, Vol. 75, No. 3, pp. 1656-1666.

101.   A.J. Heeger, I.D. Parker and Y. Yang (1994), *Synthetic Metals*, Vol. 67, pp. 23-29.

102.   H. Tomozawa, D. Braun, S.D. Phillips, R. Worland and A.J. Heeger (1989), *Synth. Met.*, Vol. 28, pp. 687-690.

103.   D. Braun and A.J. Heeger (1991), *Appl. Phys. Lett.*, Vol. 58, No. 18, pp. 1982-1984.

104.   S. Karg, M. Meier and W. Riess (1997), *J. Appl. Phys.*, Vol. 82, No. 4, pp. 1951-1960.

105.   M. Meier, S. Karg and W. Riess (1997), *J. Appl. Phys.*, Vol. 82, No. 4, pp. 1961-1966.

106.   C. Adachi, T. Tsutsui and S. Saito (1989), *Appl. Phys. Lett.*, Vol. 55, No. 15, pp. 1489-1491.

107.   A.R. Brown, D.D.C. Bradley, J.H. Burroughes, R.H. Friend, N.C. Greenham, P.L. Burn, A.B. Holmes and A. Kraft (1992), *Appl. Phys. Lett.*, Vol. 61, No. 23, pp. 2793-2795.

108.   C. Adachi, T. Tsutsui and S. Saito (1990), *Appl. Phys. Lett.*, Vol. 56, No. 9, pp. 799-801.

109.   H. Spreitzer, H. Becker, E. Kluge, W. Kreuder, H. Schenk, R. Demandt and H. Schoo (1998), *Adv. Mater.*, Vol. 10 (16), pp. 1340-1343.

110.   C.W. Tang, S.A. VanSlyke and C.H. Chen (1989), *J. Appl. Phys.*, Vol. 65, No. 9, pp. 3610-3616.

111.   C. Adachi, M.A. Baldo, M.E. Thompson and S.R. Forrest (2001), *J. Appl. Phys.*, Vol. 90, No. 10, pp. 5048-5051.

112.   M.K. Nazeeruddin, R. Humphry-Baker, D. Berner, D. Rivier, L. Zuppiroli and M. Graetzel (2003), *J. Am. Cham. Soc.*, Vol. 125, pp. 8790-8797.

113.   J. Liu, Y. Shi, T.F. Guo, and Y. Yang (2004), in *Handbook of electroluminescence materials*, D.R. Vij (Editor), IOP Publishing Ltd, London, UK, pp. 531-582.

114.   O. Onitsuka , A.C. Fou, M. Ferreira, B.R. Hsieh and M.F. Rubner (1996), *J. Appl. Phys.*, Vol. 80, No. 7, pp. 4067-4071.

115.   J.E. Malinsky, G.E. Jabbour, S.E. Shaheen, J.D. Anderson, B. Kippelen, P. Dutta and N. Peyghambarian (1999), *Adv. Mat.*, Vol. 11, No. 3, pp. 227-231.

116.   L.S. Hung, C.W. Tang and M.G. Mason (1997), *Appl. Phys. Lett.*, Vol. 70, No. 2, pp. 152-154.

117. L.S. Hung, C.W. Tang, M.G. Mason, P. Raychaudhuri and J. Madathil (2001), *Appl. Phys. Lett.*, Vol. 78, No. 4, pp. 544-546.

118. G.E. Jabbour, Y. Kawabe, S.E. Shaheen, J.F. Wang, M.M. Morrell, B. Kippelen and N. Peyghambarian (1997), *Appl. Phys. Lett.*, Vol. 71, No. 13, pp. 1762-1764.

119. Y.E. Kim, H. Park and J.J. Kim (1996), *Appl. Phys. Lett.*, Vol. 69, No. 5, pp. 599-601.

120. H. Li, H. Tang, J. Anderegg and J. Shinar (1997), *Appl. Phys. Lett.*, Vol. 70, No. 10, pp. 1233-1235.

121. B.H. Cumpston and K.F. Jensen (1995), *Synth. Met.*, Vol. 73, pp. 195-199.

122. M. Fahlman and W.R. Salaneck (2002), *Surface Science*, Vol. 500, pp. 904-922.

123. H. Aziz, Z. Popovic, C.P. Tripp, N.X. Hu, A.M. Hor and G. Xu (1998), *Appl. Phys. Lett.*, Vol. 72, No. 21, pp. 2642-2644.

124. Y. Liew, H. Aziz, N. Hu, H. Chan, G. Xu and Z. Popovic (2000), *Appl. Phys. Lett.*, Vol. 77, pp. 2650-2652.

125. P.E. Burrows, V. Bulovic, S.R. Forrest, L.S. Sapochak , D.M. McCarty and M.E. Thompson (1994), *Appl. Phys. Lett.*, Vol. 65, No. 23, pp. 2922-2924.

126. B.H. Cumpston and K.F. Jensen (1996), *Appl. Phys. Lett.*, Vol. 69, No. 25, pp. 3941-3943.

127. E. Gautier, A. Lorin, J.M. Nunzi, A. Schalchli, J.J. Benattar and D. Vital (1996), *Appl. Phys. Lett.*, Vol. 69, No. 8, pp. 1071-1073.

128. A.R. Schlatmann, D.W. Floet, A. Hilberer, F. Garten, P.J.M. Smuldars, T.M. Klapwijk and G. Hadziioannou (1996), *Appl. Phys. Lett.*, Vol. 69, No. 12, pp. 1764-1766.

129. C.I. Chao, K.R. Chuang and S.A. Chen (1996), *Appl. Phys. Lett.*, Vol. 69, No. 19, pp. 2894-2896.

130. H. Aziz and Popovic Z.D. (2004), *Chem. Mater.*, Vol. 16, pp. 4522-4532.

131. O. Prache (2001), *Displays*, Vol. 22, pp. 49-56.

132. M.C. Schlamp, X. Peng and A.P. Alivisatos (1997), *J. Appl. Phys.*, Vol. 82, pp. 5837-5842.

133. R.A.M. Hikmet, D.V. Talapin and H. Weller (2003), *J. Appl. Phys.*, Vol. 93, pp. 3509-3514.

134. N.P. Gaponik, D.V. Talapin and A.L. Rogach (1999), *Phys. Chem. Chem. Phys.*, Vol. 1, pp. 1787-1789.

135. N.P. Gaponik, D.V. Talapin, A.L. Rogach and A. Eychmuller (2000), *J. Mater. Chem.*, Vol. 10, pp. 2163-2166.

136. S. Coe, W.K. Woo, M. Bawendi and V. Bulovic (2002), *Nature*, Vol. 420, pp. 800-803.

137. H. Mattoussi, L.H. Radzilowski, B.O. Dabbousi, D.E. Fogg, R.R. Schrock, E.L. Thomas, M.F. Rubner and M.G. Bawendi (1999), *J. Appl. Phys.*, Vol. 86, pp. 4390-4399.

138. N.C. Greenham, X. Peng and A.P. Alivisatos (1996), *Phys. Rev. B*, Vol. 54, No. 24, pp. 17628-17637.

139. E.H. Rhoderick (1978), in *Metal-semiconductor contacts*, Oxford University Press, pp. 1-17.

140. N.Y. Morgan , C.A. Leatherdale, M. Drndic, M.V. Jarosz, M.A. Kastner and M. Bawendi (2002),

Phys. Rev. B, Vol. 66, pp. 075339-1-9.

141. T. Ishida, H. Kobayashi and Y. Nakato (1993), *J. Appl. Phys.*, Vol. 73, pp. 4344-4350.

142. R. Schlaf, H. Murata and Z.H. Kafafi (2001), *J. Electron Spectrosc. Relat. Phenom.*, Vol. 120, pp. 149-154.

143. L. Bardos and M. Libra (1989), *Vacuum*, Vol. 39, pp. 33-36.

144. N.C. Greenham, S.C. Moratti, D.D.C. Bradley, R.H. Firned and A.B. Holmes (1993), *Nature*, Vol. 365, pp. 628-630.

145. W. Rieβ, H. Riel, P.F. Seidler and H. Vestweber (1999), *Synthetic Metals*, Vol. 99, pp. 213-218.

146. M.V. Artemyev and V.W.U. Sperling (1997), *J. Appl. Phys.*, Vol. 81, No. 10, pp. 6975.

147. S.L. Clark and P.T. Hammond (1998), *Adv. Mater.*, Vol. 10, No. 18, pp. 1515-1519.

148. K.C. Kao and W. Hwang. *Electrical transport in solids*, Pergamon Press Ltd., 1981.

149. R.H. Fowler and L. Nordheim (1928), *Proc. R. Soc. A*, Vol. 119, pp. 173-181.

150. F.A. Padovani and R. Stratton (1966), *Solid-State Electron.*, Vol. 9, pp. 695-707.

151. O.F. Yilmaz , S. Chaudhary and M. Ozkan (2006), *Nanotechnology*, Vol. 17, pp. 3662-3667.

152. A.S. Ahmed, J. Kansy, K. Zarbout, G. Moya, J. Liebault and D. Goeuriot (2005), *J. Eur. Ceram. Soc.*, Vol. 25, pp. 2813-2816.

153. J. Kolodzey , E.A. Chowdhury, T.N. Adam, G. Qui, I. Rau, J.O. Olowolafe, J.S. Suehle and Y. Chen (2000), *IEEE T. Electron Dev.*, Vol. 47, pp. 121-128.

154. R.P. Feynman, R.B. Leighton, and M. Sands. *The Feynman lectures on physics. Quantum mechanics,* Vol.III, Addison-Wesley, 1965.

155. A.P. French and E.F. Taylor. *An introduction to quantum physics*, CRC Press, 1978.

156. N.W. Ashcroft and N.D. Mermin. *Solid State Physics*, CBS Publishing Japan, LTD, 1976.

157. M.A. Omar. *Elementary solid state physics: principles and applications*, Addison-Wesley Pub Co, 1993 .

158. W. Paul. *Handbook on semiconductors: Band theory and transport properties,* Vol.1, 1st Edition, Elsevier Science Publishers, 1982.

APPENDIXES

Related work

Title: Light emitting devices based on nanostructured semiconductors

Authors: D. E. Gallardo, C. Bertoni and S. Dunn

Abstract:

Light emitting devices based on high-efficiency photoluminescence (PL) fluorescent nanocrystals have been investigated in terms of the generation of light from the structure using a variety of deposition methods. An automated modified layer-by-layer (LbL) self-assembly technique has been employed to produce multilayers of thiol-capped red fluorescing CdTe nanocrystals. Indium-tin-oxide (ITO) and aluminium electrodes were used as the electrodes. Morphological characterization was carried out through Schottky field effect (SFEG) SEM and atomic force microscopy (AFM). The structures built presented clear red electroluminescence (EL) to the naked eye. Turn on voltages were found to be in the range of 3-6 volts while the onset current was in the order of tens of microamperes. The role of structure homogeneity, the presence of pinholes and lifetime extension were features addressed during this investigation. Samples with a lifetime of continuous operation in air longer than 60 minutes and highly stable EL spectra were achieved; EL was visible to the unaided eye, although the brightness was still below the commercial standards and has not yet been qualified.

Title: Temperature shifted photoluminescence in CdTe nanocrystals

Authors: H. C. Gardner, D. E. Gallardo, C. Bertoni, S. Dunn

Abstract:

If semiconductor quantum dots are to be incorporated into hetero-structural devices such as light emitting diodes it is important to understand the influences of the surrounding medium on the properties and particularly the photoluminescence of the nanocrystals. Here we investigate the temperature dependence of emission from CdTe quantum dots in aqueous solution with capping layers of thioglycolic acid. Results from quantum dots both held in suspension and deposited as thin films are shown. In both suspensions and thin film multilayers a reversible spectral shift to lower energy is seen with increasing temperature. This red shift of photoluminescence is thought to be the result of increased exciton carrier transfer between the quantum dots at higher temperatures and the thermal activation of emission from lower energy trap states. Both suspension and thin film devices also show a recoverable loss in photoluminescence intensity when the sample is heated. These changes are explained by the thermal activation of non-radiative surface traps. Finally, an irreversible loss in photoluminescence is reported in the CdTe thin film devices and to a lesser extent also in the quantum dot suspensions. This observation is explained by the heat induced formation of agglomerates imaged by AFM analysis.

Title: Electroforming processes for platinum nanoisland thin films

Authors: C. Bertoni, D.E. Gallardo, S. Dunn

Abstract:

An investigation of the electroforming processes for platinum discontinuous thin films is detailed. Current–voltage characteristics, for metal nanoislands deposited by sputtering, were obtained in vacuum and air and typically showed voltage-controlled negative resistance (VCNR) behaviour. The current maximum shifted with the electrode separation. Electroforming under high current density regimes was non-regenerative as samples showed irreversible resistance changes. SEM examination of the film revealed a change in the metal microstructure. Such modifications arise as a result of the current flowing through the film inducing electro and thermal migration. Current-induced effects were studied by modelling the metal nanoisland (MN) layer as an array of cubic cells. Plots of current distribution showed that hot-spots develop along conductive paths. Electromigration combined with resistive heating can lead to progressive destruction of current channels at these hot-spots. Hence, current profiles and SEM micrographs were interpreted as evidence of a 'macroscopic' electrical breakdown of sample conduction due to microstructural modifications of the thin film. The reduction of ohmic component and consequent resistive heating along the current channels prevented the metal migration and stable current profiles were obtained.

Title: Fabrication and characterization of red-emitting electroluminescent devices based on thiol-stabilized semiconductor nanocrystals

Authors: C. Bertoni, D.E. Gallardo, S. Dunn, N.P. Gaponik, A. Eychmüller

Abstract:

Thiol-capped CdTe nanocrystals were used to fabricate light-emitting diodes, consisting of an emissive nanocrystal multilayer deposited layer by layer, sandwiched between indium tin oxide and aluminum electrodes. The emissive and electrical properties of devices with different numbers of nanocrystal layers were studied. The improved structural homogeneity of the nanocrystal multilayer allowed for stable and repeatable current- and electroluminescence-voltage characteristics. These indicate that both current and electroluminescence are electric-field dependent. Devices were operated under ambient conditions and a clear red light was detected. The best performing device shows a peak external efficiency of 0.51% and was measured at 0.35 mA/cm2 and 3.3 V.

Title: LEDs with semiconductor nanocrystals: toward new architectures

Authors: N.Gaponik, A. Rogach, C.Bertoni, D.E.Gallardo, S. Dunn, N. Li Pira, M. Paderi, P. M. Repetto, S. G. Romanov, C. O'Dwyer, R. Ginige, C. M. Sotomayor Torres, A. Eychmüller

Abstract:

The advantages of the rapidly developing organic light-emitting diode (OLED) technology *[1]* can be combined with attractive properties of semiconductor nanocrystals (NCs). Optical properties of this class of lumophores are determined by the quantum confinement effect,*[2]* so that their emission colour (Figure 1) and the electron affinity can be finely controlled not only by the material choice but also by size within a single synthetic route. A typical semiconductor NC, which can also be thought of as a colloidal quantum dot, consists of an inorganic core, which is comparable to or smaller in size than the Bohr exciton diameter of the corresponding bulk material, surrounded ("passivated") by an organic shell of ligands. State-of-the-art syntheses, which can be carried out either in organic solvents*[3]* or in water,*[4]* provide different II-VI and III-V NCs with variable size and a narrow size distribution leading to narrow emission spectra – 25-35 nm full width at half maximum (FWHM) in solution – tunable from the UV to the near-infared spectral region.*[5]*